Seafloor Topography Estimation from Gravity Gradients

by

Junjun Yang

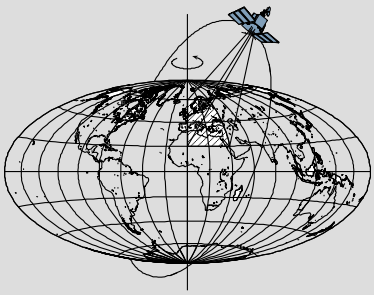

Report No. 513

Geodetic Science

The Ohio State University
Columbus, Ohio 43210

December 2017

Seafloor Topography Estimation from Gravity Gradients

By

Junjun Yang

Report No. 513

Geodetic Science
The Ohio State University
Columbus, Ohio 43210

December 2017

Abstract

Inferring seafloor topography from gravity anomaly currently is the dominant method to obtain a global view of the oceans. This study deals with the methods of inferring this topography from gravity gradients, which is more sensitive to topography at short wavelengths than gravity anomaly. Two methods, one in the spectral domain and the other in the spatial domain, were developed and tested using vertical gravity gradients derived from satellite altimetry.

The spectral domain method is based on the linear approximation to the Parker's infinite series, which is for the convenience of inversion the admittance that relates topography and gravity gradient. Only 15-160 km wavelength topography was estimated from the vertical gravity gradient, for which the inversion was stable. The long wavelengths were obtained by low-pass filtering existing bathymetric depths, and the wavelengths shorter than 15 km were omitted. This method was tested in a 2°×2° area in the West Pacific Ocean centered at (21° N, 157° E). There, the seafloor topography estimation has a root mean square error of ±268 m.

Through a numerical test, it was found that the nonlinear terrain effect was not negligible in rugged areas. Algorithmic analysis through the coherency showed that estimation accuracy at high frequencies cannot be improved by refining the resolution of gravity gradients, due to the linear approximation.

To remove the linear approximation in the modeled relationship between gravity gradients and topography, the simulated annealing, a global optimization technique that can process nonlinear inverse problems, was used to estimate the seafloor topography parameters in a forward model by minimizing the difference between the observed and forward-computed vertical gravity gradients. Careful treatments like conducting truncation error analysis, and padding the vicinity of the study area with a known topography model, were required for successful estimation. A numerical test for the same study area generated an estimation with root mean square error of ±236 m. This improves the results from the spectral domain method by 12%. Compared with the global topography model version 18 as released by the Scripps Institution of Oceanography, the estimation accuracy is improved by 22% over the study area.

The simulated annealing approach developed in this study may be used to update the global seafloor model, especially in rugged areas. Besides, this approach has no restrictions on data distribution, as required in Parker's infinite series model, thus

enabling the use of data from an airborne gravity gradiometer, whose resolution is high but flight trajectory may be irregular. This method is developed under uniform density assumption. Therefore, its performance at places of complex sub-surface geology would be poor, in general.

Preface

This report was prepared for and submitted to the Graduate School of The Ohio State University as a dissertation in partial fulfillment of the requirements for the Degree Doctor of Philosophy.

Acknowledgments

I would first like to thank my advisor, Dr. Christopher Jekeli, for responsibly preparing the renowned lectures, guiding me to trace the research frontiers, and offering enlightening discussions anytime in need with patience and impressive knowledge. His self-discipline, enthusiasm for knowledge, strictness and carefulness set a model for me and no doubt will benefit my entire career. I am also grateful to Dr. Lintao Liu, for his support and for initiating me into his airborne gravimeter design project. Moreover, I want to thank Dr. Michael Bevis and Dr. Burkhard Schaffrin for their help as committee members, great courses, and expert in their fields. Finally, a sincere gratitude goes to my parents, for their endless love and support.

I am thankful to Dr. David T. Sandwell for providing the unadjusted seafloor topography prediction, and to Dr. John Shaw in Geological Survey of Canada (Atlantic) for providing the multibeam bathymetric data over St. George's Bay. This research is supported in part by the Friend of Orton Hall travel award. Computations were partially supported by the Ohio Supercomputer Center (https://www.osc.edu/resources/getting_started/citation).

Table of Contents

Chapter 1: Introduction

1.1 Background

The ocean covers 71 percent of the Earth's surface. However, our knowledge about the topography of the seafloor in some areas is even less than that of Mars because it is difficult to observe directly [*Smith*, 1993]. Searching for the recently missing Malaysia Airlines flight MH370 shows the difficulty in viewing the ocean bottom and how little we know about it. The ocean bottom requires more detailed mapping in order to exploit its ample natural resources and to obtain information for improved understanding in geodynamics, ocean circulation, submarine and ship navigation, geophysics, fishing, marine biology, boundary delineation, Earth's climate, earthquakes and volcanoes.

1.2 Previous Studies

Since the 1950s, the seafloor depth was measured by ship using single-beam echo sounders, and later in the 1980s the multi-beam swath-mapping systems came into use [*Smith and Sandwell*, 1997]. Although the ship sounding provides high resolution mapping, it is slow and expensive. A systematic mapping of the global ocean by this method would take more than 200 years [*Smith and Sandwell*, 2004; *Sandwell et al.*, 2006; *Weatherall et al.*, 2015]. The publicly available ship sounding data are unevenly distributed. It is dense at ports and tectonic features while sparse in deep ocean areas, and is denser in the northern hemisphere than in the southern hemisphere. In the southern Pacific Ocean, the surveying tracks are as sparse as the United States Interstate Highway system, and thus make these ship sounding data alone inadequate to show detailed features of the seafloor [*Smith and Sandwell*, 2004]. Bathymetry data collected before GPS availability are usually poorly positioned and sometimes contain gross errors [*Smith*, 1993].

The fact that the gravity anomaly is correlated with topography is recognized already for over 150 years [*Lewis and Dorman*, 1970; *McKenzie and Bowin*, 1976; *Watts*, 1978; *McNutt*, 1979; *Ribe*, 1982]. The large density difference between water and the seafloor topography makes the latter contribute most to the short to medium wavelength components of the gravity anomaly while the long wavelength components are partially isostatically compensated. That is to say, except for ship sounding, it is also possible to estimate the seafloor topography using gravity anomaly data. The satellite altimetry missions provide a way to measure the sea surface height, which approximates the geoid and can be transformed into free-air gravity anomaly data that

cover the global ocean with uniform accuracy and resolution (except for polar areas). *Dixon et al.* [1983] was one of the first to demonstrate the feasibility of inferring the seafloor topography through altimetry data [*Sailor and Okal*, 1983; *White et al.*, 1983]. Based on an elastic plate regional isostatic compensation model, a theoretical response function was derived, which convolved with the detrended and band-pass-filtered one dimensional altimetry sea height tracks, transformed estimated gravity anomalies to seafloor topography. The prediction strongly depends on and is sensitive to the choice of a priori geologic parameters in the isostatic compensation model, such as effective flexural rigidity, depth of compensation, and topographic density.

Inspired by *Dixon et al.*'s research, *Smith and Sandwell* [1994; 1997] estimated the seafloor topography based on gravity anomalies derived with ±(3-5) mGal accuracy from the Seasat, Geosat, and ERS 1 satellite altimetry missions [*Sandwell and Smith*, 1992; 1997], and thus filled previously poorly charted waters. *Smith and Sandwell* [1994] downward continued the band-pass-filtered gravity anomaly at the sea surface to the mean seafloor depth, and then multiplied it with a scale factor (topography-to-gravity ratio) to represent the 15-160 km wavelength local component of seafloor topography. Finally, they added the long wavelength regional topography obtained by low-pass-filtering ship sounding data to get the final estimates. After incorporating the CryoSat-2 and Jason-1 altimetry data [*Wingham et al.*, 2006; *Sandwell et al.*, 2013; *Garcia et al.*, 2014], a new global marine gravity model with accuracy of ±2 mGal was released and the improvement on gravity accuracy also benefited the topography prediction [*Smith et al.*, 2005; *Sandwell et al.*, 2014].

Theoretical analysis shows that the shorter wavelength component of the gravity field is attenuated in the upward continuation from the seafloor to the sea surface while the longer wavelength component of gravity is partially compensated by the flexure of the lithospheric plate at the Mohorovicic discontinuity. So, the seafloor topography and the gravity anomaly at sea level are correlated only in a limited band of wavelengths (about 15-160 km). Guided by the elastic plate regional isostatic compensation theory, *Smith and Sandwell* [1994; 1997] designed a high-pass filter to remove the long wavelengths affected by the isostatic compensation. And, according to Wiener optimization theory [*Wiener*, 1949], a low-pass filter was also designed to remove the very short wavelengths, likely due to estimation error, for the purpose of minimizing the mean square error of downward continued gravity anomaly [*Sandwell and McAdoo*, 1990; *Smith and Sandwell*, 1994]. To accommodate the variation of sediment thickness and density of the seafloor, a topography-to-gravity ratio was defined and adapted to 2.5 degree by 1.25 degree local areas using ship sounding and corresponding gravity anomaly data through an inversion procedure [*Nettleton*, 1939]. Compared with the method by *Dixon et al.* [1983], the band-pass filtering and reliance on the longer wavelength signal from ship sounding data avoids the complex assumption about the isostatic model.

The *Smith and Sandwell* gravimetric grid is widely adopted and extensively discussed by researchers in different disciplines. It is the dataset upon which most publicly available global bathymetric grids are built, such as DBDB2, ETOPO2, GINA, and GEBCO, etc. [*Marks and Smith*, 2006; *Marks et al.*, 2010]. The method above is based on Parker's formula (1973), and are conducted in the frequency domain using Fast Fourier Transforms (FFT). A number of shortcomings may be considered in the linear relation, that is, in using only the first term of Parker's infinite series [*Parker*, 1973, equation 4] as an approximation to the admittance in areas of rugged topography and tall sea mounts where the local topography is significant compared with the regional topography. The missing 0-15 km wavelength components cause inaccuracy in these areas since they are needed to fit the sharply varying topography. The processing in the frequency domain makes it impossible to exploit sparse data since the FFT technique requires regularly gridded data. Moreover, it does not deal with the noise in the gravity and sounding data.

Several researchers have studied another method, the gravity-geologic method (GGM), for seafloor topography prediction using altimetry-derived free-air gravity anomalies and ship sounding data [*J W Kim et al.*, 2010a; *K B Kim et al.*, 2010b; *Hsiao et al.*, 2011; *Ouyang et al.*, 2014]. In the GGM method, the gravity anomaly is divided into a residual component and a regional component. The residual gravity is attributed to topography and is modeled by the Bouguer slab formula. The regional gravity is attributed to deeper mass variations. At control points where both ship sounding depth and gravity anomaly are known, the regional gravity is computed by subtracting the residual gravity from the total gravity anomaly. At prediction points where only the total gravity anomaly is known, the regional gravity is interpolated from the values at the control points. Subtracting it from the total gravity anomaly gives the residual gravity, which then gives the seafloor topography by inversely applying the Bouguer slab formula. In this procedure, the tuning density contrast parameter $\Delta\rho$ in the Bouguer slab formula is an empirical parameter and differs from the water-rock density difference. Its value is determined in advance using all the control points. In [*J W Kim et al.*, 2010a], two thirds of the control points were used to estimate the topography at the remaining third. The RMS (root mean square) error was computed at these points and plotted as a function of increasing $\Delta\rho$. The $\Delta\rho$ at which the RMS difference becomes comparatively stable was chosen as the tuning density contrast. The selected value of $\Delta\rho$ was 9 g/cm^3. A problem with this procedure is that it does not consider the downward continuation effect. Therefore, the tuning density contrast is essentially the mean real density contrast scaled by a downward continuation factor in the spatial domain.

Like the algorithm in [*Smith and Sandwell*, 1994], the GGM method also divides topography into a local component and a regional one, although the division is conducted in the spatial domain using the Bouguer slab formula rather than in the frequency domain. Moreover, both methods predict topography by multiplying the gravity anomaly by an empirical scaling factor based on the use of control points. To some extent the GGM method is a simplified *Smith and Sandwell*

[1994]'s algorithm without applying the downward continuation and conducting the isostatic compensation analysis.

In recent years, new methods have been investigated for gravity based seafloor topography estimation.

Least-squares inversion to estimate the seafloor topography in the spatial domain was investigated by *Calmant* [1994], *Ramillien and Wright* [2000], *Wang* [2000], and *Calmant et al.* [2002]. This method allows the computation of uncertainty of the predicted bathymetry.

Jena et al. [2012] estimated the topography using an artificial neural network (ANN) model approach based on radial basis functions. Half of the gravity anomaly and sounding data were used to train the model, 25% were used to determine the architecture of the ANN, and the remaining 25% were used for validation of the predicted results. The results showed that the correlation between the ANN-predicted bathymetry and echo sounding data was 0.9. Then the ANN model was tested near two seamounts and, compared to three global bathymetry models SIO V13.1, ETOPO1, and GEBCO V2.0, gave improved predicted topography. In their study, although comparison between the predicted bathymetry results and ship sounding showed reasonable estimation capability, its theoretical base was not clearly elaborated. Besides, the authors pointed out that the prediction works better at regions similar to the trained region.

Li and Ma [2014] verified the feasibility of estimating seafloor topography by the simulated annealing method using gravity gradient data, which is a nonlinear form of least-squares estimation. Comparison between the predicted bathymetry result and ship sounding showed reasonable estimation capability. Regions with different geology setting may generate similar gravity gradients, so the accuracy of this method at regions with different morphological characteristics and sub-topography geologic structures should be investigated further. The authors adopted Parker's series as forward computation formula, which requires regularly gridded data. The estimation accuracy at the grid margins might be low since an assumption in applying discrete Fourier transform techniques is periodic extension of the data grid.

Hu et al. [2014a] and *Hu et al.* [2014b] estimated global seafloor topography using vertical gravity gradients derived from satellite altimetry and NGDC ship sounding data. Their method is similar to *Smith and Sandwell*'s algorithm. The long wavelength topography was obtained by low-pass-filtering the ship sounding data. The 20-200 km wavelength seafloor topography was estimated by multiplying the gravity gradients with a topography-to-gradient ratio. Combining the gravity anomaly and gravity gradient data was also considered, as was isostatic compensation, but the authors did not analyze the selection of cut-off wavelength, and the validity of their method of combining gravity anomaly and gravity gradient is not effectively clarified.

In addition to the prediction methods, the need to launch a new altimetry satellite to improve the spatial resolution has also been discussed by several scholars [*Raney et al.*, 2003; *Smith and Sandwell*, 2004; *Smith et al.*, 2005; *Sandwell et al.*, 2006; *Shum et al.*, 2009]. The resulting

inferred high resolution gravity data may improve the accuracy of topography estimation at shallow areas by reducing the omitted 0-15 km short wavelength band.

1.3 Objective

Inferring seafloor topography from gravity currently is the best way to obtain a global view, provided one has global gravity coverage. The only alternative, radar sounding, only covers about 10% of the ocean floor. It would take about 200 ship-years and cost billions of dollars for ship carrying multibeam echo sounders to map the global ocean floor [*Sandwell et al.*, 2006]. Therefore, it is worthwhile to improve on the indirect gravimetric method [*Hwang et al.*, 2006].

Standard techniques rely on an approximate, linear relationship between topography and gravity. In fact, it is a first term approximation to Parker's theory [*Parker*, 1973], which is valid only if the local topography is small compared with the regional topography. Numerical analysis in section 3.2 will show that in rugged areas (topography ranges from -1000 m to -5000 m over a 200 km by 200 km rectangular area), the nonlinear terrain effect for the vertical gravity gradient can be as much as 49 Eötvös. At wavelengths shorter than 5 km, more than half of the vertical gravity gradient was from the nonlinear terms of Parker's infinite series. Therefore, it is important to consider nonlinear terms in the inversion process and this requires new algorithms that can handle tens of thousands of parameters in nonlinear models.

Current methods have used altimetry-derived gravity anomalies to indirectly infer seafloor topography. Gravity gradients are more sensitive to the short wavelength topography than gravity anomalies, so the corresponding performance in topography prediction is expected to be better and thus is in need of demonstration. Airborne gravity gradiometry is a more direct measure of the Earth's gravity field at shorter wavelengths. Besides, airborne gravity gradient surveys can be deployed in polar areas that satellite altimetry usually does not cover. However, because it is as yet scarcely available in ocean areas, the estimation algorithm developed in this study is tested mainly using altimetry-derived gravity gradients as a proxy, although one set of airborne gravity gradiometry data is also considered. Altimetry-derived vertical gravity gradients are publicly available, but the spatial resolution in gravity gradient estimation from altimetry is limited in any case (about 2.5 km for Cryosat-2, and 7.5 km for Jason-1's geodetic mission phase [*Marks*, 1996; *Sandwell et al.*, 2014]). When using airborne gravity gradiometry, not only the accuracy but also the spatial resolution of the gravity field may be improved for better inference of seafloor topography.

It is the objective of this research to improve current methods by 1) removing the linear approximation in the modeled relationship between gravity and topography, and 2) by using another type of gravimetry that is more sensitive to short wavelength topography, i.e., gravity gradiometry. The former is extremely important in rugged areas. These improvements are

important in updating the global seafloor model to achieve higher accuracy and resolution, which has not seen major improvement for more than 20 years.

Chapter 2: Relationship between Topography and Gravity

2.1 Relationship in the Frequency Domain

2.1.1 Parker's Theory

Using Fourier transformation, *Parker* [1973] gave the formulas to calculate the gravitational acceleration caused by a non-uniform volume of material, which provided a clue to correlate the topography with gravity anomaly in the frequency domain. The detailed derivation is provided below. These formulas are generalized to incorporate the gravitational gradient.

The 2-D Fourier transform pair of a function, g, is:

$$\breve{g}(f_1, f_2) = \int_{y=-\infty}^{\infty} \int_{x=-\infty}^{\infty} g(x, y) e^{-i2\pi(f_1 x + f_2 y)} dx dy \tag{2.1}$$

$$g(x, y) = \int_{f_2=-\infty}^{\infty} \int_{f_1=-\infty}^{\infty} \breve{g}(f_1, f_2) e^{i2\pi(f_1 x + f_2 y)} df_1 df_2 \tag{2.2}$$

where x, y are space domain arguments of g, and f_1, f_2 are cycle-frequencies.

Assume the lower boundary of a volume of material is the plane $z = 0$, and the upper boundary is defined by the equation $z = b(x, y)$. Further assumptions are: i) the volume is constrained in a certain area, i.e. $b(x, y) = 0$, $\sqrt{x^2 + y^2} > Constant$; ii) $b(x, y)$ and all its powers, $b^n(x, y)$, are bounded and integrable.

The gravitational potential at point (x, y, z) caused by the mass of this volume is:

$$
\begin{aligned}
V(x,y,z) &= G\rho \iiint_{\Omega} \frac{1}{\sqrt{(x-\xi)^2+(y-\eta)^2+(z-\zeta)^2}} d\xi d\eta d\zeta \\
&= G\rho \iint_{\sigma} \int_{\zeta=0}^{b(\xi,\eta)} \frac{1}{\sqrt{(x-\xi)^2+(y-\eta)^2+(z-\zeta)^2}} d\zeta d\xi d\eta
\end{aligned}
\tag{2.3}
$$

where G is the gravitational constant, (ξ,η,ζ) are the coordinates of a mass element, Ω represents the volume of material, σ is the x-y plane, and density ρ is assumed constant for the moment.

Confine all the evaluations of gravitational potential on the plane $z = z_0$, which is above all the topography. i.e. $z_0 > \max\left(b(x,y)\right)$. Take the Fourier transform of (2.3):

$$
\begin{aligned}
&\mathcal{F}\left(V(x,y,z_0)\right) \\
&= \int_{x=-\infty}^{\infty} \int_{y=-\infty}^{\infty} V(x,y,z_0) e^{-i2\pi(f_1 x + f_2 y)} dxdy \\
&= G\rho \int_{x=-\infty}^{\infty} \int_{y=-\infty}^{\infty} \iint_{\sigma} \int_{\zeta=0}^{b(\xi,\eta)} \frac{1}{\sqrt{(x-\xi)^2+(y-\eta)^2+(z_0-\zeta)^2}} d\zeta d\xi d\eta \cdot e^{-i2\pi(f_1 x + f_2 y)} dxdy \\
&= G\rho \iint_{\sigma} \int_{\zeta=0}^{b(\xi,\eta)} \int_{x=-\infty}^{\infty} \int_{y=-\infty}^{\infty} \frac{e^{-i2\pi(f_1 x + f_2 y)}}{\sqrt{(x-\xi)^2+(y-\eta)^2+(z_0-\zeta)^2}} dxdyd\zeta d\xi d\eta
\end{aligned}
\tag{2.4}
$$

According to equation (1.153) in Jekeli's *Fourier Geodesy* [2013b]

$$
\mathcal{F}\left(\frac{1}{\sqrt{x^2+y^2+a^2}}\right) = \frac{1}{\sqrt{f_1^2+f_2^2}} e^{-2\pi a\sqrt{f_1^2+f_2^2}} \tag{2.5}
$$

Applying (2.5) to (2.4) and changing the integration variable, we have

$$
\begin{aligned}
&\mathcal{F}\left(V\left(x,y,z_0\right)\right)\\
&=G\rho\iint_{\sigma}\int_{\zeta=0}^{b(\xi,\eta)}\int_{x-\xi=-\infty}^{\infty}\int_{y-\eta=-\infty}^{\infty}\frac{e^{-i2\pi\left[f_1(x-\xi)+f_2(y-\eta)\right]-i2\pi(f_1\xi+f_2\eta)}}{\sqrt{\left(x-\xi\right)^2+\left(y-\eta\right)^2+\left(z_0-\zeta\right)^2}}d\left(x-\xi\right)d\left(y-\eta\right)d\zeta\,d\xi d\eta\\
&=G\rho\iint_{\sigma}\int_{\zeta=0}^{b(\xi,\eta)}\int_{x-\xi=-\infty}^{\infty}\int_{y-\eta=-\infty}^{\infty}\frac{e^{-i2\pi\left[f_1(x-\xi)+f_2(y-\eta)\right]}}{\sqrt{\left(x-\xi\right)^2+\left(y-\eta\right)^2+\left(z_0-\zeta\right)^2}}d\left(x-\xi\right)d\left(y-\eta\right)\cdot e^{-i2\pi(f_1\xi+f_2\eta)}d\zeta\,d\xi d\eta\\
&=G\rho\iint_{\sigma}\int_{\zeta=0}^{b(\xi,\eta)}\frac{e^{-i2\pi(f_1\xi+f_2\eta)-2\pi\sqrt{f_1^2+f_2^2}(z_0-\zeta)}}{\sqrt{f_1^2+f_2^2}}d\zeta\,d\xi d\eta
\end{aligned}
$$

(2.6)

Performing the last integral gives

$$
\mathcal{F}\left(V\left(x,y,z_0\right)\right)=\frac{G\rho}{2\pi}\iint_{\sigma}\frac{e^{-i2\pi(f_1\xi+f_2\eta)-2\pi\sqrt{f_1^2+f_2^2}z_0}\left(e^{2\pi\sqrt{f_1^2+f_2^2}b(\xi,\eta)}-1\right)}{f_1^2+f_2^2}d\xi d\eta \qquad (2.7)
$$

Expanding the second exponential function into Taylor series and rearranging the equation, we have

$$
\begin{aligned}
\mathcal{F}\left(V\left(x,y,z_0\right)\right)&=\frac{G\rho}{2\pi}\iint_{\sigma}\frac{e^{-i2\pi(f_1\xi+f_2\eta)-2\pi\bar{f}z_0}\sum_{n=1}^{\infty}\frac{\left(2\pi\bar{f}b\left(\xi,\eta\right)\right)^n}{n!}}{\bar{f}^2}d\xi d\eta\\
&=2\pi G\rho\frac{e^{-2\pi\bar{f}z_0}\sum_{n=1}^{\infty}\frac{\left(2\pi\bar{f}\right)^n}{n!}\iint_{\sigma}\left(b\left(\xi,\eta\right)\right)^n e^{-i2\pi(f_1\xi+f_2\eta)}d\xi d\eta}{\left(2\pi\bar{f}\right)^2} \qquad (2.8)\\
&=2\pi G\rho e^{-2\pi\bar{f}z_0}\sum_{n=1}^{\infty}\frac{\left(2\pi\bar{f}\right)^{n-2}}{n!}\mathcal{F}\left(b^n\left(x,y\right)\right)
\end{aligned}
$$

where we define the radial frequency $\bar{f}=\sqrt{f_1^2+f_2^2}$.

When b lies entirely below the evaluation plane $z=z_0$, (2.8) is uniformly convergent [*Parker*, 1973]. Note that $\mathcal{F}\left(V\left(x,y,z_0\right)\right)$ does not exist at $\bar{f}=0$ due to the $\bar{f}^{-1}$ in the n=1 term.

V satisfies Laplace's equation outside the mass body, thus according to equation (1.89) in Jekeli's *Fourier Geodesy* [2013b], the Fourier transform of the vertical derivative is:

$$\mathcal{F}\left(\frac{\partial V(x,y,z)}{\partial z}\right) = -2\pi\bar{f}\,\mathcal{F}\left(V(x,y,z)\right) \tag{2.9}$$

The vertical component of gravitation $g(x,y,z)$ caused by the source volume is

$$g(x,y,z) = \frac{\partial V(x,y,z)}{\partial z} \tag{2.10}$$

It is valid only for planar approximation, since $\frac{\partial V}{\partial z} \neq \frac{\partial V}{\partial r}$ if z is not along the radial direction.

Substituting (2.8) and (2.10) into (2.9), we have

$$\mathcal{F}\left(g(x,y,z_0)\right) = -2\pi G\rho e^{-2\pi\bar{f}z_0}\sum_{n=1}^{\infty}\frac{\left(2\pi\bar{f}\right)^{n-1}}{n!}\mathcal{F}\left(b^n(x,y)\right) \tag{2.11}$$

If the lower boundary is $z = k(x,y)$ rather than $z = 0$, and the density ρ varies with x and y coordinates, equation (2.11) is generalized to

$$\begin{aligned}&\mathcal{F}\left(g(x,y,z_0)\right)\\ &= -2\pi G e^{-2\pi\bar{f}z_0}\sum_{n=1}^{\infty}\frac{\left(2\pi\bar{f}\right)^{n-1}}{n!}\mathcal{F}\left(\rho(x,y)\left(b^n(x,y)-k^n(x,y)\right)\right)\end{aligned} \tag{2.12}$$

The gravitational gradient tensor element $\Gamma_{zz} = \frac{\partial^2 V}{\partial z^2}$ is the second derivative of the gravitational potential. Similar to (2.11) we have

$$\begin{aligned}\mathcal{F}\left(\Gamma_{zz}(x,y,z_0)\right) &= \mathcal{F}\left(\frac{\partial^2 V}{\partial z^2}(x,y,z_0)\right)\\ &= 2\pi G\rho e^{-2\pi\bar{f}z_0}\sum_{n=1}^{\infty}\frac{\left(2\pi\bar{f}\right)^{n}}{n!}\mathcal{F}\left(b^n(x,y)\right)\end{aligned} \tag{2.13}$$

For the other elements of the gravity gradient tensor, we need the differentiation theorem [*Jekeli*, 2017]:

$$\mathcal{F}\left(\frac{\partial^{m+l}V(x,y,z)}{\partial x^m\partial y^l}\right) = \left(i2\pi f_1\right)^m\left(i2\pi f_2\right)^l\mathcal{F}\left(V(x,y,z)\right) \tag{2.14}$$

Applying (2.14) and (2.9) to (2.8) gives:

$$\mathcal{F}\left(\frac{\partial^{m+l+k}V(x,y,z_0)}{\partial x^m \partial y^l \partial z^k}\right) = \left(i2\pi f_1\right)^m \left(i2\pi f_2\right)^l \left(-2\pi \bar{f}\right)^k 2\pi G\rho e^{-2\pi \bar{f} z_0} \sum_{n=1}^{\infty} \frac{\left(2\pi \bar{f}\right)^{n-2}}{n!} \mathcal{F}\left(b^n(x,y)\right) \tag{2.15}$$

2.1.2 Forsberg's Method

Like Parker's theory, Forsberg's method [*Forsberg*, 1985] also relates the topography and the gravity gradient. Parker's theory performs the vertical derivative in the frequency domain, whereas Forsberg's method performs the vertical derivative in the space domain. This led to different approximations in the practical implementation, i.e., Parker's theory has to truncate in the frequency domain, while Forsberg's method would truncate in the space domain. While the two methods are the same in theory, Forsberg's method allows an easier way to formulate the truncation error in subsection 2.3.1, and therefore, is described here.

The formula for the vertical gravity gradient (VGG) generated by the topography relative to a reference plane is

$$\begin{aligned}\Gamma_{zz}(x,y,z) &= \frac{\partial^2}{\partial z^2}\left[G\rho \iint_{\sigma} \int_{\zeta=\bar{b}}^{b(\xi,\eta)} \frac{1}{r} d\zeta d\sigma\right] \\ &= G\rho \iint_{\sigma} \int_{\zeta=\bar{b}}^{b(\xi,\eta)} \left(\frac{3(z-\zeta)^2}{r^5} - \frac{1}{r^3}\right) d\zeta d\sigma, \\ &= G\rho \iint_{\sigma} \int_{\zeta=\bar{b}}^{b(\xi,\eta)} F_{zz} d\zeta d\sigma\end{aligned} \tag{2.16}$$

where $r = \sqrt{(x-\xi)^2 + (y-\eta)^2 + (z-\zeta)^2}$ is the distance between the observation point, (x,y,z), and the integration element, (ξ,η,ζ), G is Newton's gravitational constant, ρ is the density of the topography which is supposed to be constant, $b(\xi,\eta)$ is the elevation of topography, the constant $\bar{b}$ is the elevation of the reference plane, σ is the x-y plane, and F_{zz} is given by

$$F_{zz} = \frac{3(z-\zeta)^2}{r^5} - \frac{1}{r^3}. \tag{2.17}$$

Expand F_{zz} into a Taylor series with respect to ζ evaluated at $\zeta = \bar{b}$, we have

$$F_{zz}\left(x,y,z,\xi,\eta,\zeta\right) = \sum_{n=0}^{\infty} \frac{1}{n!} \frac{\partial^n F_{zz}\left(x,y,z,\xi,\eta,\bar{b}\right)}{\partial \zeta^n} \left(\zeta - \bar{b}\right)^n . \tag{2.18}$$

Substituting (2.18) into (2.16), we have

$$\begin{aligned} \Gamma_{zz}\left(x,y,z\right) &= G\rho \iint_{\sigma} \int_{\zeta=\bar{b}}^{b(\xi,\eta)} F_{zz} d\zeta d\sigma \\ &= G\rho \sum_{n=0}^{\infty} \frac{1}{(n+1)!} \iint_{\sigma} \frac{\partial^n F_{zz}\left(x,y,z,\xi,\eta,\bar{b}\right)}{\partial \zeta^n} \left[b\left(\xi,\eta\right) - \bar{b}\right]^{n+1} d\sigma \end{aligned} . \tag{2.19}$$

Its first term approximation gives

$$\begin{aligned} \Gamma_{zz}\left(x,y,z\right) &= G\rho \iint_{\sigma} F_{zz}\left(x,y,z,\xi,\eta,\bar{b}\right)\left[b\left(\xi,\eta\right) - \bar{b}\right] d\sigma \\ &= G\rho \iint_{\sigma} F'_{zz}\left(s\right)\left[b\left(\xi,\eta\right) - \bar{b}\right] d\sigma \end{aligned} , \tag{2.20}$$

where $s = \sqrt{\left(x-\xi\right)^2 + \left(y-\eta\right)^2}$, and the abbreviation of $F_{zz}\left(x,y,z,\xi,\eta,\bar{b}\right)$, $F'_{zz}\left(s\right)$, is given by

$$\begin{aligned} F'_{zz}\left(s\right) &= \frac{3\left(z-\bar{b}\right)^2}{\left[s^2 + \left(z-\bar{b}\right)^2\right]^{\frac{5}{2}}} - \frac{1}{\left[s^2 + \left(z-\bar{b}\right)^2\right]^{\frac{3}{2}}} \\ &= \frac{3\left(z-\bar{b}\right)^2}{\left[\left(x-\xi\right)^2 + \left(y-\eta\right)^2 + \left(z-\bar{b}\right)^2\right]^{\frac{5}{2}}} - \frac{1}{\left[\left(x-\xi\right)^2 + \left(y-\eta\right)^2 + \left(z-\bar{b}\right)^2\right]^{\frac{3}{2}}} \end{aligned} . \tag{2.21}$$

In the present analysis, we assume the evaluation point lies on a plane $z = \mathrm{z}_0$. The equation (2.20) is a convolution on the plane. Applying the convolution theorem to (2.20) gives

$$\breve{\Gamma}_{zz}\left(f_1,f_2\right) = G\rho \breve{F}'_{zz}\left(\bar{f}\right)\breve{b}\left(f_1,f_2\right) - G\rho\bar{b}\breve{F}'_{zz}\left(0\right)\delta\left(\bar{f}\right), \tag{2.22}$$

where $\delta\left(\bar{f}\right)$ is the 2-D Dirac delta function. Note that $\breve{F}'_{zz}\left(\bar{f}\right)$ is isotropic due to the isotropy of $F'_{zz}\left(s\right)$, and is given by the Hankel transform [*Jekeli*, 2017]

$$\breve{F}'_{zz}\left(\overline{f}\right) = 2\pi \int_{s'=0}^{\infty} \left[\frac{3\left(z_0 - \overline{b}\right)^2}{\left[s'^2 + \left(z_0 - \overline{b}\right)^2\right]^{\frac{5}{2}}} - \frac{1}{\left[s'^2 + \left(z_0 - \overline{b}\right)^2\right]^{\frac{3}{2}}} \right] J_0\left(2\pi \overline{f} s'\right) s' ds' \quad , \quad (2.23)$$
$$= \left(2\pi\right)^2 \overline{f} e^{-2\pi\left(z_0 - \overline{b}\right)\overline{f}}$$

where $s' = \sqrt{x^2 + y^2}$, $z_0 - \overline{b} > 0$, and J_0 is the zero-order Bessel function of the first kind.

Substituting (2.23) into (2.22) and setting the elevation of the reference plane, $\overline{b}$, to zero, we have

$$\breve{\Gamma}_{zz}\left(f_1, f_2\right) = 4\pi^2 \overline{f} G \rho e^{-2\pi \overline{f} z_0} \breve{b}\left(f_1, f_2\right) \quad (2.24)$$

which is the same as the first term of equation (2.13).

2.1.3 Relationships of Gravity Anomaly and Gravity Gradient to Topography

The equation (2.11) is a formula to compute the gravitational acceleration caused by topography above sea level under certain assumptions (constant density, planar approximation, convergent series, constant-height measurement surface above all masses). Conversely, we could invert given free-air gravity anomaly to obtain seafloor topography if the only source of gravity anomaly is the anomalous topography. But in fact the free-air gravity anomaly is the combination of the topographic effect described by (2.11), isostatic compensation at the Mohorovicic discontinuity, and density variations within the Earth. So, in order to correctly relate gravity anomaly with topography, it is necessary to analyze the sources of gravity anomaly and remove the non-terrain components.

The observed gravity is usually written as

$$g_P = \gamma_Q - F + A_T + A_C + A_G \quad (2.25)$$

where g_P is the observed gravity at point P, γ_Q is normal gravity referred to the ellipsoid, F is the free-air reduction to the geoid, A_T is the attraction of constant density topography, A_C is the attraction of the compensation as a response to A_T , and A_G is the attraction due to the variations in density from an assumed constant, in the crust and possibly in the upper mantle [*Banks et al.*, 1977; *Hofmann-Wellenhof and Moritz*, 2005].

In ocean areas, when one makes the flat-Earth approximation, the gravity anomaly is approximated by the gravity disturbance [*Sandwell and Smith*, 1997]. The usual practice of this approximation is followed because only the short-to-intermediate wavelength topography is predicted from gravity (the reason is discussed in subsection 2.1.4), which is much shorter than the radius of Earth [*Tapley*, 1997].

The components of the free-air gravity anomaly are

$$\Delta g_F = g_P - \gamma_Q + F = A_T + A_C + A_G \tag{2.26}$$

Firstly we analyze the attraction of topography A_T, which is the combined effect of a Bouguer plate and terrain correction. On land it is the attraction of the mass between the Earth's surface and the geoid. In the ocean, we treat it as the effect of mass deficiency caused by the sea water between the sea surface and the seafloor b'. Another view treats A_T as the attraction of the seafloor topography deviating from the mean sea depth d, but having (positive) density, $\Delta\rho = \rho_c - \rho_w$, i.e., the density difference between the crust and sea water. This topography is denoted as b in the Figure 2.1, and refers to a reference level at depth, d (the coordinate origin for z is still sea level). From Figure 2.1 we find that

$$b(x,y) = b'(x,y) + d\,, \tag{2.27}$$

with the following definitions: the depth, b', is always negative and the topography, b, could be positive or negative, while, the mean depth, d, is defined to be positive. Hereinafter, given the mean sea depth, the depth can always be related to the topography through equation (2.27). The difference between the gravitational acceleration computed through the two methods is just a constant, $2\pi\Delta\rho Gd$. It is a long wavelength effect and will not affect the topography estimation.

For the former view, replace ρ, z_0, b, k by $-\Delta\rho$, 0, 0, b' in (2.12) to get

$$\begin{aligned}\mathcal{F}\left(A_T(x,y,0)\right) &= -2\pi G(-\Delta\rho)e^{-2\pi\bar{f}0}\sum_{n=1}^{\infty}\frac{\left(2\pi\bar{f}\right)^{n-1}}{n!}\mathcal{F}\left(0-b'^n(x,y)\right)\\ &= -2\pi G\Delta\rho e^{-2\pi\bar{f}0}\sum_{n=1}^{\infty}\frac{\left(2\pi\bar{f}\right)^{n-1}}{n!}\mathcal{F}\left(b'^n(x,y)\right)\end{aligned}, \tag{2.28}$$

which is the formula to compute the gravitational effect of the seafloor depths at sea level.

For the latter view, replace ρ, z_0, b, k by $\Delta\rho$, 0, b', $-d$ in (2.12) to get

$$\mathcal{F}\left(A_T(x,y,0)\right) = -2\pi G\Delta\rho e^{-2\pi\bar{f}0}\sum_{n=1}^{\infty}\frac{\left(2\pi\bar{f}\right)^{n-1}}{n!}\mathcal{F}\left(b'^n(x,y)-(-d)^n\right). \quad (2.29)$$

Translate the z-axis a distance d downward (z_0 in the original coordinate system becomes z_0+d in the new system, b' becomes b, d becomes 0, and $e^{-2\pi\bar{f}0}$ becomes $e^{-2\pi\bar{f}d}$). Then one obtains the formula

$$\mathcal{F}\left(A_T(x,y,d)\right) = -2\pi G\Delta\rho e^{-2\pi\bar{f}d}\sum_{n=1}^{\infty}\frac{\left(2\pi\bar{f}\right)^{n-1}}{n!}\mathcal{F}\left(b^n(x,y)\right). \quad (2.30)$$

In this study the latter view is adopted.

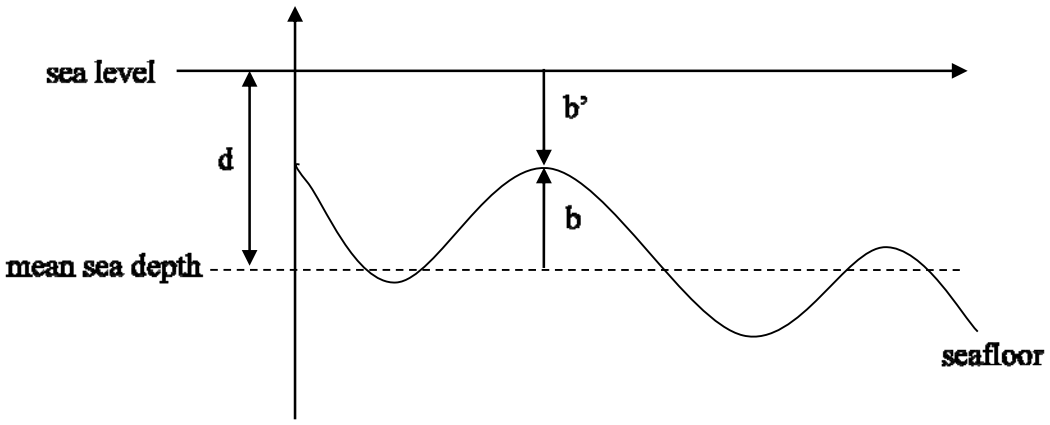

Figure 2.1: The variables used to denote depth, the mean depth, and the seafloor topography.

Formula (2.30) computes the gravitational effect of the seafloor topography on the sea surface that is due to its deviation from the mean water depth. The reason to use (2.30) rather than (2.28) is discussed in subsection 3.2.1. In short, the purpose is to minimize $\max|b|/d$ so that Parker's series concentrates on the n=1 term. If the local topography is small compared with the regional

topography, the first term of the right-hand side of the infinite series is the dominant term [*Parker*, 1973]:

$$\mathcal{F}\left(A_T\left(x,y,d\right)\right) \approx -2\pi G\left(\rho_c-\rho_w\right)e^{-2\pi\bar{f}d}\,\mathcal{F}\left(b\left(x,y\right)\right) \tag{2.31}$$

With the above substitutions applied to (2.15), the gravitational gradient effect of the seafloor topography is given by

$$\begin{aligned}&\mathcal{F}\left(\frac{\partial^{m+l+k}V_{A_T}\left(x,y,d\right)}{\partial x^m\partial y^l\partial z^k}\right)\\&=\left(i2\pi f_1\right)^m\left(i2\pi f_2\right)^l\left(-2\pi\bar{f}\right)^k 2\pi G\left(\rho_c-\rho_w\right)e^{-2\pi\bar{f}d}\sum_{n=1}^{\infty}\frac{\left(2\pi\bar{f}\right)^{n-2}}{n!}\mathcal{F}\left(b^n\left(x,y\right)\right)\end{aligned} \tag{2.32}$$

where m, l, and k are non-negative integers, and $m+l+k=2$.

Its first term approximation gives:

$$\begin{aligned}&\mathcal{F}\left(\frac{\partial^{m+l+k}V_{A_T}\left(x,y,d\right)}{\partial x^m\partial y^l\partial z^k}\right)\\&\approx-\left(i2\pi f_1\right)^m\left(i2\pi f_2\right)^l\left(-2\pi\bar{f}\right)^{k-1}2\pi G\left(\rho_c-\rho_w\right)e^{-2\pi\bar{f}d}\,\mathcal{F}\left(b\left(x,y\right)\right)\end{aligned} \tag{2.33}$$

Now consider the gravitational effect of the isostatic compensation. The regional isostatic compensation mechanism treats the lithosphere as a thin elastic plate that floats on a viscous liquid, that flexes under the load, and causes A_C by perturbing the density around the interface of layers [*McKenzie and Bowin*, 1976; *Banks et al.*, 1977; *Watts*, 2001]. The flexure $u\left(x,y\right)$ (Figure 2.2) and the load $b\left(x,y\right)$ are related by

$$\mathcal{F}\left(u\left(x,y\right)\right)=-\mathcal{F}\left(b\left(x,y\right)\right)\frac{\rho_c-\rho_w}{\rho_m-\rho_c}\Phi_e\left(\bar{f}\right) \tag{2.34}$$

where ρ_m is the density of the mantle, and $\Phi_e\left(\bar{f}\right)$ is given by (2.37).

Seafloor topography $b\left(x,y\right)$ is the density interface between the seabed and water, and the flexure $u\left(x,y\right)$ is the density interface between the crust and mantle. So, with another translation

of the z origin, substitute b by u, and substitute the mean depth of topography, d, by the mean depth of flexure, $d+t$, in (2.31), and one obtains the gravitational effect of the flexure on the sea surface that is due to its deviation from the mean depth $d+t$, when one makes the first term approximation,

$$\mathcal{F}\left(A_C\right) \approx -2\pi G\left(\rho_m - \rho_c\right) e^{-2\pi \bar{f}(d+t)} \mathcal{F}\left(u\left(x,y\right)\right) \tag{2.35}$$

where t is the mean thickness of the crust.

Substituting (2.34) into (2.35) gives

$$\mathcal{F}\left(A_C\right) \approx 2\pi G\left(\rho_c - \rho_w\right) \Phi_e\left(\bar{f}\right) e^{-2\pi \bar{f}(d+t)} \mathcal{F}\left(b\left(x,y\right)\right) \tag{2.36}$$

where $\Phi_e\left(\bar{f}\right)$ is the frequency domain function that modifies the Airy response so as to produce the flexure.

$$\Phi_e\left(\bar{f}\right) = \left[\frac{16D\pi^4 \bar{f}^4}{\left(\rho_m - \rho_c\right)g} + 1\right]^{-1} \tag{2.37}$$

In this model, g is the gravitational acceleration, and D is the flexural rigidity of the plate given by

$$D = \frac{ET_e^3}{12\left(1-\nu^2\right)} \tag{2.38}$$

where E is Young's modulus, ν is Poisson's ratio, and T_e is the elastic thickness of the plate.

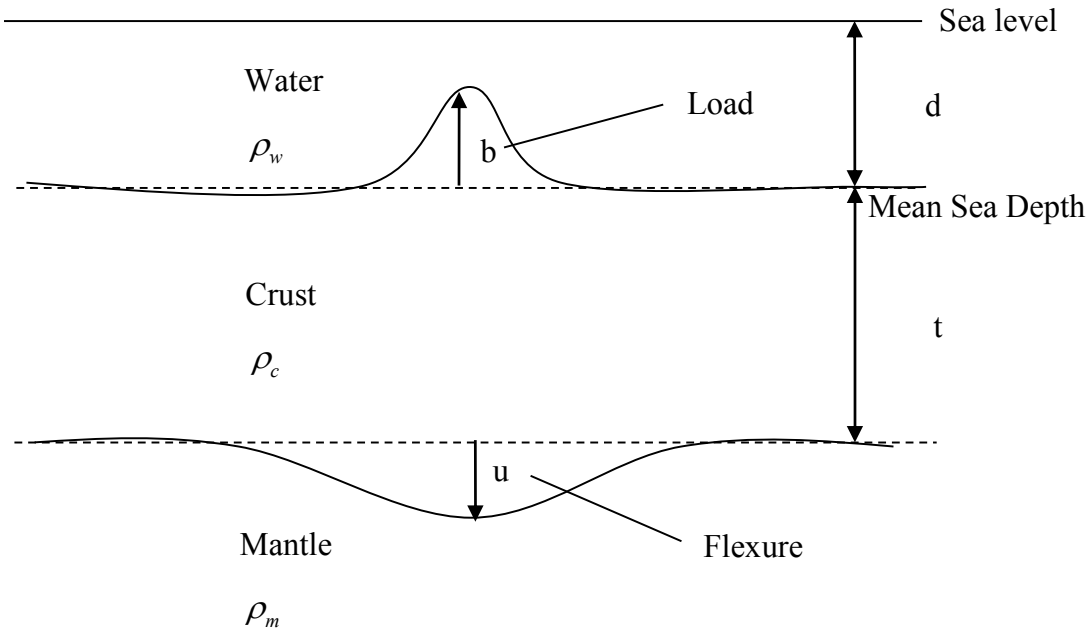

Figure 2.2: The simple elastic plate model of isostatic compensation.

Combining (2.32) and (2.34) gives the gravitational gradient effect of the isostatic compensation

$$\mathcal{F}\left(\frac{\partial^{m+l+k}V_{A_C}(x,y,d+t)}{\partial x^m \partial y^l \partial z^k}\right) = (i2\pi f_1)^m (i2\pi f_2)^l (-2\pi\bar{f})^k \, 2\pi G(\rho_m-\rho_c) e^{-2\pi\bar{f}(d+t)} \sum_{n=1}^{\infty} \frac{(2\pi\bar{f})^{n-2}}{n!} \mathcal{F}\left(u^n(x,y)\right) \tag{2.39}$$

Note that $\mathcal{F}\left(V_{A_C}\right)$ does not exist at $\bar{f}=0$, but $\mathcal{F}\left(\frac{\partial^{m+l+k}V_{A_C}(x,y,d+t)}{\partial x^m \partial y^l \partial z^k}\right)$ is well defined at $\bar{f}=0$ and equals to zero.

Its first term approximation gives:

$$\mathcal{F}\left(\frac{\partial^{m+l+k}V_{A_C}(x,y,d+t)}{\partial x^m \partial y^l \partial z^k}\right)$$
$$\approx (i2\pi f_1)^m (i2\pi f_2)^l (-2\pi\bar{f})^k 2\pi G(\rho_m-\rho_c)e^{-2\pi\bar{f}(d+t)}(2\pi\bar{f})^{-1}\mathcal{F}(u(x,y)) \quad (2.40)$$
$$= (i2\pi f_1)^m (i2\pi f_2)^l (-2\pi\bar{f})^{k-1} 2\pi G(\rho_c-\rho_w)e^{-2\pi\bar{f}(d+t)}\Phi_e(\bar{f})\mathcal{F}(b(x,y))$$

Now back to equation (2.26). The A_T can be computed using topography, and the A_C is approximately computed by the elastic plate model. If the density of the crust is assumed uniform, that is to say, $A_G = 0$ [*Barnes and Lumley*, 2011], and the isostatic compensation effect is removed or correctly computed, the topography could be estimated using free-air gravity anomaly.

2.1.4 Admittance Theory

Combining the first term approximation (2.31), (2.35) with (2.26) and assuming the density of crust is uniform, we have

$$\mathcal{F}(\Delta g_F) = -2\pi G(\rho_c-\rho_w)e^{-2\pi\bar{f}d}\left(1-\Phi_e(\bar{f})e^{-2\pi\bar{f}t}\right)\mathcal{F}(b(x,y)) \qquad (2.41)$$

In equation (2.41) the frequency parameter that modifies the seafloor topography so as to produce the free-air gravity anomaly is called the gravitational admittance $Z(\bar{f})$. It contains information about the compensation scheme. The theoretical gravitational admittance is

$$\begin{aligned} Z(\bar{f}) &= \frac{\mathcal{F}(\Delta g_F)}{\mathcal{F}(b)} \\ &= -2\pi G(\rho_c-\rho_w)e^{-2\pi\bar{f}d}\left(1-\Phi_e(\bar{f})e^{-2\pi\bar{f}t}\right) \end{aligned} \qquad (2.42)$$

Then (2.41) can be written as

$$\mathcal{F}(\Delta g_F) = Z(\bar{f})\mathcal{F}(b(x,y)) \qquad (2.43)$$

Similarly, the admittance that modifies the free-air gravity anomaly so as to produce the seafloor topography is

$$Q(\bar{f}) = \frac{\mathcal{F}(b)}{\mathcal{F}(\Delta g_F)} = \left(Z(\bar{f})\right)^{-1} \qquad (2.44)$$

The equation (2.43) provides a way to estimate the seafloor topography based upon the theoretical admittance if the geologic parameters in the admittance are well known.

$$\mathcal{F}\left(b(x,y)\right) = Q\left(\bar{f}\right)\mathcal{F}\left(\Delta g_F\right) \tag{2.45}$$

However, the uncertainty in the isostatic compensation scheme and the attenuation of the admittance at short and long wavelengths suggest that it is impractical, as analyzed below.

The compensation scheme affects the admittance function mainly in the long wavelengths. As seen in the top panel of Figure 2.3 which is computed using values from Table 2.1, at long wavelengths, the admittance function depends on and is sensitive to the choice of the effective elastic thickness of the plate T_e. That is to say, the estimated topography would severely deviate from reality if T_e contains an error, which in fact is uncertain to a large extent. But at short wavelengths, the differences between the compensated admittances and the uncompensated admittance are very small. Therefore, *Smith and Sandwell* [1994] confined the estimation within the uncompensated wavelength band to avoid modeling errors associated with the isostatic compensation. As shown in the bottom panel of Figure 2.3, the gradient admittance is less sensitive to the isostatic compensation parameter T_e. In this study, also only the uncompensated wavelengths of topography are to be estimated, which is even more justified when using gravity gradients as observations.

Figure 2.3 also shows that at long wavelengths the gravitational admittance $Z\left(\bar{f}\right)$ approaches zero because the long wavelength component of gravity generated by seafloor topography is canceled out by isostatic compensation, which means the gravity anomaly and topography are no longer correlated. At short wavelengths it also approaches zero due to the upward continuation operator $e^{-2\pi\bar{f}d}$ [*Forsberg and Kenyon*, 1995]. This operator attenuates the short wavelength component of gravity anomaly at the sea surface generated by the topography at the seafloor, so the signal-to-noise ratio is small and the short-wavelength gravity anomaly is less sensitive to the seafloor topography. As a result, $Q\left(\bar{f}\right)$ approaches infinity at both short and long wavelengths. At these wavelengths, a slight error in the gravity anomaly would be greatly enlarged and bring huge error to the predicted topography. In a word, estimating topography using gravity anomaly is stable only in a certain short-to-medium wavelength band (about 15-160 km). A detailed selection process for the cut-off frequencies can be found in [*Smith and Sandwell*, 1994]. In short, wavelengths longer than 160 km were suppressed so that the prediction is constrained to uncompensated bands. Wavelengths shorter than 15 km were removed to make the downward

continuation stable which, in any case, is achieved by minimizing the mean square error of the downward continued gravity anomaly. Rearranging equation (2.31), multiplying both sides by the band-pass filter, and omitting the isostatic compensation, we have

$$\mathcal{F}\left(b(x,y)\right)W\left(\bar{f}\right) = -\left[2\pi G\left(\rho_c - \rho_w\right)\right]^{-1} e^{2\pi \bar{f} d}\,\mathcal{F}\left(\Delta g_F\right)W\left(\bar{f}\right) \qquad (2.46)$$

where $W\left(\bar{f}\right)$ is the band-pass filter. This is the linear approximation to the relation between topography and gravity anomaly at uncompensated wavelengths.

Table 2.1: Parameters used to calculate the admittances in Figure 2.3.

Parameter	Value
ρ_w, density of sea water	1030 kg / m^3
ρ_c, density of the crust	2800 kg / m^3
ρ_m, density of the mantle	3330 kg / m^3
d, mean depth of sea water	4500 m
t, mean thickness of the crust	6000 m
E, Young's modulus	$7*10^{10}$ $kg\ m^{-1}s^{-2}$
ν, Poisson's ratio	0.27

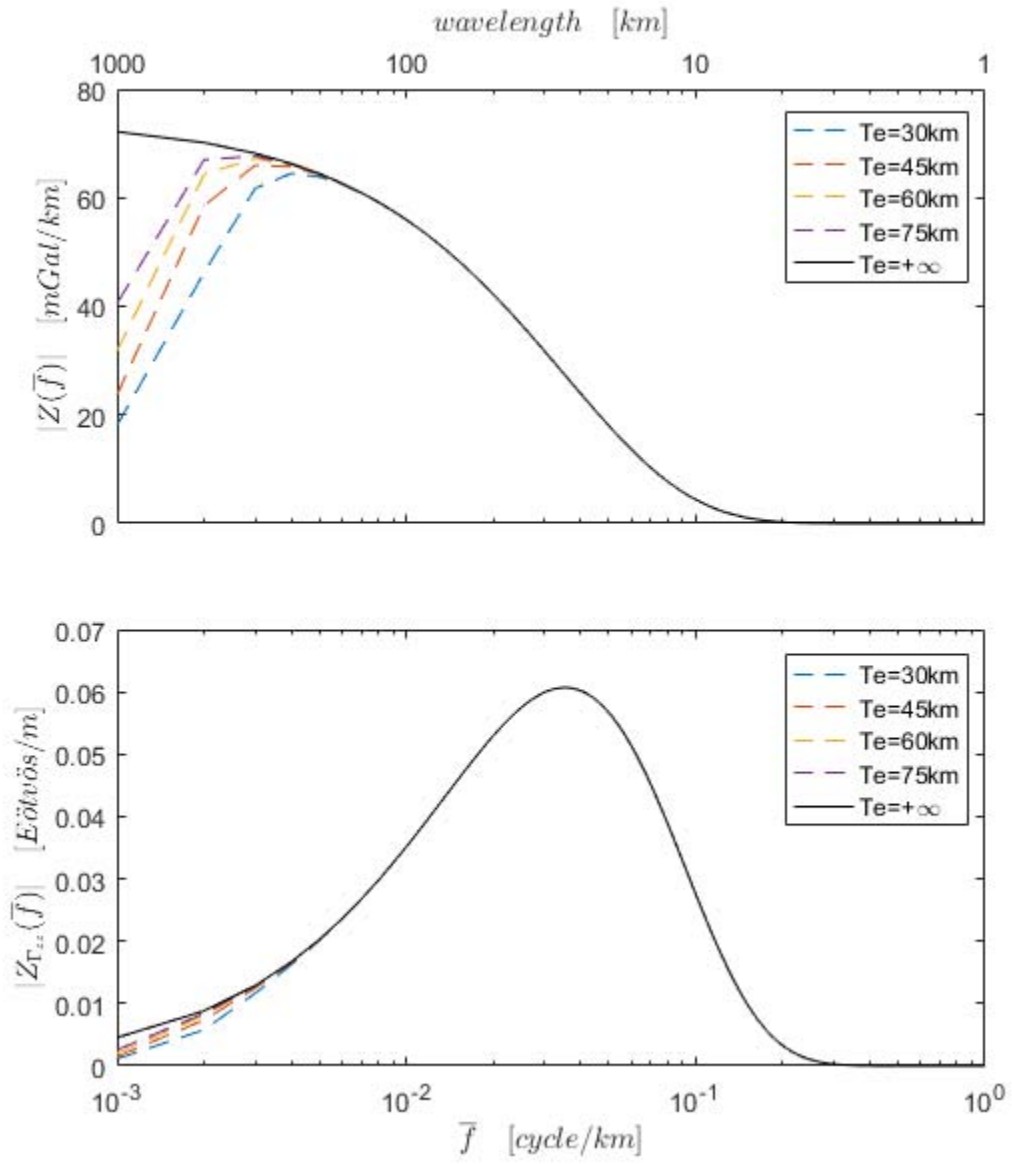

Figure 2.3: (top) The theoretical gravitational admittance. (bottom) The theoretical gravity gradient admittance. Scale at bottom in frequency and at top in wavelength. The solid curve is for the isostatically uncompensated model. The dashed curves are for the regionally isostatically compensated model with respect to different effective elastic thickness of the plate T_e.

Note that if $T_e \to 0$ the compensation model becomes local (Airy model) rather than regional. If $T_e \to +\infty$ there is no compensation ($\Phi_e\left(\overline{f}\right) = 0$).

Now let us discuss the gravity gradient admittance. Combining (2.33) (2.40) and assuming that the measured gravity gradient is only caused by the topography and isostatic compensation, we have:

$$\begin{aligned}&\mathscr{F}\left(\frac{\partial^{m+l+k}V}{\partial x^m \partial y^l \partial z^k}\right)\\ &\approx -\left(i2\pi f_1\right)^m \left(i2\pi f_2\right)^l \left(-2\pi\overline{f}\right)^{k-1} 2\pi G\left(\rho_c-\rho_w\right)e^{-2\pi\overline{f}d}\left(1-\Phi_e\left(\overline{f}\right)e^{-2\pi\overline{f}t}\right)\mathscr{F}\left(b(x,y)\right)\end{aligned} \tag{2.47}$$

According to (2.47), the compensated gravity gradient admittances with respect to each tensor element are:

$$\begin{aligned}
Z_{\Gamma_{zz}} &= \frac{\mathscr{F}\left(\Gamma_{zz}\right)}{\mathscr{F}\left(b(x,y)\right)} = 4\pi^2\overline{f}G\left(\rho_c-\rho_w\right)e^{-2\pi\overline{f}d}\left(1-\Phi_e\left(\overline{f}\right)e^{-2\pi\overline{f}t}\right)\\
Z_{\Gamma_{yy}} &= \frac{\mathscr{F}\left(\Gamma_{yy}\right)}{\mathscr{F}\left(b(x,y)\right)} = -4\pi^2 f_2^2\overline{f}^{-1}G\left(\rho_c-\rho_w\right)e^{-2\pi\overline{f}d}\left(1-\Phi_e\left(\overline{f}\right)e^{-2\pi\overline{f}t}\right)\\
Z_{\Gamma_{xx}} &= \frac{\mathscr{F}\left(\Gamma_{xx}\right)}{\mathscr{F}\left(b(x,y)\right)} = -4\pi^2 f_1^2\overline{f}^{-1}G\left(\rho_c-\rho_w\right)e^{-2\pi\overline{f}d}\left(1-\Phi_e\left(\overline{f}\right)e^{-2\pi\overline{f}t}\right)\\
Z_{\Gamma_{xy}} &= \frac{\mathscr{F}\left(\Gamma_{xy}\right)}{\mathscr{F}\left(b(x,y)\right)} = -4\pi^2 f_1 f_2\overline{f}^{-1}G\left(\rho_c-\rho_w\right)e^{-2\pi\overline{f}d}\left(1-\Phi_e\left(\overline{f}\right)e^{-2\pi\overline{f}t}\right)\\
Z_{\Gamma_{yz}} &= \frac{\mathscr{F}\left(\Gamma_{yz}\right)}{\mathscr{F}\left(b(x,y)\right)} = -i4\pi^2 f_2 G\left(\rho_c-\rho_w\right)e^{-2\pi\overline{f}d}\left(1-\Phi_e\left(\overline{f}\right)e^{-2\pi\overline{f}t}\right)\\
Z_{\Gamma_{zx}} &= \frac{\mathscr{F}\left(\Gamma_{zx}\right)}{\mathscr{F}\left(b(x,y)\right)} = -i4\pi^2 f_1 G\left(\rho_c-\rho_w\right)e^{-2\pi\overline{f}d}\left(1-\Phi_e\left(\overline{f}\right)e^{-2\pi\overline{f}t}\right)
\end{aligned} \tag{2.48}$$

where $\left\{\Gamma_{ij} \mid i,j \in \{x,y,z\}\right\}$ represent the gravity gradient tensor elements.

The gravity gradient admittances calculated using parameters in Table 2.1 are shown in Figure 2.4.

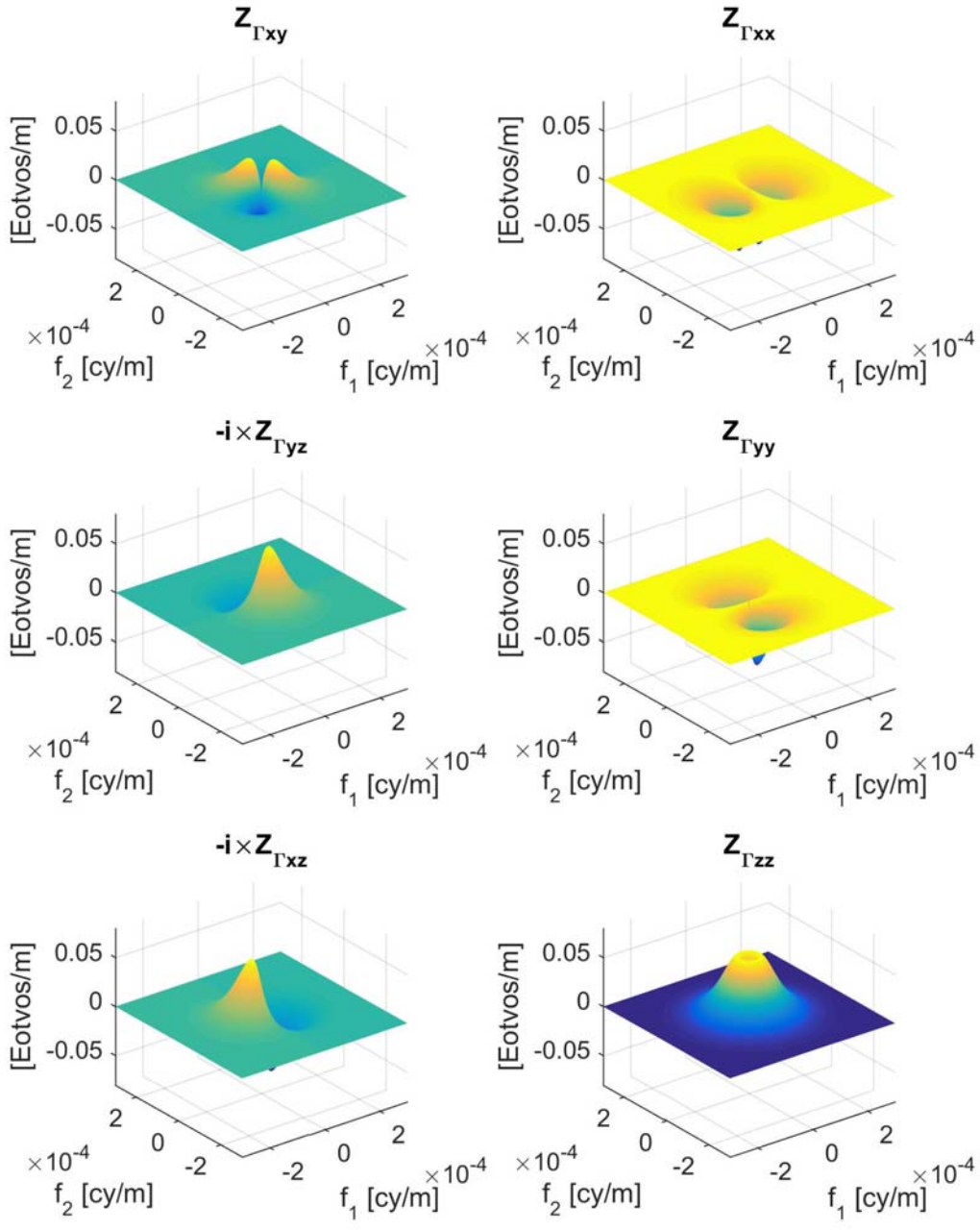

Figure 2.4: The theoretical gravity gradient admittances for combined seafloor topography and isostatic compensation.

Like the gravitational admittance, the gravity gradient admittance for the component Γ_{zz} is isotropic. After removing the short and long wavelengths at which the gradient admittance $Z_{\Gamma_{zz}}$ approximates zero (see the bottom panel of Figure 2.3), as well as the compensated wavelengths, estimating seafloor topography using Γ_{zz} is stable:

$$\begin{aligned}\mathcal{F}\left(\Gamma_{zz}\right)\cdot W\left(\bar{f}\right) &= Z_{\Gamma_{zz}}\mathcal{F}\left(b\right)\cdot W\left(\bar{f}\right)\\ &= 4\pi^2\bar{f}G\left(\rho_c-\rho_w\right)e^{-2\pi\bar{f}d}\mathcal{F}\left(b\right)\cdot W\left(\bar{f}\right)\end{aligned} \tag{2.49}$$

where $W\left(\bar{f}\right)$ is a band-pass filter.

Rearrange equation (2.49) and take the inverse Fourier Transform on both sides to obtain

$$\mathcal{F}^{-1}\left[\mathcal{F}\left(b\right)\cdot W\left(\bar{f}\right)\right]=\left[2\pi G\left(\rho_c-\rho_w\right)\right]^{-1}\mathcal{F}^{-1}\left[\left(2\pi\bar{f}\right)^{-1}e^{2\pi\bar{f}d}\mathcal{F}\left(\Gamma_{zz}\right)\cdot W\left(\bar{f}\right)\right] \tag{2.50}$$

Note that the gravity gradient admittances for the other elements of the gravity gradient tensor are anisotropic and thus require anisotropic filters. But the combinations of tensor elements could yield quantities that have isotropic admittances (e.g. $\sqrt{\Gamma_{xz}^2+\Gamma_{yz}^2}$). Combining independent gravity gradient tensor elements incorporates more data and thus may improve the accuracy of topography estimation. This study only uses the vertical gravity gradient Γ_{zz} derived from satellite altimetry to estimate the seafloor topography.

2.1.5 Advantages and Limitations of Using the Gravity Gradient

By comparing the two panels in Figure 2.3, the isostatic compensation was found to have smaller effect on the gravity gradient admittance than on the gravitational admittance. This is due to the $-2\pi\bar{f}$ factor in the gradient admittance, which makes the vertical gravity gradient less sensitive to the long wavelength topography.

On the other hand, the gravity gradient admittance reaches its maximum at wavelength 75 km, whereas the peak of the gravitational admittance is at the longer wavelength of 200 km. This difference is even larger if we use a smaller mean sea depth. This indicates that, compared to the gravity anomaly, the gravity gradient is more sensitive to short wavelength topography. We may conclude that the gravity gradient is superior to the gravity anomaly at short wavelengths when predicting topography.

One should note that the gravity gradient diminishes with the cube of distance between the mass element and the attracted point, while gravity attenuates with the square of distance. So for deep ocean areas the magnitude of the gravity gradient at the sea surface may be small, which then also implies a small signal-to-noise ratio. For these areas the superiority of the gravity gradient at short wavelengths may be cancelled by the low signal-to-noise ratio because the attenuation rate of gravity anomaly is slower.

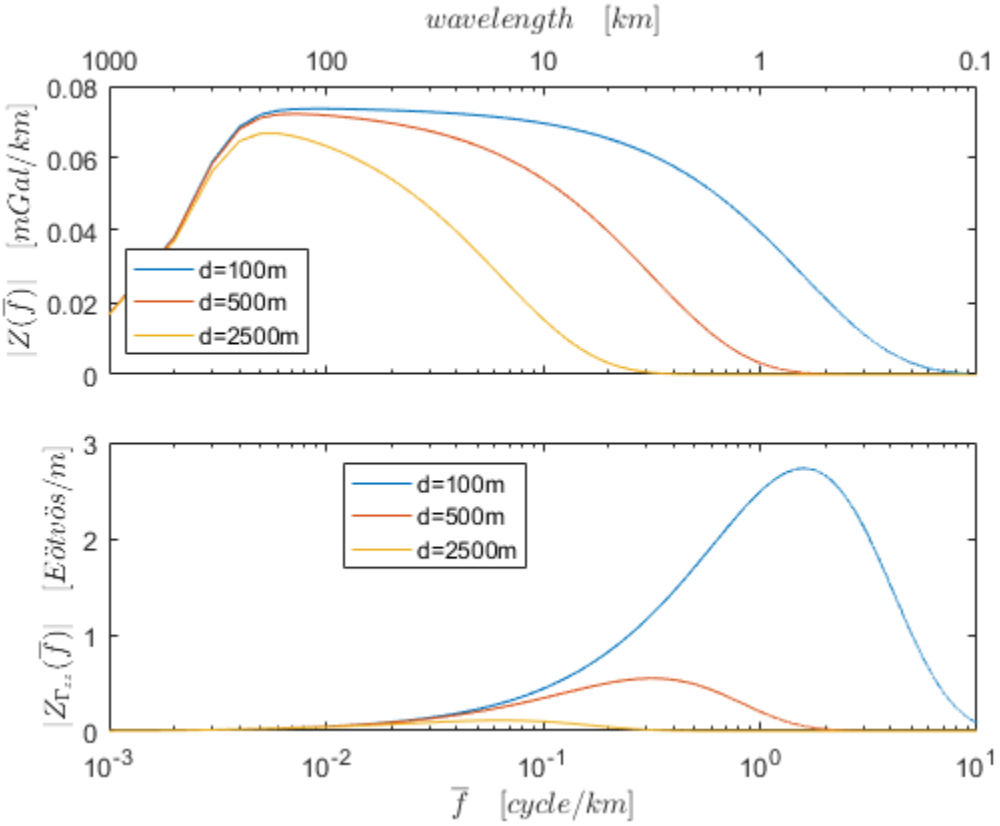

Figure 2.5: The gravitational admittance and gravity gradient admittance with respect to mean sea depth d .

The variation of admittance with respect to mean sea depth is shown in Figure 2.5. As the mean sea depth increases, the gravity gradient admittance decreases fast, and the peak of the admittance gradually moves to longer wavelengths. Although the gravitational admittance also decreases when mean sea depth increases, the change rate is comparatively slower.

2.2 Relationship in the Spatial Domain

2.2.1 The Gravitational Gradients Due to a Right Rectangular Prism

The last section serves as the theoretical basis for the Parker FFT-based seafloor topography estimation method developed in section 3.1. Except for the frequency domain, the gravity gradient can be related to the topography in the space domain. The seafloor topography can be modeled using adjacent right rectangular prisms as illustrated in Figure 2.6.

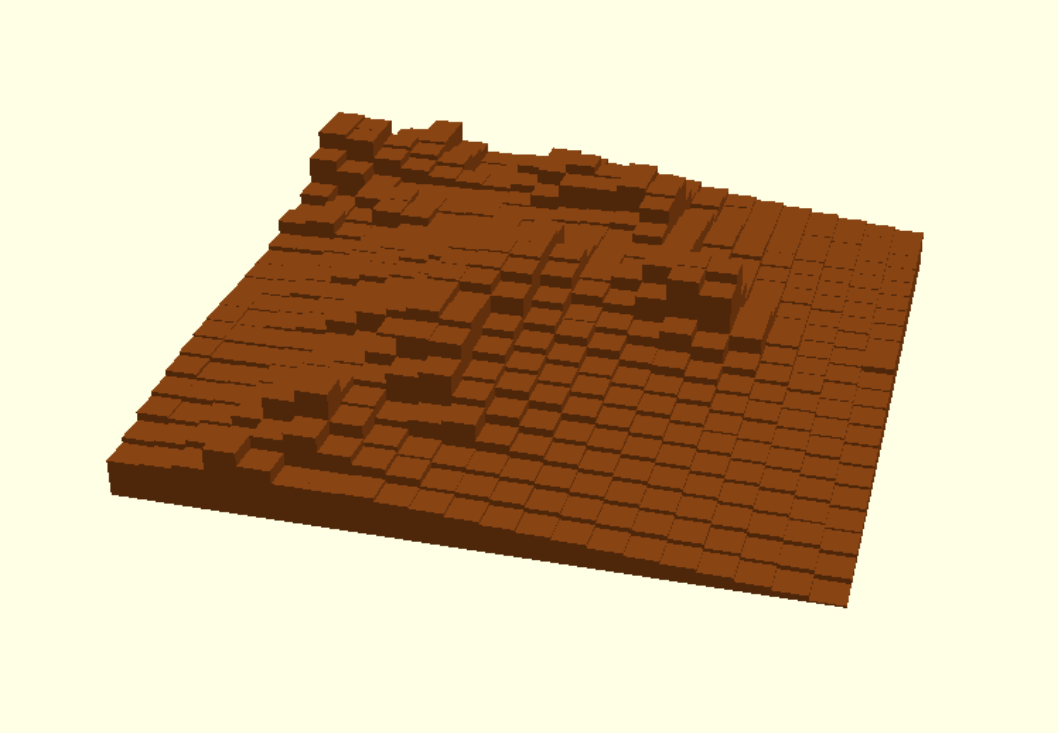

Figure 2.6: Model the seafloor topography using right rectangular prisms.

The gravitational gradients due to a right rectangular prism can be computed using [*Zhu*, 2007]

$$ {}^{i}\Gamma_{zz}^{comp}\left(b_j\right) = G\Delta\rho \arctan \frac{(x-\xi)(y-\eta)}{(z-\zeta)\sqrt{(x-\xi)^2+(y-\eta)^2+(z-\zeta)^2}} \Bigg|_{\xi=\mathrm{xw}_j}^{\mathrm{xe}_j} \Bigg|_{\eta=\mathrm{ys}_j}^{\mathrm{yn}_j} \Bigg|_{\zeta=md_j}^{b_j} \tag{2.51} $$

where ${}^{i}\Gamma_{zz}^{comp}\left(b_j\right)$ is the vertical gravity gradient at i due to prism j, G is Newton's gravitational constant, $\Delta\rho$ is the density difference between sea water and seafloor topography, (x,y,z) are the coordinates of the location of observation point i, (ξ,η,ζ) are the variables of integration over the right rectangular prism, xw_j, xe_j, ys_j, yn_j are the X-axis and Y-axis boundaries for the *jth* prism, md_j is the Z-coordinate of mean depth at j, and b_j is the Z-coordinate of seafloor at j.

The forward computation formula (2.51) is used in the simulated annealing method developed in section 3.3 for seafloor topography estimation.

2.3 Errors Associated with Gradient Inversion Techniques

2.3.1 Truncation and Resolution Errors in the Forward Computation

In practice, the gravity gradient is forward computed from a discrete digital topography model (Figure 2.6) within a preset near zone. For each computation point, its *near zone* is defined as the area in which the horizontal distance between a prism and the computation point is within a preset truncation distance. Area outside the near zone is defined as *far zone*. The *truncation error* is defined as the error at one point caused by neglecting the far zone effect in the forward computation. In this analysis, the truncation error was assumed as long-wavelength and was approximated by a constant. In order to validate this assumption, one can compute the *relative truncation error*, which is the difference between truncation errors of two points both in the study area but separated by a horizontal distance l. If the relative truncation error is small, then we could use just one parameter to represent the truncation errors in the entire area, see formula (3.42). If the relative truncation error is large, then our assumption that the truncation error is a constant is not tenable. In addition, the forward computation uses discrete topography with finite resolution, and thus causes an error called the *resolution error*. *Jekeli* [2013a] developed a systematic and algorithmic approach to estimate the relative truncation error and resolution error. This subsection analyzes the errors in the forward computation associated with a numerical implementation.

The equation (2.20) can be rewritten as

$$\Gamma_{zz}(x,y,z)=G\rho\iint_{\sigma}F'_{zz}(s)b(\xi,\eta)\,d\sigma-G\rho\bar{b}\breve{F}'_{zz}(0). \qquad (2.52)$$

Suppose the near zone is defined as

$$\sigma'(s_0)=\left\{(\xi,\eta)\left|\sqrt{(x-\xi)^2+(y-\eta)^2}\le s_0\right.\right\};\tag{2.53}$$

then the truncation error is given by a convolution

$$\varepsilon_{zz}^{trunc}(x,y)=-G\rho\iint_{\sigma}\omega_{zz}(s)b(\xi,\eta)\,d\sigma,\tag{2.54}$$

where

$$\omega_{zz}(s)=\begin{cases}0 & s\le s_0\\ F'_{zz}(s) & s>s_0\end{cases}.\tag{2.55}$$

Take the Fourier transform on both sides of (2.54) and we have

$$\breve{\varepsilon}_{zz}^{trunc}(f_1,f_2)=-G\rho\breve{\omega}_{zz}(\overline{f})\breve{b}(f_1,f_2),\tag{2.56}$$

where

$$\breve{\omega}_{zz}(\overline{f})=(2\pi)^2\,\overline{f}e^{-2\pi(z_0-\overline{b})\overline{f}}+2\pi\int_{s'=0}^{s_0}\left[\frac{1}{\left[s'^2+(z_0-\overline{b})^2\right]^{\frac{3}{2}}}-\frac{3(z_0-\overline{b})^2}{\left[s'^2+(z_0-\overline{b})^2\right]^{\frac{5}{2}}}\right]J_0(2\pi\overline{f}s')s'ds'\tag{2.57}$$

Next, assume the topography is an ergodic stochastic process, then its power spectral density is related to its Fourier transform through [*Bendat and Piersol*, 2010]

$$\Phi_b(f_1,f_2)=\lim_{T_x\to\infty}\lim_{T_y\to\infty}E\left[\frac{1}{T_xT_y}\breve{b}^*_{T_x,T_y}(f_1,f_2)\breve{b}_{T_x,T_y}(f_1,f_2)\right],\tag{2.58}$$

where the asterisk denotes complex conjugate, E is the expectation, and $\breve{b}_{T_x,T_y}(f_1,f_2)$ is the Fourier transform of the topography in the finite interval T_x, T_y along the X and Y axis, respectively. Note that T_x and T_y are limits for the entire topography model. They are not to be confused with the truncation distance. Each computation point has a near zone. Truncation distance is the limit for the near zone.

The power spectral density (2.58) was azimuthally averaged to form an isotropic function in order to simplify the analysis.

$$\bar{\Phi}_b\left(\bar{f}\right)=\frac{1}{2\pi}\int_{\psi=0}^{2\pi}\Phi_b\left(\bar{f}\cos\psi,\bar{f}\sin\psi\right)d\psi \tag{2.59}$$

Neglecting the limits and expectation in (2.58) gives a practical way to evaluate the power spectral density. It is called the periodogram method. The periodogram of the truncation error derived from (2.56) is given by

$$\Phi_{\varepsilon_{zz}^{trunc}}\left(\bar{f}\right)=\left(G\rho\right)^2\left|\breve{\omega}_{zz}\left(\bar{f}\right)\right|^2\bar{\Phi}_b\left(\bar{f}\right). \tag{2.60}$$

The inverse Hankel transform of (2.60) gives the covariance function,

$$\phi_{\varepsilon_{zz}^{trunc}}\left(s'\right)=2\pi\int_{\bar{f}=0}^{\infty}\Phi_{\varepsilon_{zz}^{trunc}}\left(\bar{f}\right)J_0\left(2\pi\bar{f}s'\right)\bar{f}d\bar{f} \tag{2.61}$$

And, the variance of the truncation error for points separated by distance, l, is

$$\left(\sigma_{\varepsilon_{zz}^{trunc}}\right)^2=\phi_{\varepsilon_{zz}^{trunc}}\left(0\right)=2\pi\int_{\bar{f}=0}^{\infty}\Phi_{\varepsilon_{zz}^{trunc}}\left(\bar{f}\right)\bar{f}d\bar{f}\,. \tag{2.62}$$

The variance of the relative truncation error is

$$\begin{aligned}\left(\sigma_{\Delta\varepsilon_{zz}^{trunc}}\right)^2&=2\left[\phi_{\varepsilon_{zz}^{trunc}}\left(0\right)-\phi_{\varepsilon_{zz}^{trunc}}\left(l\right)\right]\\&=4\pi\int_{\bar{f}=0}^{\infty}\Phi_{\varepsilon_{zz}^{trunc}}\left(\bar{f}\right)\left[1-J_0\left(2\pi\bar{f}l\right)\right]\bar{f}d\bar{f}\\&=4\pi\left(G\rho\right)^2\int_{\bar{f}=0}^{\infty}\left|\breve{\omega}_{zz}\left(\bar{f}\right)\right|^2\bar{\Phi}_b\left(\bar{f}\right)\left[1-J_0\left(2\pi\bar{f}l\right)\right]\bar{f}d\bar{f}\end{aligned} \tag{2.63}$$

If the topography is given on a grid $b\left(x,y\right)=b\left(l_x\Delta x,l_y\Delta y\right)$, $l_x=0,1,\cdots,N_x-1$, $l_y=0,1,\cdots,N_y-1$, then its discrete Fourier transform is given by

$$\breve{b}_{k_1,k_2}=\Delta x\Delta y\sum_{l_x=-\frac{N_x}{2}}^{\frac{N_x}{2}-1}\sum_{l_y=-\frac{N_y}{2}}^{\frac{N_y}{2}-1}b_{l_x,l_y}e^{-i2\pi\left(\frac{k_1l_x}{N_x}+\frac{k_2l_y}{N_y}\right)} \tag{2.64}$$

where the indices k_1, k_2 count off frequencies, $f_{k_1} = \dfrac{k_1}{\Delta x N_x}$ and $f_{k_2} = \dfrac{k_2}{\Delta y N_y}$, respectively. If N_x is even, $-\dfrac{N_x}{2} \le k_1 \le \dfrac{N_x}{2} - 1$, and if N_x is odd, $-\dfrac{N_x - 1}{2} \le k_1 \le \dfrac{N_x - 1}{2}$, and similarly for f_{k_2}.

The power spectral density of topography $\bar{\Phi}_b\left(\bar{f}\right)$ in (2.63) can be computed by azimuthally averaging the periodogram,

$$\left(\bar{\Phi}_b\right)_k = \frac{1}{M_k} \sum_{\bar{f}_{k-1} < \sqrt{f_{k_1}^2 + f_{k_2}^2} \le \bar{f}_k} \frac{1}{\Delta x N_x \Delta y N_y} \breve{b}^*_{k_1,k_2} \breve{b}_{k_1,k_2} \qquad k = 1, 2, \cdots, M \tag{2.65}$$

where M_k is the number of discrete frequencies pairs f_{k_1}, f_{k_2} whose corresponding radial frequency lies in the interval $\left(\bar{f}_{k-1}, \bar{f}_k\right]$. Note that $\bar{f}_M \le \min\left(\dfrac{1}{2\Delta x}, \dfrac{1}{2\Delta y}\right)$.

The quantity $\left(\breve{\omega}_{zz}\right)_k = \breve{\omega}_{zz}\left(\bar{f}_k\right)$ can be numerically computed from (2.57). In summary, the variance of the relative truncation error (2.63) can be estimated by

$$\left(\sigma_{\Delta\varepsilon_{zz}^{trunc}}\right)^2 = 4\pi (G\rho)^2 \Delta\bar{f} \sum_{k=1}^{M} \left|\left(\breve{\omega}_{zz}\right)_k\right|^2 \left(\bar{\Phi}_b\right)_k \left[1 - J_0\left(2\pi \bar{f}_k l\right)\right] \bar{f}_k \tag{2.66}$$

where $\Delta\bar{f} = \bar{f}_k - \bar{f}_{k-1} = \text{constant}$.

Similarly, the variance of the truncation error

$$\begin{aligned} \left(\sigma_{\varepsilon_{zz}^{trunc}}\right)^2 &= \phi_{\varepsilon_{zz}^{trunc}}(0) \\ &= 2\pi \int_{\bar{f}=0}^{\infty} \Phi_{\varepsilon_{zz}^{trunc}}\left(\bar{f}\right) \bar{f} d\bar{f} \\ &= 2\pi (G\rho)^2 \int_{\bar{f}=0}^{\infty} \left|\breve{\omega}_{zz}\left(\bar{f}\right)\right|^2 \bar{\Phi}_b\left(\bar{f}\right) \bar{f} d\bar{f} \end{aligned} \tag{2.67}$$

can be numerically estimated by

$$\left(\sigma_{\varepsilon_{zz}^{trunc}}\right)^2 = 2\pi (G\rho)^2 \Delta\bar{f} \sum_{k=1}^{M} \left|\left(\breve{\omega}_{zz}\right)_k\right|^2 \left(\bar{\Phi}_b\right)_k \bar{f}_k \tag{2.68}$$

The topography grid does not contain spectral components higher than the Nyquist frequencies, which are determined by the sampling intervals Δx and Δy. The error thus introduced is called the resolution error. Its Fourier transform is given by

$$\breve{\varepsilon}_{zz}^{res}\left(f_1,f_2\right)=\begin{cases}0 & \left|f_1\right|\le\dfrac{1}{2\Delta x}\ \&\ \left|f_2\right|\le\dfrac{1}{2\Delta y}\\ -\breve{\Gamma}_{zz}\left(f_1,f_2\right) & otherwise\end{cases} \tag{2.69}$$

With equation (2.22), the power spectral density of the resolution error is

$$\Phi_{\varepsilon_{zz}^{res}}\left(\bar{f}\right)\approx\begin{cases}0 & \left|\bar{f}\right|\le\bar{f}_N\\ \left(G\rho\right)^2\left|\breve{F}'_{zz}\left(\bar{f}\right)-\breve{F}'_{zz}\left(0\right)\delta\left(\bar{f}\right)\right|^2\bar{\Phi}_b\left(\bar{f}\right) & \left|\bar{f}\right|>\bar{f}_N\end{cases} \tag{2.70}$$

where we assume $\Delta x\approx\Delta y$, and approximate the "radial" Nyquist frequency by $\bar{f}_N=\sqrt{\left(\dfrac{1}{2\Delta x}\right)^2+\left(\dfrac{1}{2\Delta y}\right)^2}$.

Analogous to (2.62), the variance of the resolution error is given by

$$\left(\sigma_{\varepsilon_{zz}^{res}}\right)^2=2\pi\int_{\bar{f}=\bar{f}_N}^{\infty}\Phi_{\varepsilon_{zz}^{res}}\left(\bar{f}\right)\bar{f}d\bar{f} \tag{2.71}$$

If the power spectral density of the topography is approximated by a power law [*Jekeli*, 2013a]

$$\bar{\Phi}_b\left(\bar{f}\right)=C\bar{f}^{-\beta}, \tag{2.72}$$

then (2.71) becomes

$$\begin{aligned}\left(\sigma_{\varepsilon_{zz}^{res}}\right)^2&=\left(2\pi\right)^5\left(G\rho\right)^2C\int_{\bar{f}=\bar{f}_N}^{\infty}e^{-4\pi\left(z_0-\bar{b}\right)\bar{f}}\bar{f}^{-\beta+3}d\bar{f}\\&=2^{2\beta-3}\pi^{\beta+1}\left(G\rho\right)^2C\left(z_0-\bar{b}\right)^{\beta-4}\Gamma^{uigf}\left[4-\beta,4\pi\left(z_0-\bar{b}\right)\bar{f}_N\right]\end{aligned}, \tag{2.73}$$

where $\Gamma^{uigf}\left(p,z\right)$ represents the upper incomplete gamma function [*Abramowitz and Stegun*, 1972].

2.3.2 Summary of Other Error Sources

The density of the seafloor topography is assumed uniform throughout this study. In reality, the sub-topography density anomaly is large in some areas, and may contribute to more than 50% of the gravity gradient observations (see section 5.1).

In this study, the planar approximation is made when using the altimetry derived gravity gradients, whereas local Cartesian coordinates are used without any approximation when using the airborne gravity gradients.

Subtracting (2.33) from (2.32) gives the nonlinear approximation error for Γ_{zz}

$$\varepsilon_{nonlinear}\left(\Gamma_{zz}\right) = 2\pi G\left(\rho_c - \rho_w\right) e^{-2\pi \bar{f} d} \sum_{n=2}^{\infty} \frac{\left(2\pi \bar{f}\right)^n}{n!} \mathcal{F}\left(b^n\left(x, y\right)\right) \qquad (2.74)$$

This error is discussed in section 3.2. Numerical analysis in subsection 3.2.1 showed that in rugged areas (topography ranges from -1000 m to -5000 m over a 200 km by 200 km rectangular area), the nonlinear approximation error can be as much as 49 Eötvös.

The depths measured by ship sounding do not come with accuracy information. They are treated as errorless (true) values, because an analysis of 2253 cruises surveys shows that the median absolute value of the crossover errors at intersecting ship tracks is 26 m [*Smith*, 1993], which is much smaller than the accuracy of gravity predicted seafloor topography. The accuracy of the altimetry-derived gravity anomaly released by Scripps Institution of Oceanography is ±2 mGal [*Sandwell et al.*, 2014]. The accuracy of the vertical gravity gradient derived from the same altimetry data sets is not reported. A rough analysis by applying the law of error propagation to equation (A6) in [*Sandwell and Smith*, 1997], with the derivatives of the vertical deflections substituted by a numerical differentiation formula, shows that the accuracy of vertical gravity gradient released by SIO is about ±4 Eötvös.

Chapter 3: Estimation Methodology

3.1 Seafloor Topography Estimation Based on Fourier Transform

Equation (2.50) indicates that, when band-pass filtered and multiplied by $\left(2\pi\overline{f}\right)^{-1} e^{2\pi\overline{f}d}$, the vertical gravity gradient becomes what may be called an "equivalent gravity anomaly" that is proportional to the topography in both the frequency and the spatial domains. In other words, multiplying the equivalent gravity anomaly by a scaling factor gives the intermediate wavelength component of the topography. The constant, $S = \left[2\pi G\left(\rho_c - \rho_w\right)\right]^{-1}$ in (2.50), is defined as the theoretical value of the "topography-to-gradient admittance scale". It describes the uncompensated relation between topography and gravity gradient under a constant density assumption. But equation (2.50) is just a first-term approximation to Parker's infinite series. The error caused by neglecting the nonlinear terms is affected by the roughness of the seafloor topography. In addition, it is assumed that the density of the crust is uniform. Due to these two location dependent factors, the topography-to-gradient admittance scale deviates from its theoretical value and varies from place to place, therefore the empirical rather than the theoretical S is used in the prediction to enable local dependency. The scale S is computed using gravity gradient and topography pairs at places constrained by ship soundings.

In summary, the short-to-intermediate wavelength seafloor topography $\hat{b}_{si}$ is estimated from the gravity gradient:

$$\hat{b}_{si} = S \cdot \mathcal{F}^{-1}\left[\left(2\pi\overline{f}\right)^{-1} e^{2\pi\overline{f}d}\, \mathcal{F}\left(\Gamma_{zz}\right) \cdot W\right] \tag{3.1}$$

Note that the prediction band is the same as the one for the gravity anomaly (15-160 km) [*Smith and Sandwell*, 1994] because the derived gradients do not have higher resolution.

The long wavelength topography $\hat{b}_l$ is computed from ship sounding b:

$$\hat{b}_l = \mathcal{F}^{-1}\left[\mathcal{F}\left(b\right) \cdot W_l\right] \tag{3.2}$$

where W_l is the low-pass filter.

The sum of $\hat{b}_{si}$ and $\hat{b}_l$ gives the total predicted topography.

$$\hat{b} = \hat{b}_l + \hat{b}_{si} \tag{3.3}$$

The short wavelengths are omitted. They could only be obtained through multi-beam swath-mapping system.

3.2 Analysis to the Nonlinear Terms

3.2.1 Validity of the Linear Approximation

The algorithm developed in the last section is based on the assumption that the seafloor topography and the vertical gravity gradient are related by the first-term approximation in Parker's theory. In this section, the validity of this assumption is analyzed.

To be specific, equation (2.32) describes the nonlinear relation between gravity gradient and seafloor topography. It is rewritten here as

$$\mathcal{F}\left(\Gamma_{jk}\right) = \mu_{jk}\mathcal{F}\left(V_{A_T}\right) = \mu_{jk}\cdot 2\pi G\left(\rho_c - \rho_w\right)e^{-2\pi\bar{f}d}\sum_{n=1}^{\infty}\frac{\left(2\pi\bar{f}\right)^{n-2}}{n!}\mathcal{F}\left(b^n\left(x,y\right)\right) \tag{3.4}$$

where $j,k \in \{x,y,z\}$ and

$$\begin{array}{lll} \mu_{xx} = -4\pi^2 f_1^2 & \mu_{yx} = -4\pi^2 f_1 f_2 & \mu_{zx} = -i4\pi^2 f_1 \bar{f} \\ & \mu_{yy} = -4\pi^2 f_2^2 & \mu_{zy} = -i4\pi^2 f_2 \bar{f} \\ & & \mu_{zz} = 4\pi^2 \bar{f}^2 \end{array} \tag{3.5}$$

The linear term (n=1 term) in (3.4) was assumed to be dominant in the frequency domain inversion method (section 3.1), and the nonlinear terms (n>1 terms) negligible. Note that $\mathcal{F}\left(V_{A_T}\right)$ does not exist at $\bar{f}=0$ due to the $\bar{f}^{-1}$ in the $n=1$ term. But $\mathcal{F}\left(\Gamma_{jk}\right)$ is well defined at $\bar{f}=0$ since $\lim\limits_{\substack{f_1\to 0\\ f_2\to 0}} f_2^2\bar{f}^{-1} = \lim\limits_{\substack{f_1\to 0\\ f_2\to 0}} f_1^2\bar{f}^{-1} = \lim\limits_{\substack{f_1\to 0\\ f_2\to 0}} f_1 f_2\bar{f}^{-1} = 0$ [*Zhu*, 2007].

$b(x,y)$ is the deviation of the actual topography from the reference plane $z=-d$, as shown in Figure 2.1. The selection of this reference plane is entirely arbitrary because the vertical gravity gradient effect due to an infinite horizontal slab with uniform density is zero. As long as $d > \max|b|$, the series (3.4) converges [*Parker*, 1973]. Moreover, Parker (1973) shows that the rate of convergence depends on the ratio, $\max|b|/d$, where a smaller value leads to a faster rate. Thus, one should choose the mean seafloor depth as the reference plane to obtain the fastest rate of convergence, i.e. to let the series concentrate on the n=1 term.

The last paragraph indicates why the error introduced by neglecting the nonlinear terms is larger in rough areas. Let us consider two areas with the same mean seafloor depth d: one smooth area with smaller $\max|b|$, and one rugged area with larger $\max|b|$. More percentage of the infinite series value is concentrated on the $n=1$ term in the smooth area than in the rough area, because in the smooth area smaller $\max|b|/d$ leads to a faster convergence rate. This conclusion is illustrated in the following example.

The digital elevation models (DEM) of one smooth and one rugged area were synthesized to analyze the dominance of the $n=1$ term. The bathymetric depth grid (refer to subsection 4.2.1 for detailed description of the data) in Figure 4.3 was used to construct the simulated DEM for the rugged area. Depth at each grid point remains unchanged but was assigned a new X and Y coordinates as if the topography was sampled from Cartesian coordinates with interval of 1713.8 m along the west-east direction and 1839.4 m along the south-north direction. In this way, the roughness of the simulated DEM is in the same order as the study area of section 4.1. Then the Z axis origin was translated from sea level to the mean depth and this model was treated as the rugged area (lower panel of Figure 3.1). The purpose of the translation is to let Parker's series concentrate on the n=1 term. The DEM of the smooth area was built in the same way, except that the magnitude of bathymetric depth was divided by 10 (upper panel of Figure 3.1). The vertical gravitational gradients at constant altitude $z=4530.3\,m$ and above the center of each area were computed through formula (3.4). It can be seen that every parameter in (3.4) for the two areas is the same except the topography b. The computation results are shown in Figure 3.2.

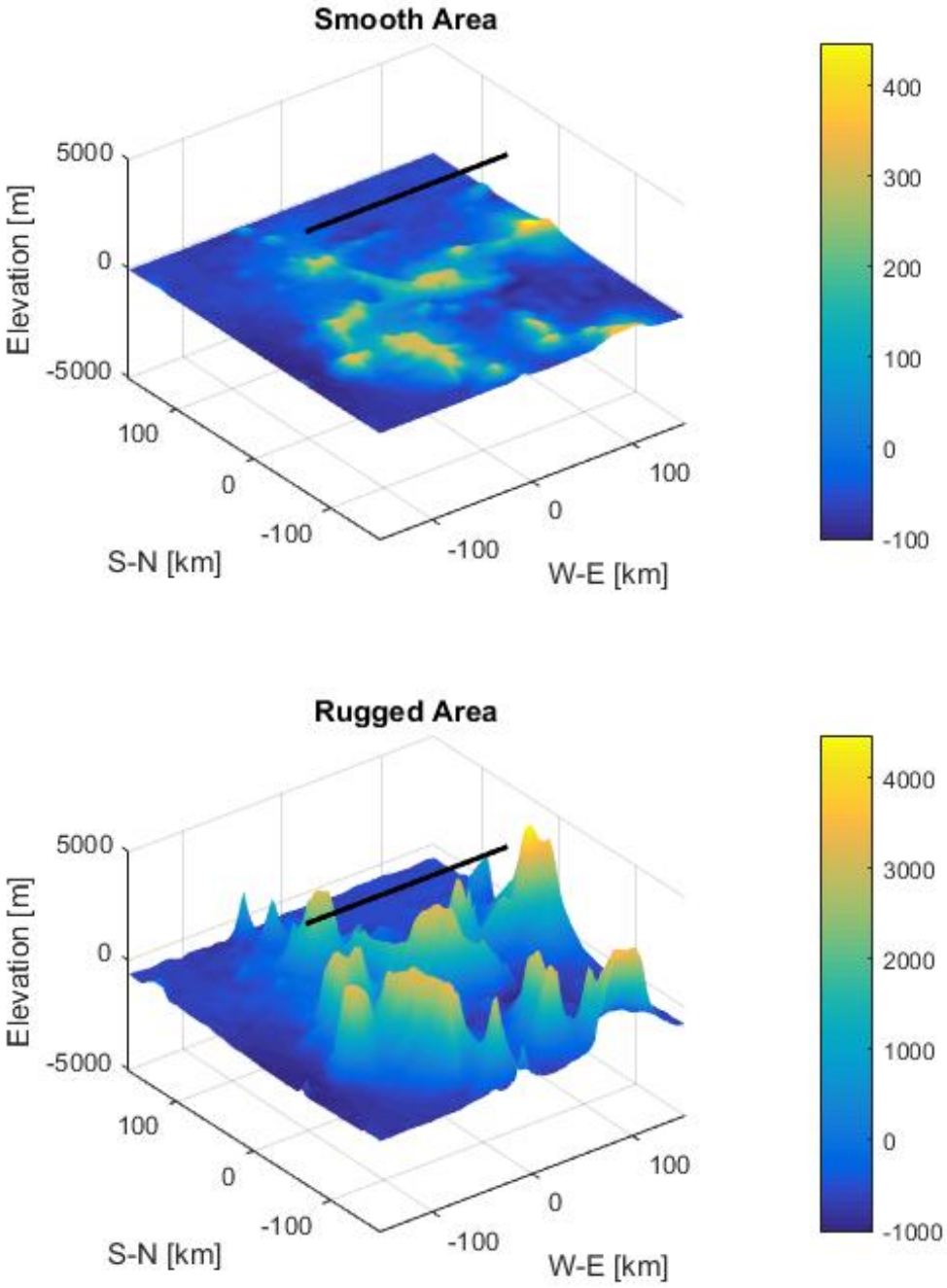

Figure 3.1: The simulated digital elevation models of two areas. The units of the color bars are meter. The black lines are the locations where the gravitational gradients were computed.

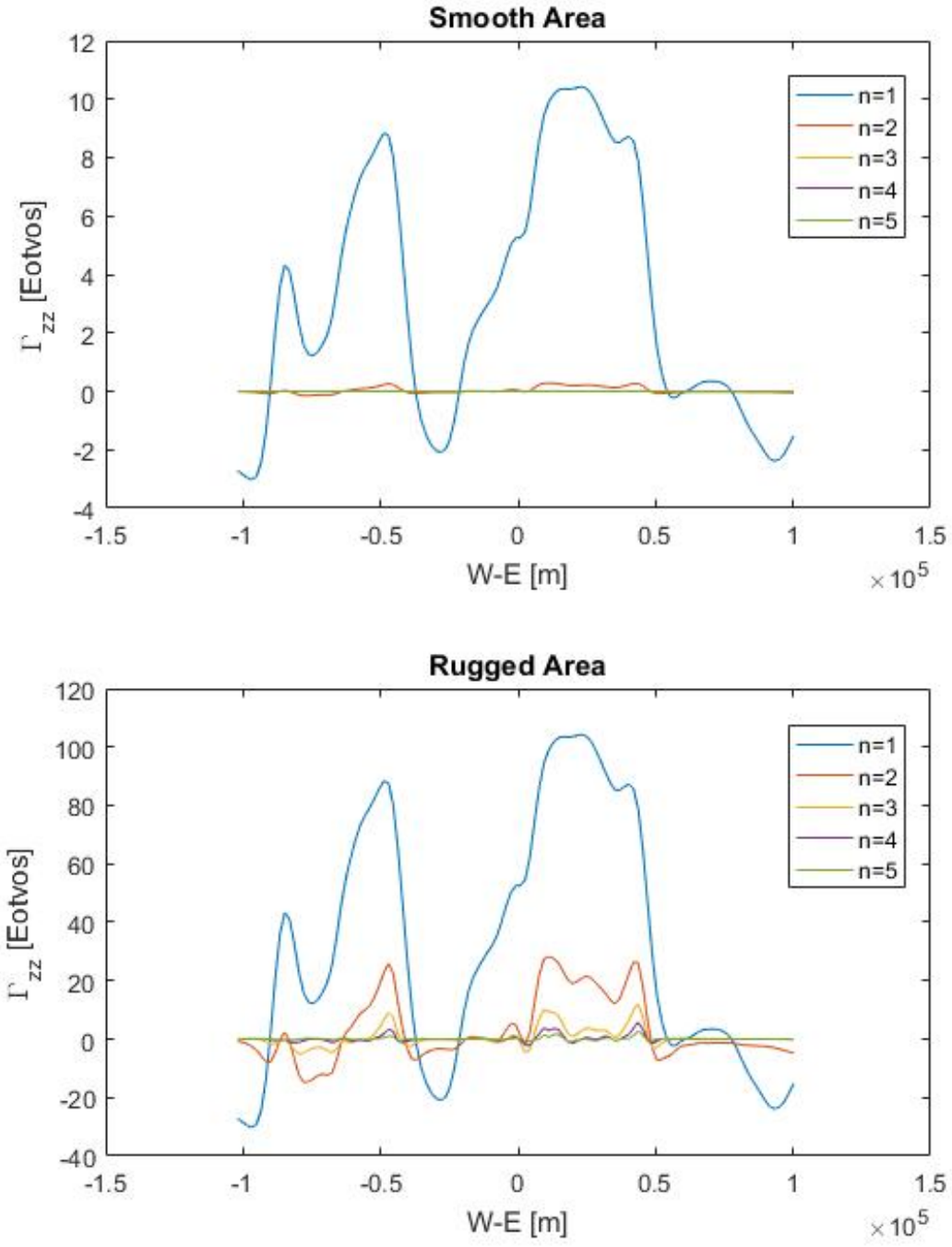

Figure 3.2: The first 5 terms of series (3.4) for the vertical gravitational gradient Γ_{zz} of the two areas.

Similar results were obtained for the other elements of the gravitational gradient tensor. Figure 3.2 clearly shows that in the smooth area, the $n=1$ term of Parker's series is dominant and the nonlinear terms are negligible, whereas in the rugged area the nonlinear terms are not negligible compared to the $n=1$ term. A nonlinear term is artificially defined as "negligible" if its mean value is smaller than 1.5% of the mean of the linear term. In the smooth area the mean of the largest nonlinear term is 1.02% of the mean of the linear term, whereas in the rugged area this number is 10.24%.

The total vertical gravity gradient is computed through formula (3.4), using the first 16 terms for the smooth area and the first 49 terms for the rugged area. Higher order terms are neglected because they are smaller than the computer precision. The largest difference between the total VGG and the linear term is 0.3 Eötvös in the smooth area, whereas it is as large as 48.9 Eötvös in the rugged area. To show the convergence of (3.4), the total gravity gradient is also computed through the right rectangular prisms method using formula (2.51). The detailed algorithm for this forward computation method can be found in section 2.2 or [*Zhu*, 2007]. Figure 3.3 shows that the series (3.4) converges to the gradient computed by the right rectangular prism method in both smooth and rugged areas, because the observation points are on the plane that is above all the topography.

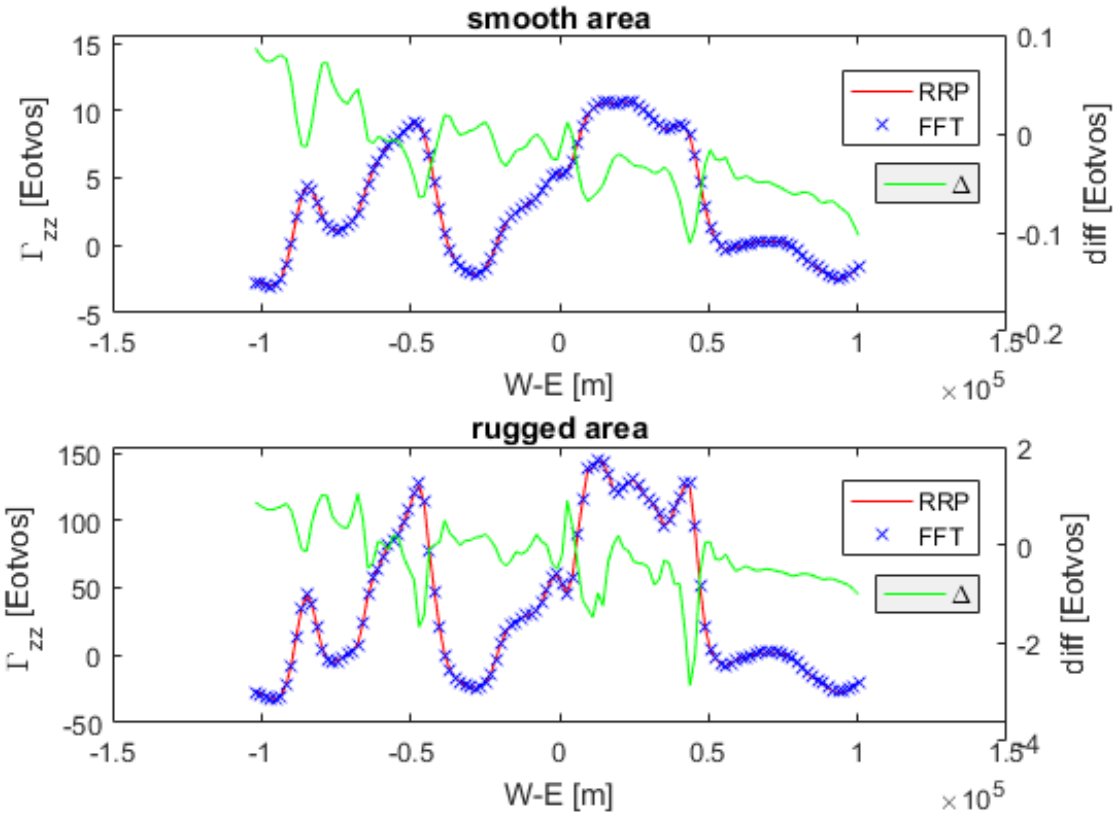

Figure 3.3: The vertical gravity gradients computed from the right rectangular prisms (RRP) method and from formula (3.4) using the fast Fourier transform (FFT). The green line is the difference between the two methods.

For gravity and gravity gradient measurements, usually it is not easy to significantly improve the measurement accuracy. Therefore, it is important to study how to make use of the nonlinear terms before we seek more precise gravity gradient measurements to improve the estimation accuracy, and this requires new algorithms that can handle tens of thousands of parameters in nonlinear models.

There exist several methods to make use of the nonlinear terms, such as iteration, like Newton's method. Another idea is to rearrange (3.4), which gives

$$\mathcal{F}\left(b(x,y)\right)+\pi\bar{f}\,\mathcal{F}\left(b^2\right)+\cdots+\frac{\left(2\pi\bar{f}\right)^{n-1}}{n!}\mathcal{F}\left(b^n\right)+\cdots=\frac{\mathcal{F}\left(\Gamma_{jk}\right)}{\mu_{jk}\cdot G\left(\rho_c-\rho_w\right)\bar{f}^{-1}e^{-2\pi\bar{f}d}} \quad (3.6)$$

Its right-hand side can be computed from measurements. Its left-hand side contains the only unknown parameter b. If we could find a way to solve this equation, one more method to solve

for the seafloor topography is obtained. The author leaves this discussion open, and in the next section concentrates on the method of simulated annealing, an optimization algorithm that is specifically designed to solve for parameters (seafloor topography) in highly nonlinear models.

3.2.2 Introduction to the Coherency

The analysis of the nonlinear effect in the last subsection relies on numerical computation. In this subsection, an algorithmic approach to analyze the linearity between gravity gradient and topography called coherency is developed.

Assume that the signals (e.g. gravity anomaly Δg , gravity gradient Γ , topography b) are ergodic zero-mean stochastic processes. Let us discuss the one-dimensional signals first. Generalizing signals to higher Cartesian dimensions is straightforward. The *cross-correlation function* for them is:

$$\theta_{\Gamma b}(\tau) = E\left(\Gamma_x b_{x+\tau}\right) = \int_{-\infty}^{\infty}\int_{-\infty}^{\infty} \Gamma_x b_{x+\tau} p_{\Gamma b}\left(\Gamma_x, b_{x+\tau}\right) d\Gamma_x db_{x+\tau} \tag{3.7}$$

where E is the expectation operator, $p_{\Gamma b}$ is the joint probability density function of the two random variables, $\Gamma_u \equiv \Gamma(u)$ and $b_v \equiv b(v)$. The Fourier transform of the cross-correlation function is the cross-Power-Spectral-Density (PSD) of Γ and b. The units of this particular cross-correlation function are $Eötvös \cdot m$, and then the cross-PSD has units $Eötvös \cdot m/(cycle/m)$. If the two signals in (3.7) are the same, one obtains the auto-correlation and auto-PSD:

$$\mathcal{F}\left(\theta_{\Gamma b}\right) \equiv \Theta_{\Gamma b}(f) = \int_{-\infty}^{\infty} \theta_{\Gamma b} e^{-i2\pi f\xi} d\xi \tag{3.8}$$

The *coherency*, also called magnitude squared coherence (MSC), is defined as the normalized cross-PSD so that it is in the interval between zero and unity for all frequencies. The coherency defined by

$$r^2(f) = \frac{\left|\Theta_{\Gamma b}(f)\right|^2}{\Theta_{\Gamma\Gamma}(f)\Theta_{bb}(f)} \tag{3.9}$$

is real-valued where the auto-PSDs $\Theta_{\Gamma\Gamma}(f)$ and $\Theta_{bb}(f)$ are real-valued even functions of f and the cross-PSD $\Theta_{\Gamma b}(f)$ is a complex-valued function of f [*Carter et al.*, 1973; *Bendat and Piersol*, 2010].

The coherency is a frequency-domain analogue of the correlation coefficient. It indicates the linearity between the two data sets in the frequency domain regardless of their amplitude. Equation (2.48) suggests that under a first-term approximation the relationship between topography and gravity gradient can be described through a linear system, in which the topography b is treated as input, and the gravity gradient Γ is treated as output,

$$\Gamma(b) = \mathscr{F}^{-1}(Z_\Gamma) * b, \tag{3.10}$$

where * denotes convolution. This system is linear because it satisfies the additive and homogeneous properties:

$$\Gamma(b_1 + b_2) = \mathscr{F}^{-1}(Z_\Gamma) * b_1 + \mathscr{F}^{-1}(Z_\Gamma) * b_2 \tag{3.11}$$

$$\Gamma(c \cdot b) = c \cdot \mathscr{F}^{-1}(Z_\Gamma) * b \tag{3.12}$$

where c is an arbitrary constant, and b_1, b_2 are two inputs.

In fact, in addition to $\mathscr{F}^{-1}(Z_\Gamma) * b$, Γ when observed may also contain noise w:

$$\Gamma = \mathscr{F}^{-1}(Z_\Gamma) * b + w \tag{3.13}$$

The w and the input b are assumed independent from each other. Let us denote the power spectral density of the topography and noise as Θ_{bb} and Θ_{ww}, respectively. Then the PSD $\Theta_{\Gamma b}$ and $\Theta_{\Gamma\Gamma}$ are:

$$\Theta_{\Gamma b}(f) = Z_\Gamma^* \Theta_{bb}(f) \tag{3.14}$$

$$\Theta_{\Gamma\Gamma}(f) = |Z_\Gamma|^2 \Theta_{bb}(f) + \Theta_{ww}(f) \tag{3.15}$$

where the asterisk in (3.14) denotes the complex conjugate.

The coherency between b and Γ is:

$$
\begin{aligned}
r^2(f) &= \frac{\left|\Theta_{\Gamma b}(f)\right|^2}{\Theta_{\Gamma\Gamma}(f)\Theta_{bb}(f)} \\
&= \frac{\left|Z_\Gamma\right|^2 \Theta_{bb}^2(f)}{\left(\left|Z_\Gamma\right|^2 \Theta_{bb}(f) + \Theta_{ww}(f)\right)\Theta_{bb}(f)} \\
&= \frac{\dfrac{\left|Z_\Gamma\right|^2 \Theta_{bb}(f)}{\Theta_{ww}(f)}}{\left(\dfrac{\left|Z_\Gamma\right|^2 \Theta_{bb}(f)}{\Theta_{ww}(f)} + 1\right)}
\end{aligned}
\tag{3.16}
$$

The ratio of spectral density of $\mathscr{F}^{-1}(Z_\Gamma) * b$ to the spectral density of the noise, $\dfrac{\left|Z_\Gamma\right|^2 \Theta_{bb}(f)}{\Theta_{ww}(f)}$, is treated as the signal-to-noise ratio (SNR). In the ideal case of a single input/single output linear system without noise (where $\Theta_{ww}(f)$ is zero), the coherency should be 1 for all frequencies according to (3.16). If the coherency is greater than zero but less than unity, one possible reason is that the measurement contains noise (i.e., $\Theta_{ww}(f)$ is not zero). In other words, the coherency tells us how much of Γ can be described as a filtered version of b. Except for noise, there are two other causes that can make the coherency deviate from one. Firstly, the topography and gravity gradient are not linearly related as the admittance theory suggests. In fact, Parker's theory says that (2.48) is only approximately true. Secondly, the gravity gradient may be generated due to the topography as well as to other inputs, e.g. the underground density anomaly. Coherency close to one means Γ is generated mostly as the convolution of b and a filter function. Coherency close to zero means that the gravity gradient Γ and the topography b are independent.

In summary, at wavelength bands where the coherency between the gravity gradient and the topography is large, we could use the admittance to estimate the topography since the relation between them is well represented by a linear system. At wavelength bands where the coherency is small, we cannot estimate the topography from gravity gradients using a linear system due to noises, significant nonlinear terms, and/or other sources that falsify the relationship described in (2.48).

3.2.3 Coherency for finite power signals

The PSD in (3.9) is computed as follows. Equations (3.7) and (3.8) provide one way to compute the coherency: taking Fourier transform of the estimated correlation function. This is called the correlogram method. The second method is based on the relationship between PSD and the Fourier transforms of the original data records. This is called the periodogram method and will be discussed in the following.

The realization of the stationary random process cannot be a finite-energy signal since the stationary data theoretically persist forever. We assume that it is a finite-power signal. In practice both topography and gravity gradient data are available only in the finite interval T. The truncated data $\Gamma_T(x)$ and $b_T(x)$ are square-integrable and thus both have a Fourier transform $\breve{\Gamma}_T(f)$ and $\breve{b}_T(f)$, respectively:

$$\begin{aligned}\breve{\Gamma}_T(f) &= \int_0^T \Gamma_T(x) e^{-i2\pi fx} dx \\ \breve{b}_T(f) &= \int_0^T b_T(x) e^{-i2\pi fx} dx\end{aligned} \tag{3.17}$$

If the data are discrete, we identify them by adding a subscript to the spatial variable: $x_0, x_1, \cdots, x_{N-1}$, where N is the total number of the data, Δx is the constant sampling interval, and $T = N\Delta x$. Then the discrete Fourier transforms of the data are:

$$\begin{aligned}\breve{\Gamma}(f_k) &= \Delta x \sum_{l=0}^{N-1} \Gamma_T(x_l) e^{-i\frac{2\pi}{N}kl} \\ \breve{b}(f_k) &= \Delta x \sum_{l=0}^{N-1} b_T(x_l) e^{-i\frac{2\pi}{N}kl}\end{aligned} \tag{3.18}$$

where $f_k = \dfrac{k}{N\Delta x}$, $-\dfrac{N}{2} \le k \le \dfrac{N}{2} - 1$ if k is even, $-\dfrac{N-1}{2} \le k \le \dfrac{N-1}{2}$ if k is odd.

The Fourier transform of the correlation function can be shown to be related to the signals by (3.19) [*Bendat and Piersol*, 2010]:

$$\Theta_{\Gamma b}(f) = \lim_{T\to\infty}\left(E\left(\frac{1}{T} \breve{\Gamma}_T^*(f) \breve{b}_T(f) \right) \right) \tag{3.19}$$

where E is the expectation operator and the asterisk denotes the complex conjugate.

Omitting the limit and expectation gives a simple way to estimate the PSD:

$$\hat{\Theta}_{\Gamma b}(f) = \frac{1}{T}\breve{\Gamma}_T^*(f)\breve{b}_T(f) \tag{3.20}$$

This estimator is not a consistent estimator and generally biased. In addition, the standard deviation of the estimate $\hat{\Theta}_{\Gamma b}(f)$ is as large as the true value, which is unacceptable in most cases (see subsection 6.5.5 in [*Bendat and Piersol*, 1971]). What's more, this estimate would cause failure when computing the coherency:

$$\begin{aligned}\hat{r}^2(f) &= \frac{\left|\hat{\Theta}_{\Gamma b}(f)\right|^2}{\hat{\Theta}_{\Gamma\Gamma}(f)\hat{\Theta}_{bb}(f)} \\ &= \frac{\left|\frac{1}{T}\breve{\Gamma}_T^*(f)\breve{b}_T(f)\right|^2}{\frac{1}{T}\breve{\Gamma}_T^*(f)\breve{\Gamma}_T(f)\frac{1}{T}\breve{b}_T^*(f)\breve{b}_T(f)} \\ &\equiv 1\end{aligned} \tag{3.21}$$

Equation (3.21) shows that the coherency calculated using (3.20) always gives unity, even if the two signals are totally incoherent. So, in practice, the PSD estimated by (3.20) should be smoothed. In this procedure the smoothing operation approximates and replaces the expectation operator in (3.19). It is usually done in one of the following two ways. The first way is to compute individual estimates from several independent sample records or several overlapping segments split from one sample record, and then these estimates are averaged at each frequency. The second way is to average the adjacent spectral components in the estimate from a single sample record. A generalization of the second method is to average the estimates computed from one sample record windowed with different orthogonal tapers.

Nowadays Welch's averaged, modified periodogram method [*Welch*, 1967] is a common way to estimate the PSD. But this method is inappropriate for short signals since it splits the signal into segments. As a result the long wavelengths are not kept since the longest resolvable wavelength equals the length of the data. In the appendix A, the Thomson's [1982] Multiple-Slepian-Taper method is introduced, which does not segment signals.

3.2.4 Radially Symmetric Coherency

The formula (2.48) suggests that the gravity gradient Γ_{zz} and topography are related through a radially symmetric operator, so their 2-D periodograms are azimuthally averaged to obtain the *radially symmetric coherency*, which is a function of radial frequency [*Marks and Smith*, 2012].

Firstly, the discrete Fourier transform of the vertical gravity gradient and topography grids were computed. Next, the periodograms for the auto- and cross-PSD were calculated. Then the radial frequency was evenly divided into several frequency bands. Next, the elements of the periodogram whose radial frequencies fall into the same band were averaged, and treated as the PSD at the frequency band center. Finally, the radially symmetric coherency was computed by normalizing the azimuthally averaged cross-PSD,

$$r^2\left(\bar{f}\right)=\frac{\left|\left\langle\left(\mathcal{F}\left(\Gamma_{zz}\right)\right)^{*}\mathcal{F}\left(b\right)\right\rangle\right|^2}{\left\langle\left(\mathcal{F}\left(\Gamma_{zz}\right)\right)^{*}\mathcal{F}\left(\Gamma_{zz}\right)\right\rangle\left\langle\left(\mathcal{F}\left(b\right)\right)^{*}\mathcal{F}\left(b\right)\right\rangle} \tag{3.22}$$

where $\langle\ \rangle$ is the average operator.

The radially symmetric coherency between topography and vertical gravity gradient for the smooth and the rugged areas, shown in Figure 3.1, were computed using (3.22). The synthetic vertical gravity gradients (with no random error) were calculated through the theoretical formula (3.4) from topography data.

In smooth area where topography and vertical gravity gradient are almost linearly related (see upper panel of Figure 3.2), the coherency is large at all frequencies. In the rugged area where the nonlinearity is significant (see lower panel of Figure 3.2), the coherency is large only at low frequencies. As frequency increases from 2e-5 to 2e-4 cy/m, the coherency quickly decreases from 0.95 to 0.5. At wavelengths shorter than 5 km, more than half of the vertical gravity gradient is from the nonlinear terms of Parker's infinite series. In other words, if the topography is estimated through the linear approximation based FFT method as described in section 3.1, the short wavelengths cannot be improved no matter how accurate the vertical gravity gradient measurements are.

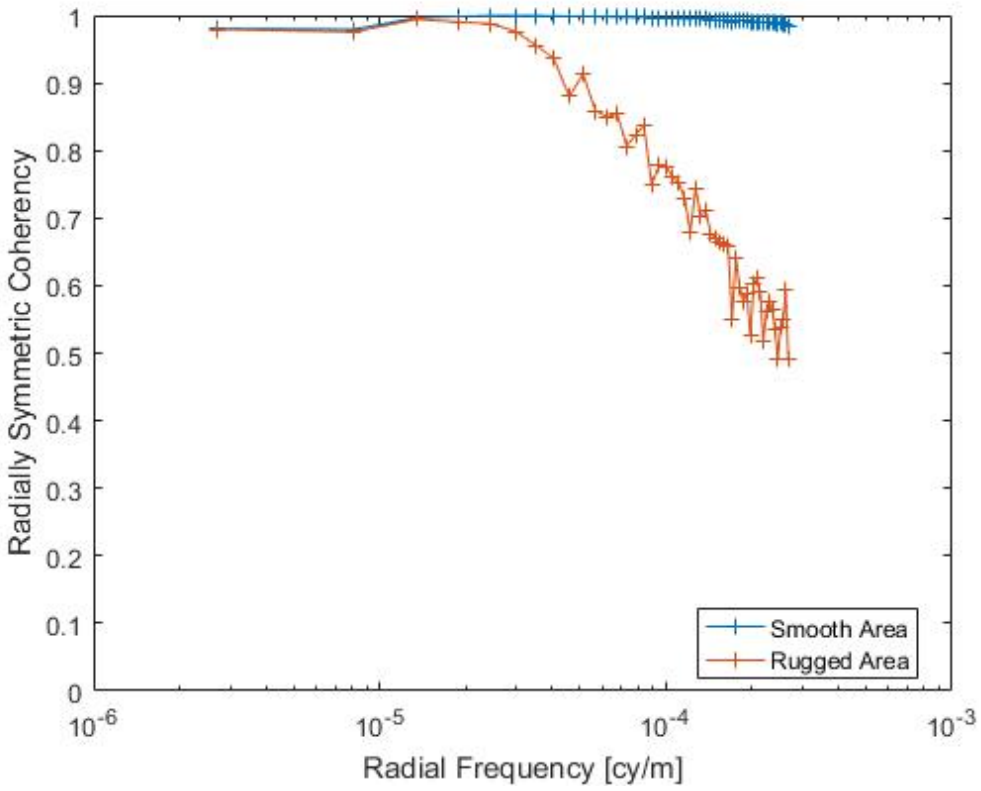

Figure 3.4: Radially symmetric coherencies for the smooth and the rugged areas. The topographies were synthesized data, and the simulated vertical gravity gradients were computed from the synthesized topographies using Parker's infinite series.

3.2.5 Coherency for Signals on the Sphere

The coherency analysis for the local data above is conducted in flat-Earth approximation. Instead of concentrating on a small area where one has depth and gradient data, it would be beneficial to look at the coherency between gradients and topography in general, using global models like EGM2008. The coherency analysis for the global gravity and topography data should be conducted in spherical approximation. That is, the Fourier-Legendre transform rather than the Fourier transform is used to estimate the PSD.

The Legendre transform pair is defined as:

$$g(\theta,\lambda)=\sum_{n=0}^{\infty}\sum_{m=0}^{n}\left(\overline{C}^{g}_{n,m}\cos m\lambda+\overline{S}^{g}_{n,m}\sin m\lambda\right)\overline{P}_{n,m}(\cos\theta) \qquad (3.23)$$

$$\bar{C}^{g}_{n,m} = \frac{1}{4\pi}\int_{\theta=0}^{\pi}\int_{\lambda=0}^{2\pi} g(\theta,\lambda)\,\bar{P}_{n,m}(\cos\theta)\cos m\lambda \sin\theta d\theta d\lambda$$
$$\bar{S}^{g}_{n,m} = \frac{1}{4\pi}\int_{\theta=0}^{\pi}\int_{\lambda=0}^{2\pi} g(\theta,\lambda)\,\bar{P}_{n,m}(\cos\theta)\sin m\lambda \sin\theta d\theta d\lambda \qquad (3.24)$$

where θ is co-latitude, λ is longitude, $\bar{C}^{g}_{n,m}$ and $\bar{S}^{g}_{n,m}$ are called the Legendre transform of g, and $\bar{P}_{n,m}(\cos\theta)$ is the fully normalized, associated Legendre function of the first kind of degree n and order m, with $0 \le m \le n$ and $n \ge 0$. The definition of the associated Legendre function can be found in [*Hofmann-Wellenhof and Moritz*, 2005].

If assumed isotropic, the correlation function for signals on the sphere is given by (3.25) [*Jekeli*, 2010]:

$$\phi_{gb}(\psi) = \frac{1}{8\pi^2}\int_{0}^{2\pi}\iint_{\sigma} g(\theta,\lambda)\,b(\theta',\lambda')\sin\theta d\theta d\lambda d\alpha \qquad (3.25)$$

where ψ is the spherical distance between (θ,λ) and (θ',λ'), α is the azimuth of (θ',λ') at (θ,λ).

Applying the direct Legendre transform to (3.25), we obtain the spectrum of the correlation function, $(\Theta_{gb})_n$. It is also called the cross-PSD of g and b on the sphere or degree-and-order variance, and can be computed in terms of $\bar{C}^{g}_{n,m}$, $\bar{S}^{g}_{n,m}$, $\bar{C}^{b}_{n,m}$, and $\bar{S}^{b}_{n,m}$, the Legendre transforms of the functions being correlated.

$$(\Theta_{gb})_n = \frac{1}{2n+1}\sum_{m=0}^{n}\left(\bar{C}^{g}_{n,m}\bar{C}^{b}_{n,m} + \bar{S}^{g}_{n,m}\bar{S}^{b}_{n,m}\right) \qquad (3.26)$$

The Legendre transform of the gravity anomaly can be obtained from the EGM2008 model and one reference ellipsoid (see Appendix B). The Legendre transform of topography can be obtained from the spherical harmonics of topography.

The topography in spherical harmonics is:

$$b(\theta,\lambda) = \sum_{n=0}^{N\max}\sum_{m=0}^{n}\left(\bar{C}^{b}_{n,m}\cos m\lambda + \bar{S}^{b}_{n,m}\sin m\lambda\right)\bar{P}_{n,m}(\cos\theta) \qquad (3.27)$$

where the $\overline{C}^{b}_{n,m}$ and $\overline{S}^{b}_{n,m}$ are the spherical harmonic coefficients.

Substituting (B.6) and (3.27) into (3.26), we have

$$\left(\Theta_{gb}\right)_n = \frac{GM}{\left(2n+1\right)r}\sum_{m=0}^{n}\left(\frac{a}{r}\right)^n\left(\overline{C}^{\Delta g}_{n,m}\overline{C}^{b}_{n,m} + \overline{S}^{\Delta g}_{n,m}\overline{S}^{b}_{n,m}\right) \tag{3.28}$$

For the auto-PSD, we have

$$\left(\Theta_{gg}\right)_n = \frac{GM^2}{\left(2n+1\right)r^2}\sum_{m=0}^{n}\left(\frac{a}{r}\right)^{2n}\left(\overline{C}^{\Delta g}_{n,m}\overline{C}^{\Delta g}_{n,m} + \overline{S}^{\Delta g}_{n,m}\overline{S}^{\Delta g}_{n,m}\right) \tag{3.29}$$

$$\left(\Theta_{bb}\right)_n = \frac{1}{\left(2n+1\right)}\sum_{m=0}^{n}\left(\overline{C}^{b}_{n,m}\overline{C}^{b}_{n,m} + \overline{S}^{b}_{n,m}\overline{S}^{b}_{n,m}\right) \tag{3.30}$$

Analogous to (3.9), the coherency is defined as:

$$r_n^2 = \frac{\left|\left(\Theta_{gb}\right)_n\right|^2}{\left(\Theta_{gg}\right)_n\left(\Theta_{bb}\right)_n} \tag{3.31}$$

The spatial resolution corresponding to n is computed using the formula (3.32) [*Barthelmes*, 2009]:

$$\psi = 4 * \arcsin(\frac{1}{n+1}) \tag{3.32}$$

where ψ is the spherical distance.

The auto- and cross-PSDs of the global gravity anomaly and global topography were computed using the EGM2008 tide-free model, DTM2006.0 [*Pavlis et al.*, 2012], and EARTH2012 [*Hirt and Kuhn*, 2012]. The former model is for gravity and the latter two are for topography. In the computation, the GM and a associated with EGM2008 were adopted for the three models above, and the r was set to a. The WGS84 was chosen to compute the spherical harmonics for the normal gravitational potential.

Results from the two global topography models are similar. Figure 3.8 displays the coherency between the topography and gravity anomaly over the globe. Because the Legendre transform is computed using global data and we are not able to tell the "location" of a Legendre transform, the Figure 3.8 can be interpreted as a kind of globally averaged coherency, which provides information about the general relation between topography and gravity field over the globe. Between the degree 130 and 930 the coherency is larger than 0.5. According to equation (3.32), this band is about [24.4 km, 194.5 km]. Within this wavelength band, the assumption of the

linear relationship between gravity and topography is a good one, and the estimation algorithm in section 3.1 is eligible. This band is close to the 15-160 km band chosen in [*Smith and Sandwell*, 1994], which predicts seafloor topography only over the southern oceans. At longer wavelengths, the coherency is low because isostatic compensation cancels most of the gravity anomaly. At shorter wavelengths, the coherency is low due to both the nonlinear effects of rugged topography on gravity and the underground density anomaly. At these wavelengths the performance of the estimation algorithm in section 3.1 is poor. Because the EGM2008 model is developed based on 5′×5′ free-air gravity anomaly data, Figure 3.8 does not provide information about coherency for wavelengths shorter than 10 km. The analysis in this subsection is not specific to gravity anomaly or gravity gradients. It holds for any vertical derivative of the gravity potential.

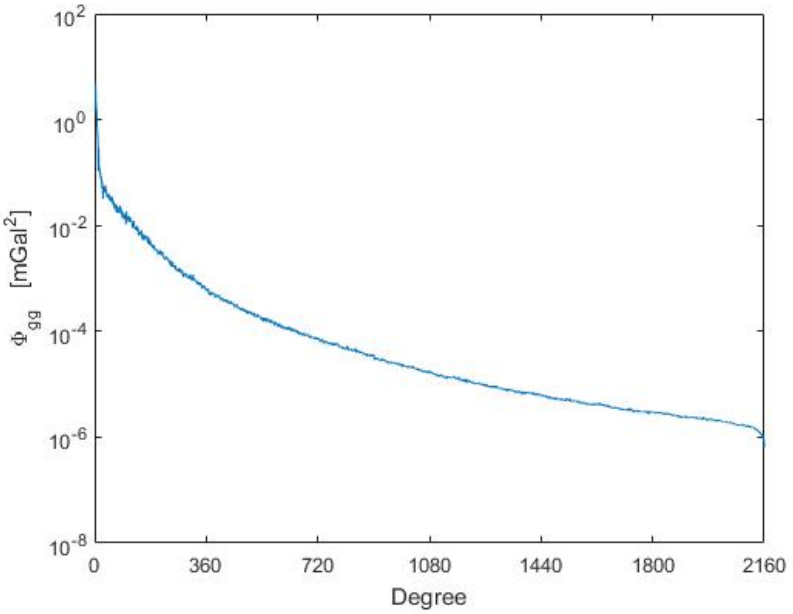

Figure 3.5: The Degree-and-order variance of the gravity anomaly computed by EGM2008.

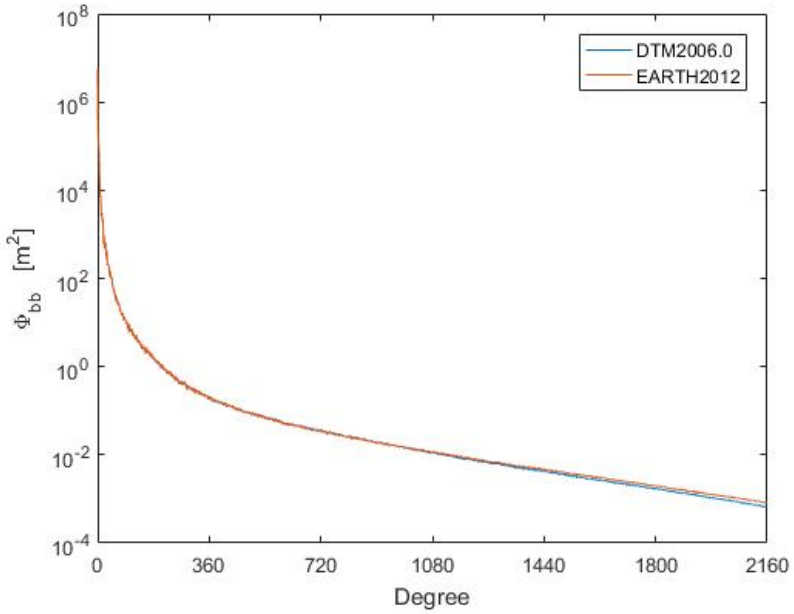

Figure 3.6: The Degree-and-order variance of the DTM2006.0 and EARTH2012 global topography models.

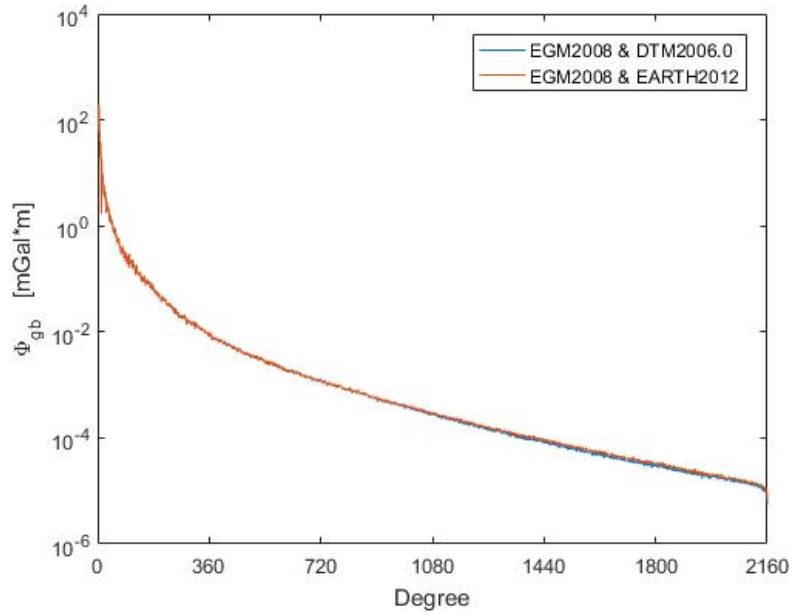

Figure 3.7: The cross-PSD between EGM2008 gravity anomaly and each of the two global topography models.

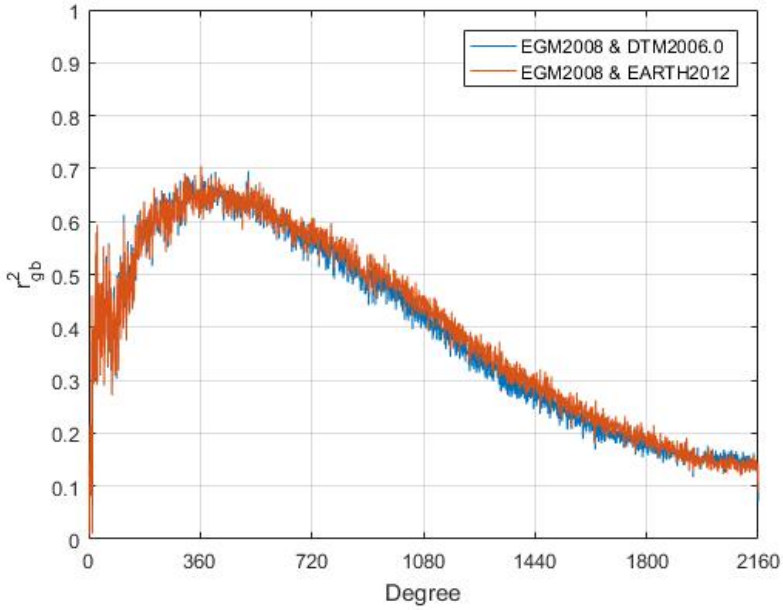

Figure 3.8: The coherency between EGM2008 gravity anomaly and each of the two global topography models.

3.3 Seafloor Topography Estimation Using Simulated Annealing

3.3.1 Introduction to the Simulated Annealing

As shown in Figure 3.2 and Figure 3.4, the nonlinear effect is nonnegligible in rugged areas like the one shown in Figure 4.2. Simulated annealing (SA) is a candidate for a global optimization technique that can process nonlinear inverse problems. The vector containing the parameters to be determined is called the state of the system. The SA algorithm asymptotically finds an optimal state vector with probability 1, for which its cost function, a quality indicator that measures the discrepancy between the observations and the corresponding computed forward model, is at a global minimum [*Kirkpatrick et al.*, 1983; *Laarhoven and Aarts*, 1987]. In this section the SA method to estimate the seafloor topography is developed, for the purpose of improving the accuracy by employing a direct nonlinear model that relates topography and the gravity field.

The invention of SA is generally credited to Metropolis and his coworkers, who established an algorithm to simulate the process of annealing in thermal dynamics [*Metropolis et al.*, 1953]. Thirty years later, *Kirkpatrick et al.* [1983] found the connection between statistical mechanics and multivariate optimization, and developed an algorithm called “simulated annealing” to

minimize the cost function of a multivariate optimization problem by applying the Metropolis criterion. The simulated annealing algorithm was also independently developed by other scientists [*Černý*, 1985] during the same period. Since then, an increasing number of papers have been published for the refinement of the SA algorithm and its applications [*Laarhoven and Aarts*, 1987; *Szu and Hartley*, 1987; *Ingber*, 1989].

The SA algorithm starts with an arbitrary initial state $\mathbf{b}_0$ whose cost function is $E(\mathbf{b}_0)$. Then a new state is generated with the probability $a(\mathbf{b}_k)$ controlled by a parameter called "temperature", where k is the iteration step number. In the initial algorithm [*Kirkpatrick et al.*, 1983], the new state is generated through $b_k^i = b_{k-1}^i + y^i \cdot (B^i - A^i)$, $i \in \{1,2,\cdots D\}$ subject to $A^i \le b_k^i \le B^i$, where D is the number of elements in the state vector, y^i is a random number generated from a uniform distribution in the interval [-1,1], and $[A^i, B^i]$ is the allowed range of b^i [*Uzun*, 2013]. The next step is to compute the cost function of the new state $E(\mathbf{b}_k)$, and then use the Metropolis criterion to determine whether to accept the new state or not. That is, if $\Delta E = E(\mathbf{b}_k) - E(\mathbf{b}_{k-1}) \le 0$, the new state is accepted; and, if $\Delta E > 0$, the new state is accepted with the probability $1/(1+\exp(\Delta E / T_k))$. Next, the temperature is decreased according to a cooling schedule, and a new state is generated to start another iteration cycle. This process is iterated until there is no change in the cost function. It has been verified (see pp. 27-38 in [*Laarhoven and Aarts*, 1987]) that if the cooling schedule is not faster than

$$T_k = \frac{T_0}{\ln k} \tag{3.33}$$

the probability distribution of the state $a(\mathbf{b}_k)$ is given by the Boltzmann distribution

$$\lim_{T\to 0^+}\lim_{k\to\infty} a(\mathbf{b}_k) = \lim_{T\to 0^+}\lim_{k\to\infty} \Pr(\mathbf{b}=\mathbf{b}_k) = \frac{\exp\left\{-\left[E(\mathbf{b}_k) - E_{\min}\right]/T_k\right\}}{\sum_{\mathbf{b}} \exp\left\{-\left[E(\mathbf{b}) - E_{\min}\right]/T_k\right\}} \tag{3.34}$$

Note that the initial temperature T_0 is set sufficiently high so that almost every state transition is accepted at the beginning. As the temperature decreases, the probability to reject the transitions

that increases the cost function gradually approaches one. That is why the simulated annealing can jump out of a local minimum of the cost function at the beginning, and ultimately land on the global minimum cost.

As the temperature decreases, the Boltzmann distribution concentrates on the states with lowest cost, in other words, the state asymptotically converges to an optimal value with probability 1,

$$\lim_{T\to 0^+}\lim_{k\to\infty}\Pr\left\{\mathbf{b}_k \in \mathscr{R}_{optimal}\right\} = 1 \tag{3.35}$$

where $\mathscr{R}_{optimal}$ is the set of global minimal states.

Ingber [1989] improved the SA algorithm and named his new algorithm the adaptive simulated annealing (ASA), which is also known as the very fast simulated annealing. In his algorithm, each element of the state vector is assigned a temperature, so that different elements can be assigned different cooling schedules. The new state is generated through

$$b_k^i = b_{k-1}^i + y^i \cdot \left(B^i - A^i\right),\ i \in \left\{1,2,\cdots D\right\} \tag{3.36}$$

$$y^i = \operatorname{sgn}\left(u^i - \frac{1}{2}\right) T_k^i \left[\left(1+\frac{1}{T_k^i}\right)^{\left|2u^i-1\right|} - 1\right] \tag{3.37}$$

where u^i is generated from a uniform distribution

$$u^i \sim U\left[-1,1\right] \tag{3.38}$$

As a consequence, the temperature is allowed to decrease no faster than

$$T_k^i = T_0^i \exp\left(-c^i k^{\frac{1}{D}}\right) \tag{3.39}$$

where $c^i = m^i \exp\left(-n^i / D\right)$, and m^i, n^i are "free" parameters to help tune the adaptive simulated annealing, so that at the e^n-th iteration the temperature becomes $T_0 \cdot e^{-m}$. This cooling schedule is much faster than $T_k = \dfrac{T_0}{\ln k}$ used in the initial simulated annealing algorithm.

It can be seen from equation (3.39) that, if the parameter dimension D is large, the increase of $k^{\frac{1}{D}}$ becomes exponentially slow, which will slow the speed of temperature decrease and require

prohibitively large computation resources. The adaptive simulated annealing turns to the next best choice by adding a quenching parameter Q

$$T_k^i = T_0^i \exp\left(-c^i k^{\frac{Q}{D}} \right) \tag{3.40}$$

$$c^i = m^i \exp^{-\frac{n^i Q}{D}} \tag{3.41}$$

The quenching parameter is of the same order as D and makes the simulated annealing lose its property of statistical convergence to the global minimum, although in practice it might still be among the best algorithms for a given system [*Ingber and Rosen*, 1992]. Indeed, it has been successfully applied to a number of complex problems with large dimension [*Harri and Kimmo*, 1990; *Griff*, 1991; *Roy et al.*, 2005; *Liu et al.*, 2008; *Li and Ma*, 2014].

The state transition may be best described by a Markov chain. A Markov chain is a discrete state-space stochastic process where the subsequent state only depends on the current state, and not on the previous states [*Uzun*, 2013]. A Markov chain is called homogeneous if, $\Pr\left\{ \mathbf{b}_k = \Xi_j \,|\, \mathbf{b}_{k-1} = \Xi_i \right\}$, the probability of moving from one state Ξ_i to another state Ξ_j, is independent of the index k.

The adaptive simulated annealing method [*Ingber*, 1989; 1993; 1996] is adopted. It is described by a single inhomogeneous Markov chain, and thus is an inhomogeneous algorithm. This is because the temperature T is decreased between every state transition, so the probability density function of y^i in (3.36) depends on the index k. A pseudo-code for the adaptive simulated annealing is given in the Appendix C.

3.3.2 Seafloor Topography Estimation from Gravity Gradients

The seafloor topography parameters in a forward model can be estimated through simulated annealing by minimizing the difference between the observed and forward-computed gravity gradients. Compared to the standard frequency-domain method, SA only needs forward computation formulas, so that the linearization of Parker's infinite series for the convenience of inversion can be avoided and nonlinear topographic effects can be included. SA also has no restrictions on data distribution, as required in Parker's infinite series model, thus enabling more flexibility in airborne gravity gradient trajectories.

The practical implementation of the simulated annealing technique for seafloor topography estimation is described in the following. A local Cartesian coordinate system is set up with the

origin located at the center of a study area and on the surface of the reference ellipsoid, and with X, Y and Z axes pointing to east, north, and up respectively. Then the seafloor of the study area is modeled as a set of adjacent right rectangular prisms with edges parallel to the coordinate axes. The X and Y coordinates of the right rectangular prisms are known. The Z coordinate of the lower faces is the mean depth of the study area. The Z coordinates of the upper faces represent the seafloor heights. They are the unknown parameters and are part of the state vector for simulated annealing.

The vertical gravity gradients at the sea surface, caused by the mass-density of the seafloor topography, are computed using the aforementioned right rectangular prism model. Only the "near zone" effect is considered. That is, for each computation point, only the prisms within a preset distance are included. The vertical gravity gradient is computed at the evaluation point at sea level due to each prism and then summed. The "far zone" effect is of long-wavelength type and approximated by a constant for the entire study area (the validity of this assumption is discussed in the subsection 4.3.1). This parameter (far zone effect) is unknown and added to the state vector **b** to be determined. The density difference between the sea water and seabed is assumed to be constant. In summary, the state vector to be determined contains the seafloor topography parameters and the gravity gradient off-set due to mass outside the near zone. The vertical gravity gradient at each computation point is the sum of vertical gravitation gradients caused by the near zone prisms and the off-set due to the far zone mass, with the density of the prism assumed constant,

$$ {}^{i}\Gamma_{zz}^{comp}\left(\mathbf{b}\right) = \Delta + \sum_{j=1}^{M} {}^{i}\Gamma_{zz}^{comp}\left(b_j\right) \tag{3.42} $$

where ${}^{i}\Gamma_{zz}^{comp}\left(\mathbf{b}\right)$ is the computed vertical gravity gradient at i, $\mathbf{b} = \left\{b_1, b_2, \cdots, b_M, \Delta\right\}$ is the state vector, M is the number of right rectangular prisms within the near zone, and Δ is the vertical gravity gradient due to the far zone mass.

The data used to estimate the topography are vertical gravity gradients derived from satellite altimetry using derivatives of the vertical deflections, and called the "observed" gravity gradients [*Rummel and Haagmans*, 1990; *Sandwell and Smith*, 1997]. There are differences between the computed and observed vertical gravity gradients. The objective is to find the optimal state vector by using the SA that minimizes these differences. The cost function is defined as the average of squared differences between the computed and the observed vertical gravity gradients,

$$ E\left(\mathbf{b}\right) = \frac{1}{N}\sum_{i=1}^{N}\left[{}^{i}\Gamma_{zz}^{obs} - {}^{i}\Gamma_{zz}^{comp}\left(\mathbf{b}\right)\right]^2 \tag{3.43} $$

where N is the number of observation points, ${}^{i}\Gamma_{zz}^{obs}$ is the vertical-vertical gravity gradient observed at i.

Chapter 4: Numerical Experiment

4.1 Study Area Description

The Parker's FFT-based method and the simulated annealing technique developed in the last chapter for seafloor topography estimation were tested in this chapter using data sets for a 2°×2° area.

The study area is located in the West Pacific Ocean. It lies between latitudes 20° and 22° north, and longitudes 156° and 158° east. The 1'×1' vertical gravity gradient model version 24.1 was downloaded from the website of the Scripps Institution of Oceanography (SIO) [*Sandwell et al.*, 2014]. The VGG is calculated using the derivatives of the vertical deflections (refer to Appendix B in [*Sandwell and Smith*, 1997] for details). In [*Sandwell and Smith*, 1997], it is reported that all the along-track data were filtered with the same filter to ensure a common bandwidth (0.5 gain at 18 km wavelength). No such description is found in [*Sandwell et al.*, 2014], which updates the SIO gravity model using the Cryosat-2 and Jason-1 data. The two missions have nominal track spacing of 2.5 km and 7.5 km respectively. The ship sounding depths were downloaded from the National Centers for Environment Information (NCEI). The spatial resolution in 2-D is not uniform due to nonuniform ship tracks. No accuracy information comes with these depths. The ship sounding depths are treated as true values, as analyzed in subsection 2.3.2. This study also uses the global topography model version 18.1 released by the SIO [*Smith and Sandwell*, 1997].

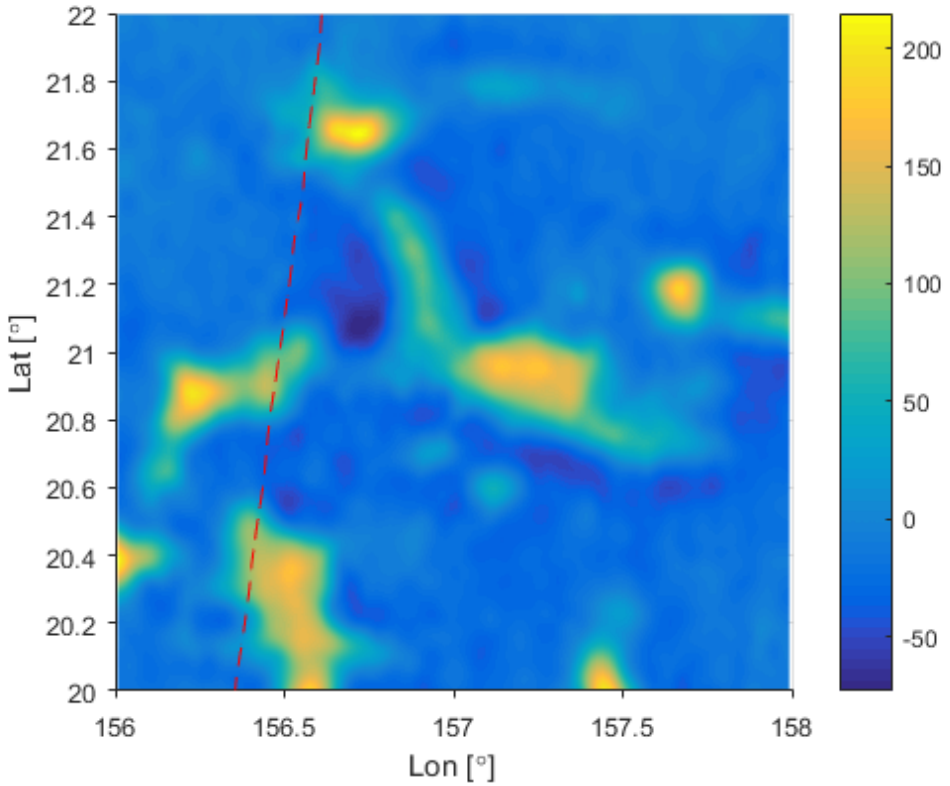

Figure 4.1: The 1′×1′ vertical gravity gradients of the study area. The units of the colorbar are Eötvös. The dashed red line is the ship track of the vessel *JOIDES Resolution*. It was not used in the experiment and was reserved for the accuracy test. All other ship tracks are shown in the upper panel of Figure 4.2.

4.2 Estimation Using Parker's Formulation

4.2.1 Data Preparation

For Parker's method, the bathymetry data that were downloaded from the NCEI cover an extra 0.5° on each side of the research area to reduce the edge effects. Each of the bathymetric depths was assigned to its nearest node of the VGG mesh. For mesh nodes with more than one depth, the weighted average was retained (see the bottom panel of Figure 4.2). The weight assigned to each bathymetric depth is based on its distance from the mesh node using a cosine window, and is given by

$$P = \cos\left(\frac{l}{l_{\max}} \cdot \frac{\pi}{2}\right), \tag{4.1}$$

where P is the weight, l is the distance between the bathymetric depth and the mesh node, and $l_{\max}$ is maximum value that l can achieve, namely $\sqrt{2}$ times the sampling interval.

In the mesh displayed in the bottom panel of Figure 4.2, the mesh nodes constrained by ship sounding were marked for determination of the topography-to-gradient admittance scale. The mesh nodes without constraining data were interpolated through the biharmonic spline interpolation method [*Sandwell*, 1987], see Figure 4.3.

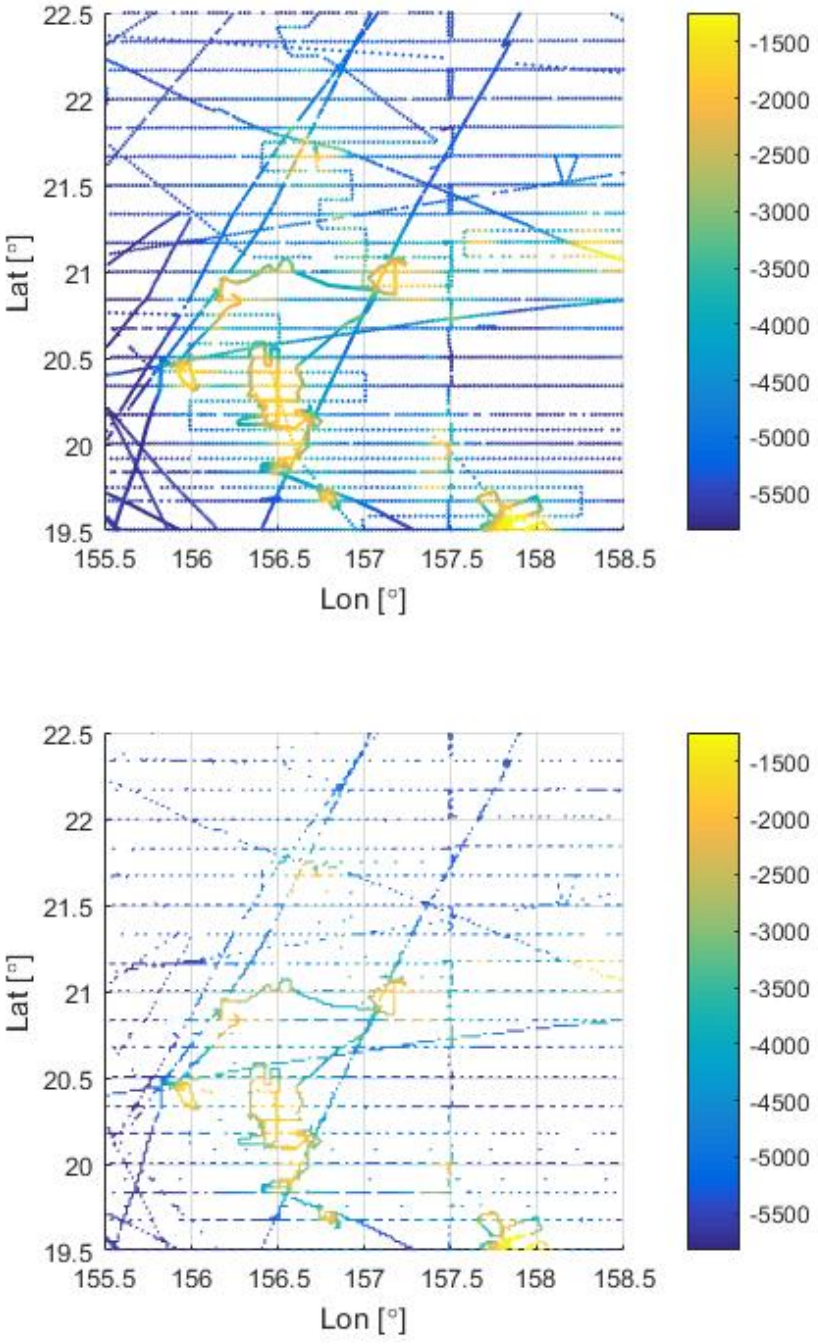

Figure 4.2: (top) Single-beam ship sounding data downloaded from NCEI's website. (bottom) The ship sounding data were assigned to the nearest mesh nodes on the basis of weighted averaging. The units are meter.

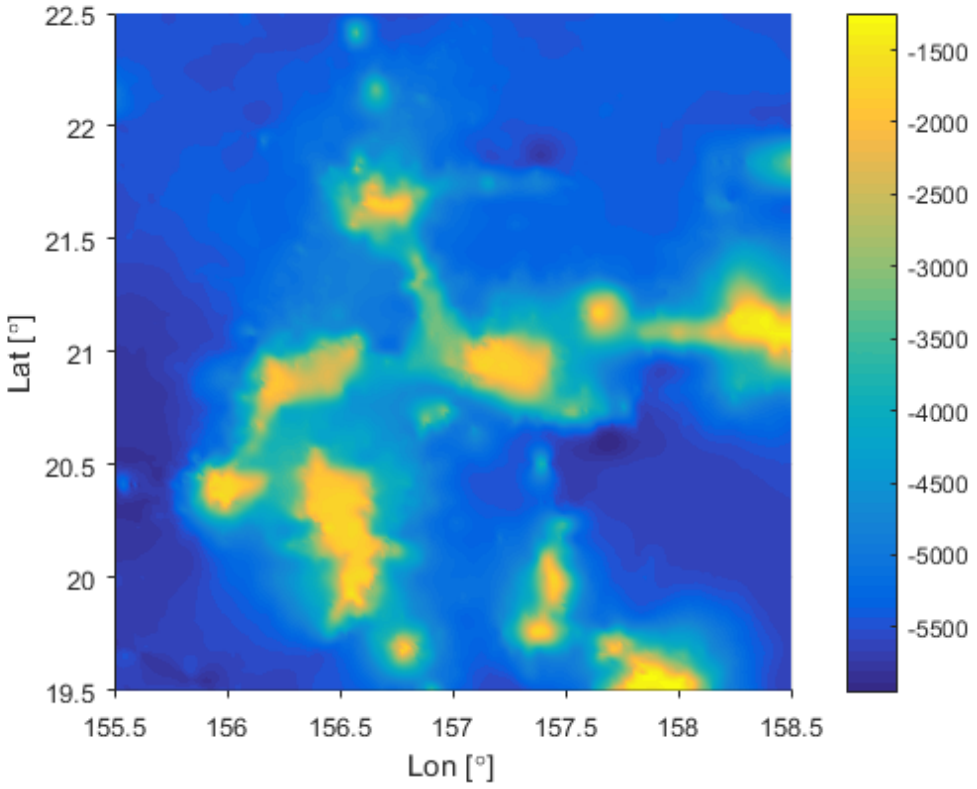

Figure 4.3: The seafloor depths interpolated from the bottom panel of Figure 4.2 through biharmonic spline interpolation. The units are meter.

The mean sea depth, $d = 4828.8$ m, is the average value of the single-beam ship soundings. It relates the seafloor depth and the topography through equation (2.27).

4.2.2 Data Filtering

Parker's theory was developed in the Cartesian coordinate system whereas the data prepared in the last section were given in geodetic coordinates. Therefore, a flat-Earth approximation was used in this section. This approximation is acceptable because its effect is of long-wavelength character, whereas our prediction band is in the short-to-intermediate wavelengths (15-160 km), which are much shorter than the radius of the Earth [*Tapley*, 1997]. Although the data grids are equally spaced along meridians, the distance of the sampling interval along the parallel circle varies with latitude. Nevertheless, since the experiment area is small, in the Fast Fourier Transform the data grids were used as if they were sampled with constant intervals. These

constant intervals are 1729.8 m (mean value of the actual sampling intervals) along west-east direction, and 1729.9 m along south-north direction.

In the uncompensated 15-160 km wavelength band, the seafloor topography was estimated from the gravity gradients. The wavelengths longer than 160 km were obtained by low-pass filtering the ship sounding data. The filters used in this section are Gaussian. The cut-off frequency is defined as the radial frequency where the frequency response of the filter is 0.5.

The low-pass filter (blue line in Figure 4.4)

$$W_l = e^{-2\times\left(2.9983\times10^4\,\pi\bar{f}\right)^2}, \qquad (4.2)$$

was applied to the interpolated ship sounding grid (see Figure 4.3) to obtain the long-wavelength regional seafloor topography $\hat{b}_l$. Note that $W_l = 0.5$ when $\bar{f}^{-1} = 160\,km$.

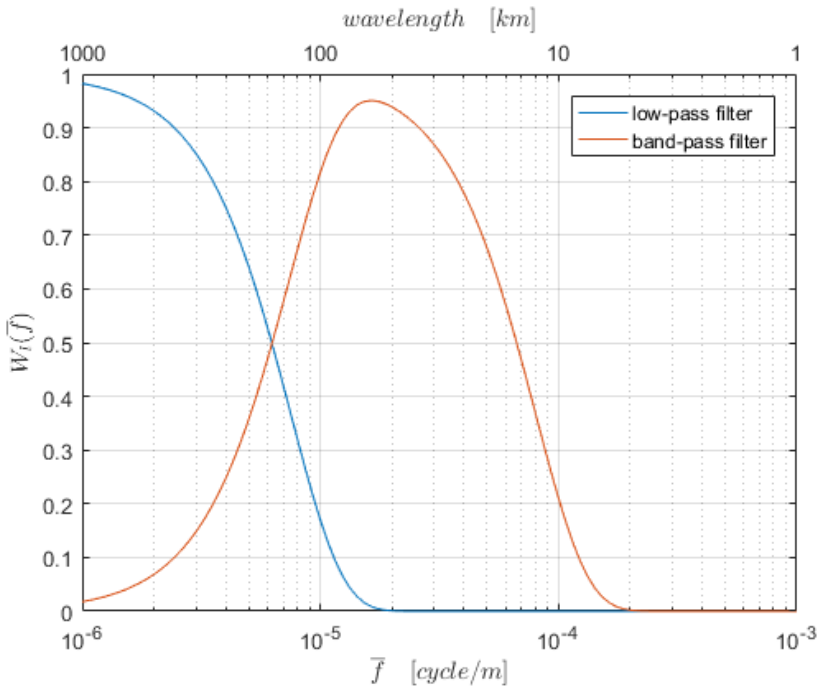

Figure 4.4: The Gaussian low-pass filter (4.2) and the Gaussian band-pass filter (4.3).

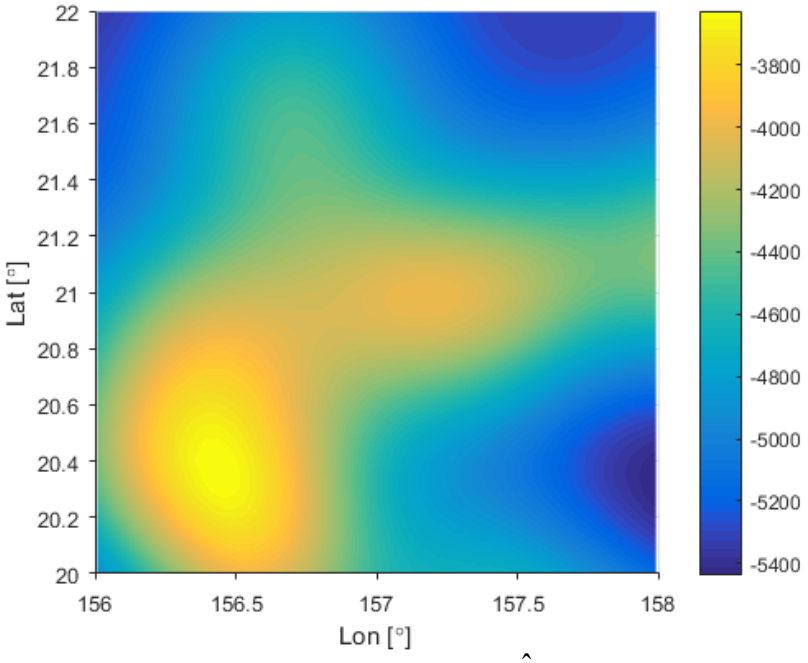

Figure 4.5: The long wavelength regional depths $\hat{b}_l$ computed by low-pass filtering the interpolated ship sounding data. The units are meter.

The band-pass filter (red line in Figure 4.4)

$$W = \left[1 - e^{-2\times\left(2.9983\times10^{4}\pi\bar{f}\right)^{2}}\right] e^{-2\times\left(2.8109\times10^{3}\pi\bar{f}\right)^{2}} \qquad (4.3)$$

was also applied to the interpolated ship sounding (Figure 4.3) to obtain the 15-160 km local wavelengths. The vertical gravity gradient (Figure 4.1) was multiplied by $\left(2\pi\bar{f}\right)^{-1} e^{2\pi\bar{f}d}$ in the frequency domain to obtain the equivalent gravity anomaly, and then was filtered using the same band-pass filter. For this band-pass filter, $W = 0.5$ when $\bar{f}^{-1} = 160\,km$ or $\bar{f}^{-1} = 15\,km$. After the filtering above, we have all the quantities needed by (3.3) for the topography estimation except the topography-to-gradient admittance scale.

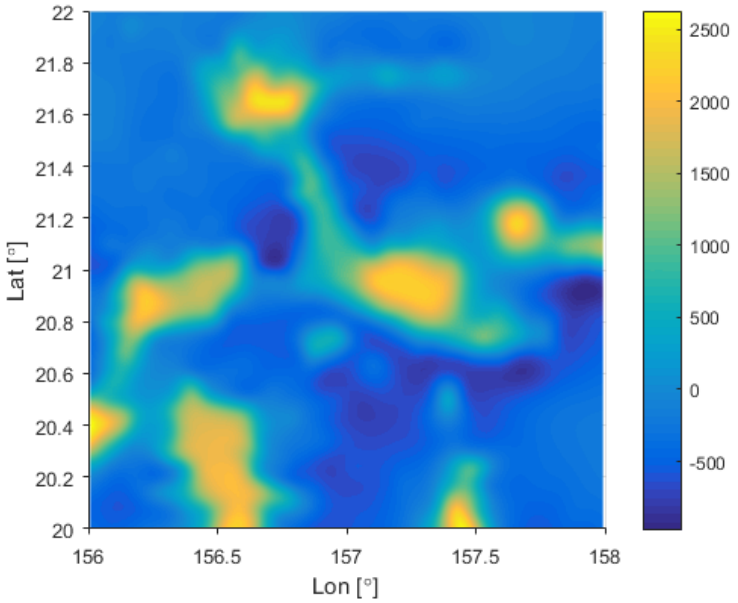

Figure 4.6: The 15-160 km wavelength local seafloor topography obtained by band-pass filtering the interpolated ship sounding (Figure 4.3). Note that only the grid points originally constrained by ship sounding (shown in the bottom panel of Figure 4.2) were used to compute the topography-to-gradient admittance scale. The units are meter.

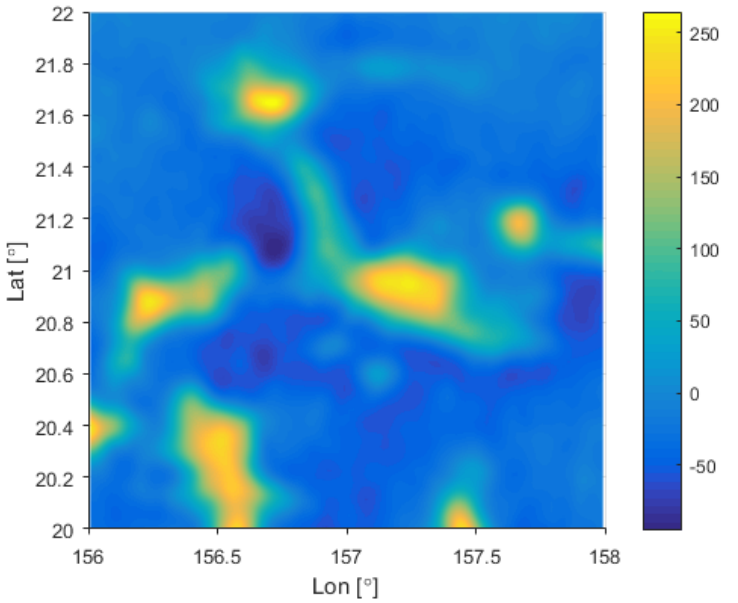

Figure 4.7: The band-pass filtered equivalent gravity anomaly. The units are $mGal$.

4.2.3 Determination of Topography-to-Gradient Admittance Scale

The 15-160 km wavelength local topography and equivalent gravity anomaly (Figure 4.6, Figure 4.7) at places originally constrained by ship soundings (see bottom panel of Figure 4.2) were used to determine the topography-to-gradient admittance scale. The scatter plot of local topography versus equivalent gravity anomaly is shown in Figure 4.8.

Equation (2.50) suggests that the band-pass filtered equivalent gravity anomaly is proportional to the topography in the spatial domain. This is generally true over our study area as Figure 4.8 shows. The correlation coefficient, $\rho_{corrcoef}$, between the local topography and the equivalent gravity anomaly is computed according to

$$\rho_{corrcoef} = \frac{1}{N-1}\sum_{i=1}^{N}\left(\frac{b_i - \mu_b}{\sigma_b}\right)\left(\frac{g_i^e - \mu_{g^e}}{\sigma_{g^e}}\right) \tag{4.4}$$

where N is the number of topography and gravity gradient pairs, μ_b and σ_b are the mean and standard deviation, respectively, of the band-pass filtered topography b_i; and, μ_{g^e} and σ_{g^e} are the mean and standard deviation of the band-pass filtered equivalent gravity anomaly g_i^e. The value of the correlation coefficient is 0.9689.

In some other areas where the ocean bedrock is buried by thick sediments, the local topography and equivalent gravity anomaly may not be linearly related because the observed topography is smooth but the gravity gradient is generated by sub-topography structures.

The scatter plot in Figure 4.8 does not strictly follow a single straight line. When the equivalent gravity anomaly increases, the slope of the scatter plot gradually becomes smaller and could lead to an overestimated topography. As discussed in the last paragraph, sub-seafloor density anomaly may be one cause. Another possible reason is that equation (2.50) is just a first term approximation to Parker's infinite series. This approximation is good only at places where the local topography is small compared with the regional topography.

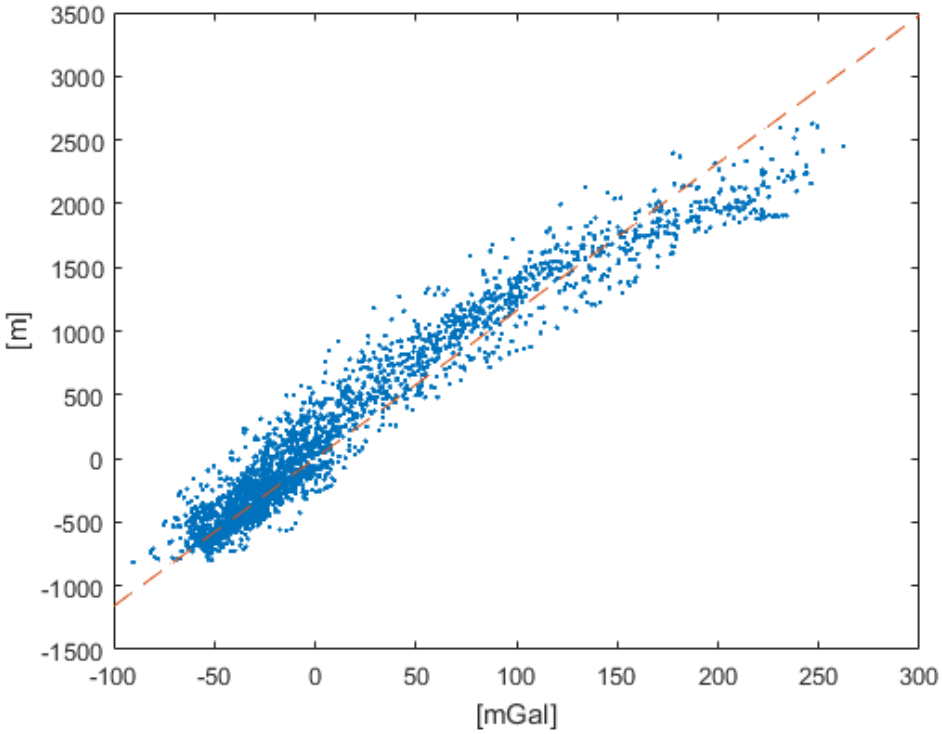

Figure 4.8: Local topography versus local equivalent gravity anomaly at places originally constrained by ship sounding. The red line passes through the coordinate origin. Its slope is topography-to-gradient admittance scale computed through formula (4.5), with standard deviation substituted by median absolute deviation, which is defined by (4.6).

The topography-to-gradient admittance scale S can be found from the slope of the line that best fits the local topography and equivalent gravity anomaly pairs according to the least-squares method. But, because both topography and equivalent gravity anomaly data contain errors, *Smith and Sandwell* [1994] suggest using the standard deviation to calculate the topography-to-gradient admittance scale [*Bendat and Piersol*, 2010]:

$$S = \frac{\sigma_b}{\sigma_g} \tag{4.5}$$

where σ_b , σ_g are standard deviations for the local topography and the equivalent gravity anomaly, respectively.

Because the distributions of the local topography and equivalent gravity anomaly were not normal, as shown in Figure 4.9, in practice the standard deviation is substituted by the median

absolute deviation (MAD) σ^{MAD}, a robust measurement of dispersion [*Rousseeuw and Leroy*, 2005]. The MAD of the topography b is defined as

$$\sigma_b^{MAD} = median[|b_i - median(b_i)|] \tag{4.6}$$

The topography-to-gradient admittance scale corresponding to (4.6) is 13.5 m/mGal. Since the long wavelengths have been removed, the local topography and the equivalent gravity anomaly in the study area should be distributed around zero. This constraint is applied, that is, their medians are set to zero. The topography-to-gradient admittance scale computed in this way is reduced to 11.6 m/mGal. It is the slope of the red dashed line in Figure 4.8. This indicates that the S is not stable. It varies when different computation methods are used.

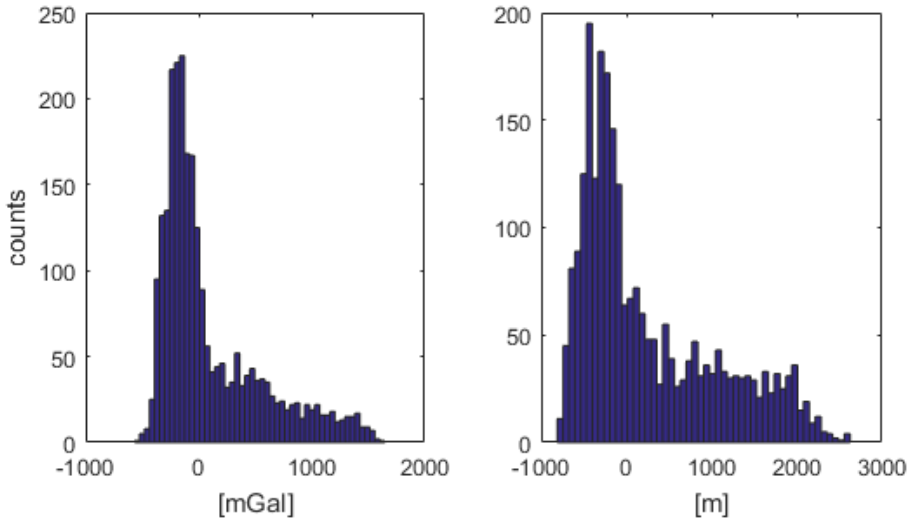

Figure 4.9: Histograms of the local equivalent gravity anomaly and the local topography at places originally constrained by ship sounding.

4.2.4 Results and Evaluation

The band-pass filtered equivalent gravity anomaly (Figure 4.7) multiplied by the topography-to-gradient admittance scale gives the predicted short-to-intermediate wavelength topography. Combining it with the long wavelength regional topography obtained by low-pass filtering of ship sounding (Figure 4.5) gives the total seafloor depth estimation (shown in Figure 4.10), as

indicated by equation (3.3). Since wavelengths shorter than 15 km are omitted, the topography estimation is smooth. Estimation based on the Forsberg method gives the same result, because the first term approximation of Parker's series and Forsberg method are the same, as formula (2.24) shows.

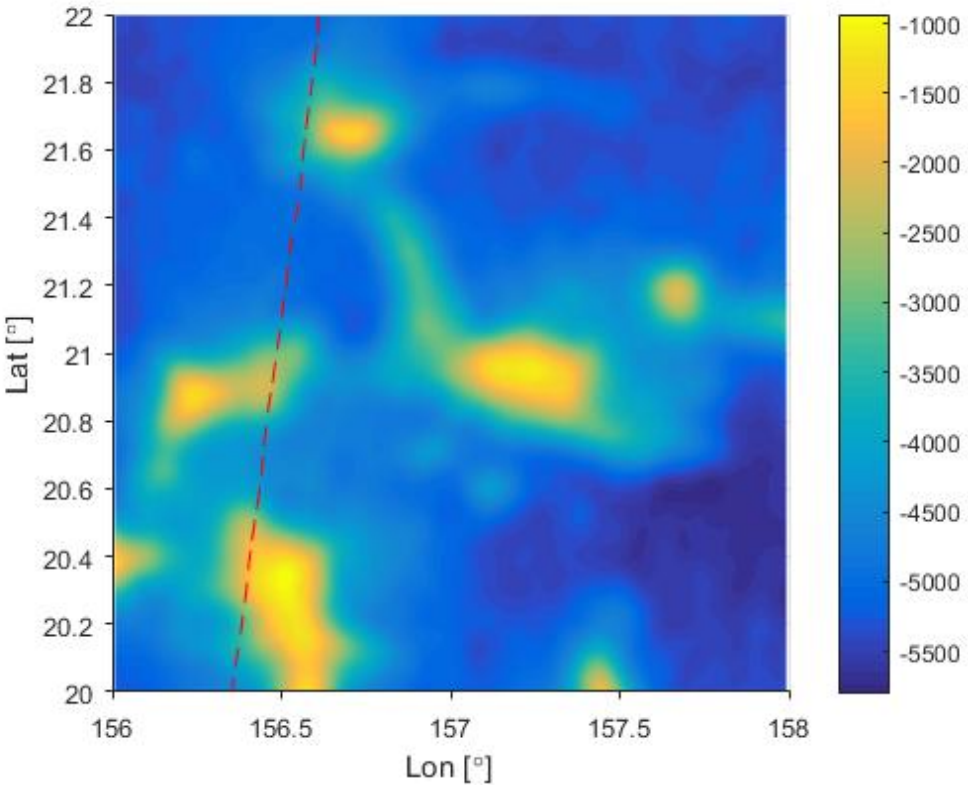

Figure 4.10: The total seafloor depths estimation. The units are meter. The red dashed line is the ship track reserved for quality evaluation.

Figure 4.11 is the profile of depths along the ship track of the vessel *JOIDES Resolution*. The blue cross is the observed depth while the solid line represents the estimated seafloor depth. It shows that the estimation resolved most of the seafloor topography. But the estimation was smooth and did not recover some short wavelength details. Besides, the topography was overestimated at very rugged places. One reason is that wavelengths shorter than 15 km had been suppressed to make the inversion stable; so, some short wavelengths that the ship measurement contains were not estimated. Another contributing factor is the first-term approximation. Along

this ship track the topography varies severely, but the linear approximation of Parker's series that relates topography and gravity gradients is good only at places where the local topography is small compared to the regional topography, provided the sub-topography density is uniform. As discussed in subsection 3.2.1, in a synthesized area similar to the study area, the nonlinear terms can be as large as 48.9 Eötvös. As shown in Figure 4.8, the topography is generally proportional to the equivalent gravity anomaly when the topography is within ± 1000 m. But the topography-to-gradient admittance scale gradually becomes smaller and deviates from the red dashed line when the topography is larger than 1500 m, where the neglected nonlinear terms may bring errors to the estimation.

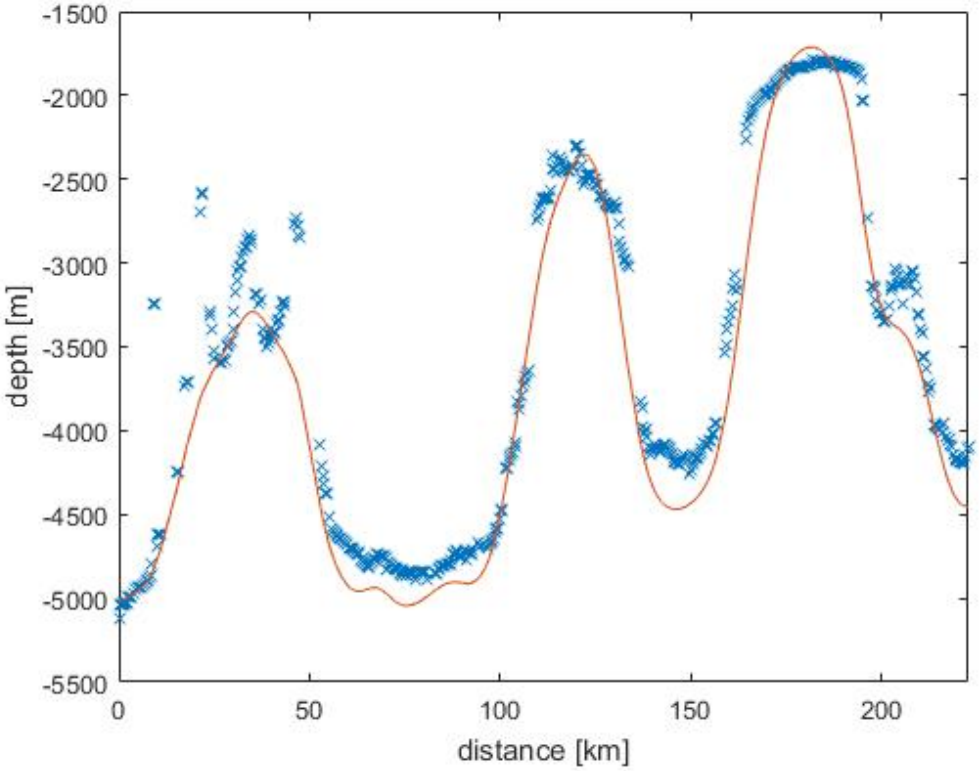

Figure 4.11: The blue crosses are observed depths from *JOIDES Resolution*. The solid line is the estimated depth at corresponding location.

The topography-to-gradient admittance scale S is location dependent. That is to say, the S determined in one area cannot be used in other areas and still provide as good results. Therefore, if the estimation area is large, it should be divided into several small regions each with an

independent S determined from regional gravity gradient and ship sounding pairs. To show the sensitivity of the estimation to the topography-to-gradient admittance scale, the estimation was recalculated using different S. The results are shown in Figure 4.12.

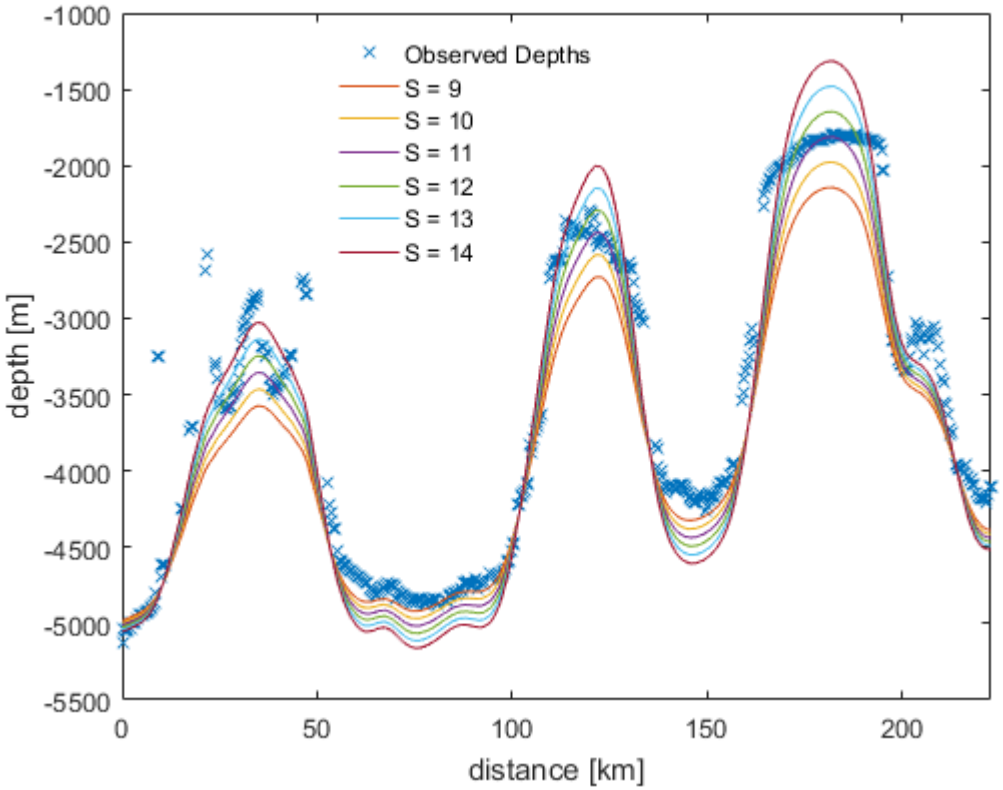

Figure 4.12: The seafloor depth estimations along the ship track of *JOIDES Resolution* with respect to different topography-to-gradient admittance scale S.

The difference between the ship soundings and the estimation at mesh nodes originally constrained by ship data (bottom panel of Figure 4.2) was calculated. Table 4.1 summarizes the statistics of this difference. The histogram is shown in Figure 4.13. The distribution of the difference is not normal, because the normal distribution is symmetric about zero, whereas the skewness of the difference is 0.57. The difference concentrates on small values. The distribution shows that the peak is sharp, and the tails are longer than those for the normal distribution. Therefore, the cumulative distribution of the absolute difference is also computed (shown in

Figure 4.14) to provide another perspective, which shows half of the differences are smaller than 133.66 m, and less than 20% are larger than 300 m.

Table 4.1: The statistics of the difference between ship soundings and estimated seafloor depths at constrained grid nodes. The units are meter.

Max Absolute	Mean	STD	RMS
1378.32	72.81	258.21	268.28

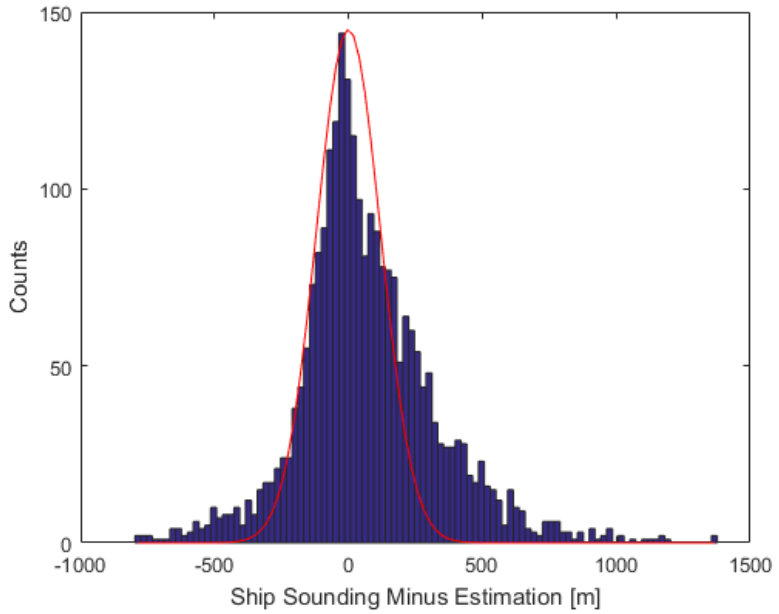

Figure 4.13: The histogram of the difference between ship soundings and estimation. The difference is spread out more to the right of the mean than to the left. The red line is the probability density function of a normal distribution for comparison.

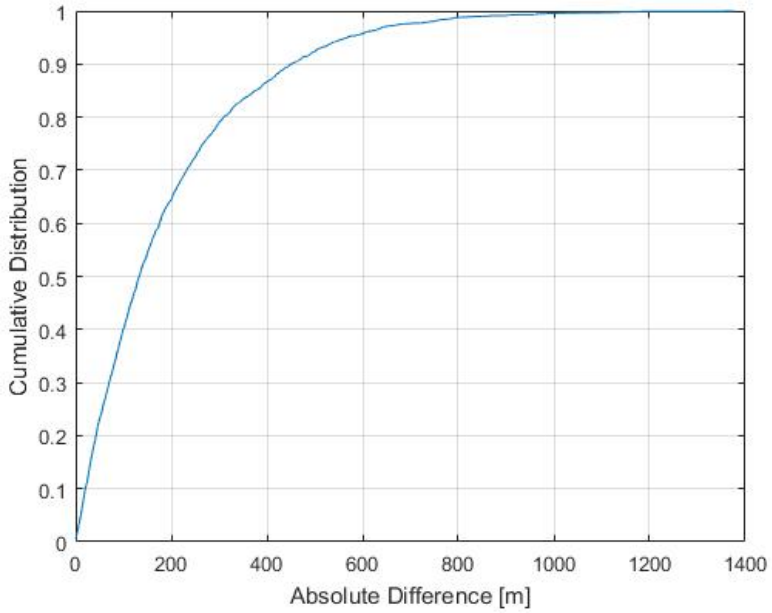

Figure 4.14: The cumulative distribution of the absolute difference between ship sounding and estimation.

The seafloor depth estimations with respect different S are also compared with the ship soundings. The statistics of the differences are shown in Table 4.2. It indicates that the Parker's method is sensitive to the topography-to-gradient admittance scale S.

Table 4.2: The statistics of the difference between ship soundings and estimated seafloor depths with respect to different S shown in Figure 4.12.

S [m/mGal]	Max Absolute [m]	Mean [m]	STD [m]	RMS [m]
9	1522.68	115.71	302.21	323.60
10	1466.51	99.02	270.90	288.43
11	1410.35	82.33	257.06	269.92
12	1370.79	65.64	263.45	271.50
13	1406.18	48.95	288.73	292.85
14	1441.57	32.26	328.57	330.15

4.2.5 Results after Including Shorter Wavelengths

The prediction band of the gravity gradient is set to 15-160 km. It is the same as the one for the gravity anomaly used by *Smith and Sandwell* [1994;1997] in order to make the results from the two methods comparable in subsection 4.4.1. To test the effect of including shorter wavelengths, the shorter cut-off wavelength of the band pass filter (4.3) is reduced, and the corresponding estimation results are shown in Table 4.3.

Table 4.3: The statistics of the differences between ship soundings and estimated seafloor topography at constrained grid nodes for different shorter cut-off wavelengths. The units of the cut-off wavelengths are km, and the units of other values are meter.

Shorter Cut-off Wavelength	Max Absolute	Mean	STD	RMS
15	1378.32	72.81	258.21	268.28
14	1360.43	72.02	258.76	268.60
13	1340.81	71.45	259.56	269.21
12	1326.12	71.35	260.38	269.98
11	1312.73	71.90	261.03	270.75
10	1298.79	72.21	262.19	271.95
9	1282.42	73.13	263.22	273.19
8	1264.73	73.77	264.83	274.92
7	1245.01	74.05	267.15	277.23
6	1219.22	76.11	268.72	279.29
5	1223.26	77.26	272.39	283.13

Table 4.3 shows that, as the shorter cut-off wavelength decreases, the STD and RMS of the estimation error increases. One reason is that a low-pass filter (0.5 gain at 18 km wavelength) was applied to all the along-track altimetry data to ensure a common bandwidth [*Sandwell and Smith*, 1997]; so, the altimetry derived vertical gravity gradient does not contain sufficient short wavelength information.

4.3 Estimation Using Simulated Annealing

4.3.1 Analysis of the Forward Computation in the SA

The truncation theory developed in the subsection 2.3.1 needs rudimentary knowledge of the topography in the study area, i.e., a power-law model that approximates the power spectral density of the topography. The power spectral density of the study area (ranging from E156° to E158° and from N20° to N22°) was computed through formula (2.65) from the global topography model version 18.1 released by SIO. Then a power-law model whose log-log plot (a straight line) best fits the log-log plot of the PSD in a least-squares sense (see Figure 4.15) is given by

$$\bar{\Phi}_{b'}(f) = C \times f^{-\beta} = 0.0043 \times f^{-3.4319}. \qquad (4.7)$$

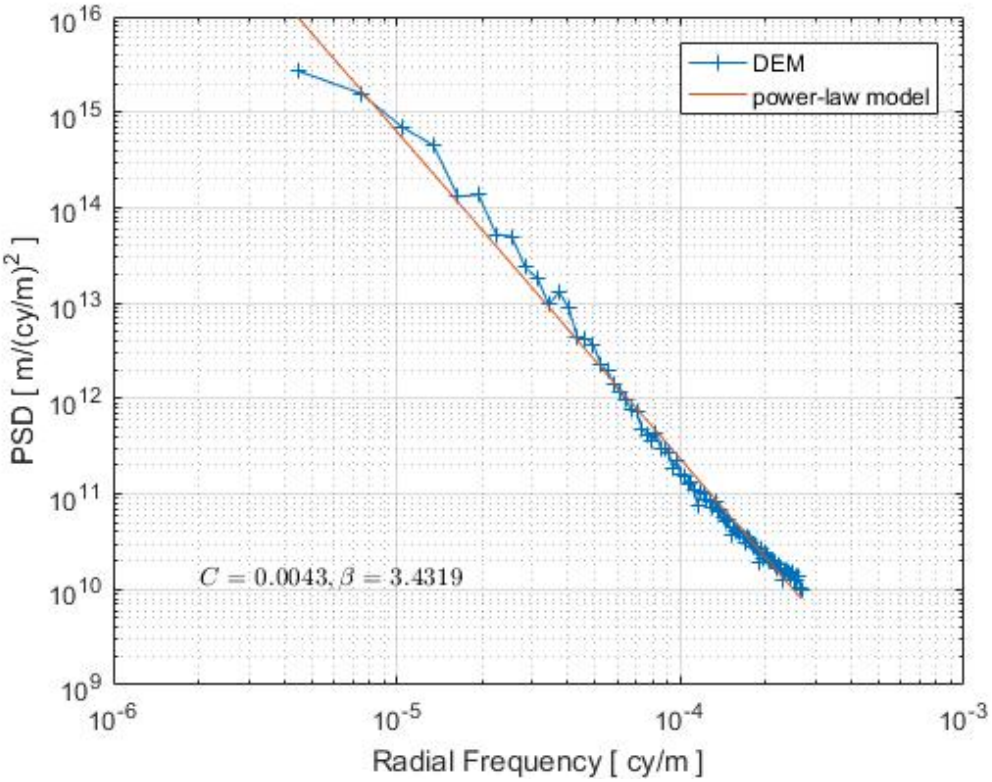

Figure 4.15: The power spectral density of the SIO topography model in the study area, and the power-law model (4.7) that fits the PSD.

Based on this power-law model, the standard deviation of the relative truncation error as a function of the truncation distance s_0 from the computation points was calculated through formula (2.66), and is shown in Figure 4.16. Note that s_0 is implicitly contained in $\left(\breve{\omega}_{zz}\right)_k$, which can be numerically computed from (2.57).

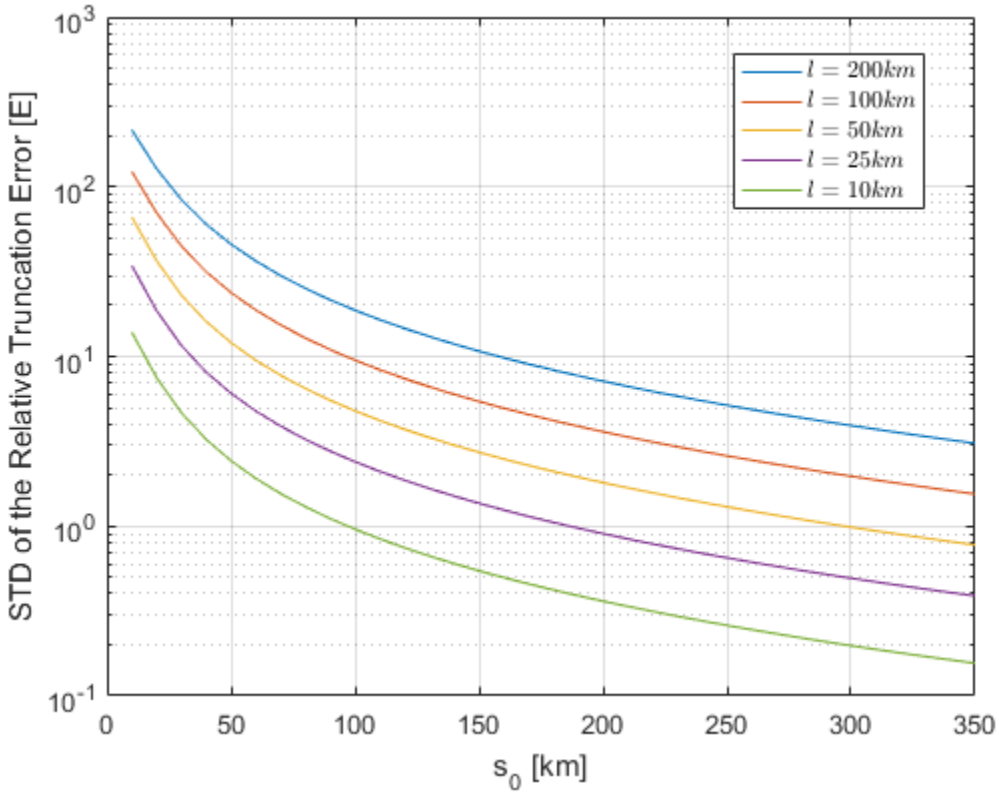

Figure 4.16: Relative truncation error between two points separated by a horizontal distance l versus truncation distance s_0. The mean sea depth is $d = 4828.8$ m in the study area.

The relative truncation error is the difference of the far zone topography effect between two points separated by a horizontal distance l. Figure 4.16 shows that, for a given l, increasing the truncation distance, s_0, reduces the relative truncation error. Figure 4.16 also shows that for a

given s_0, the relative truncation error increases as the separation distance l increases. This suggests that a small study area should be adopted for simulated annealing, considering that in SA method as implemented here assumes that the far zone effect is the same for all points in the study area. If the study area is large, then we should divide it into several small regions and invert one region at a time, otherwise the assumption of a constant far zone topography effect is no longer valid. A small study area usually leads to a small number of seafloor topography parameters and thus benefits the simulated annealing by allowing a faster temperature cooling schedule (as shown by equation (3.40)).

On the other hand, in the simulated annealing technique, the topography to be determined is surrounded by a padded-topography model. During the SA iterations, the errors in the padded-topography model propagate to the unknown topography. This propagated error is larger at the edge of the study area where more of the padded-topography model is used. To reduce this error, the topography to be estimated by SA should cover as large an area as possible.

Combining the two considerations above, given a certain truncation distance s_0, the size of the study area can be set to the largest l whose corresponding relative truncation error is small enough, so that the far zone effect can be assumed uniform for the entire study area. Figure 4.16 shows that if the study area remains at 2°×2° (about 222 km×222 km, that is, l=222 km), a 350 km truncation distance reduces the relative truncation error to 3 Eötvös, which is smaller than the assumed VGG data accuracy (also a typical measurement accuracy of airborne gravity gradiometry is 5~7 Eötvös [*Selman*, 2013]).

Because the data do not contain information higher than the Nyquist frequency, the sampling intervals of the vertical gravity gradient and the seafloor topography limit the resolution that the SA method can achieve. The grid size of the vertical gravity gradient data is 1′×1′, corresponding to a Nyquist wavelength of about 3.7 km. Therefore, there is no need to use intervals shorter than 1.85 km when building topography models. The resolution error computed through formula (2.73) based on the power-law model (4.7) is 8.8e-7 Eötvös, which is negligible.

4.3.2 Data Preparation and SA Configuration

The geodetic coordinates for the gravity gradients and the SIO global seafloor topography model were transformed to local Cartesian coordinates with origin (E157°, N21°, 0 m) through GEOTRANS software version 3.5 released by the National Geospatial-Intelligence Agency's office of geomatics.

The topography over the study area was divided into a mesh using local Cartesian coordinates with interval of 1713.8 m along the West-East direction and 1839.4 m along the South-North direction. The coordinates of the middle points between adjacent mesh nodes were calculated.

Then for each mesh node, its nearest west, east, south, north middle points were chosen as boundary to build a rectangular prism representing the seafloor topography at the mesh node, with each face of the prism parallel to one of the coordinate planes. The topographic height served as the upper boundary of the prism, and the mean depth as the bottom boundary. For each VGG observation point, the topography within its near zone of radius, 350 km (about 3.2°), was used to conduct the forward computation of the gravity gradient. The topography outside the 2°×2° study area was substituted by the global topography model version 18.1 released by the Scripps Institution of Oceanography [*Smith and Sandwell*, 1997] to make the forward computation for observation points in the study area margin possible, see the schematic diagram shown in Figure 4.17. Therefore, the topography used to forward-compute the gradients in the 2°×2° study area covers 9°×9°, ranging from E152.5° to E161.5° and from N16.5° to N25.5°. Only the topographic heights within the central 2°×2° are unknown parameters, and the outside topography was fixed to values from the SIO global topography model. This model, with 1′×1′ resolution is resampled to a mesh with the same interval as the study area (1713.8 m along the West-East direction and 1839.4 m along the South-North direction) using the nearest-neighbor interpolation. The forward computation for observation points uses topography that is a composite of both known and to-be-solved parameters. Note that the forward computation algorithm provides the Z-Z component of the gradient with respect to the local Cartesian coordinate, whereas the observed gravity gradient is the vertical-vertical component with respect to the perpendicular to the reference ellipsoid. Since our study area is small, this discrepancy was neglected (along the meridian, the discrepancy is 1-cos(1°) = 0.015% at most.).

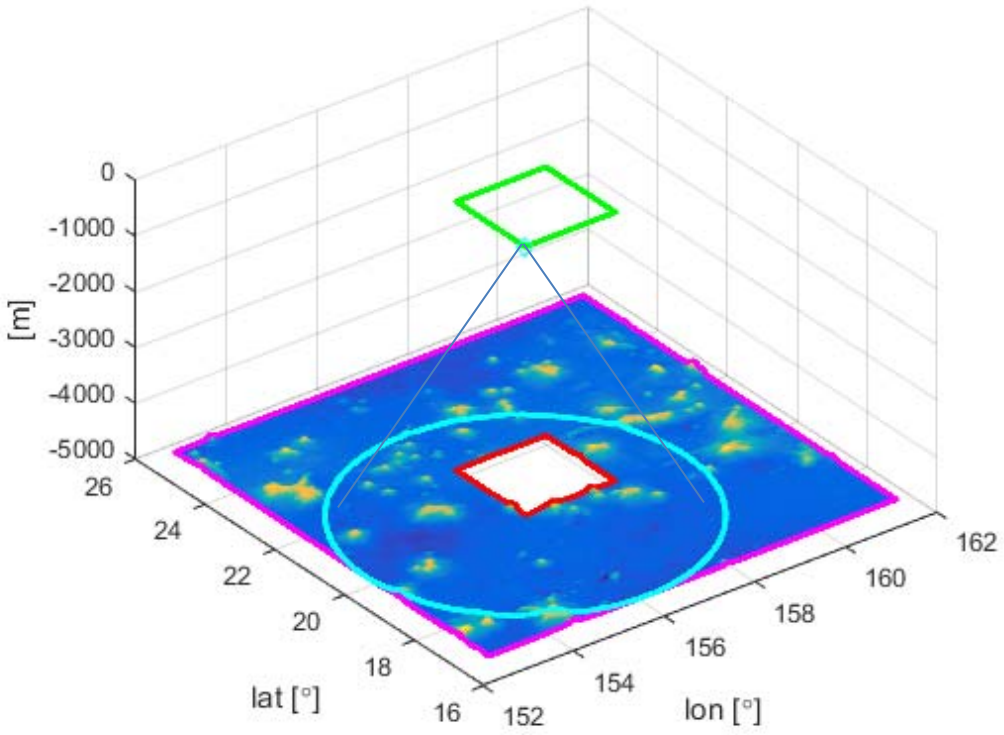

Figure 4.17: The green rectangle represents the range of observed vertical gravity gradients. The area directly beneath it and marked by a red rectangle is the unknown seafloor topography to be estimated. The topography between the red and the magenta rectangles are fixed values from SIO global topography model version 18.1. It is called the padding area. In this figure, the cyan circle marks the near zone topography needed to forward compute the vertical gravity gradient at a corner. The radius of the cyan circle is the truncation distance s_0 that defines the near zone.

The search limit of the unknown seafloor topography (i.e. the state vector in the simulated annealing) can be set to constant values, e.g., the upper search limit could be set to the sea surface and the lower limit could be set to 1 km below the maximum depth over the study area. But the computations are wasted if one uses too large a search space. Considering the facts that the SIO global topography model is based on a fit to ship soundings [*Smith and Sandwell*, 1997] and that our SA method mainly improves the estimation of the topography due to originally neglected nonlinear effects which are not large, the search space was reduced by setting the upper and lower search limits of the seafloor topography at each grid point to 1 km above and 1 km below the depth value interpolated from the SIO global topography model. The mean of the difference between the VGG observations and the VGG forward computed from the SIO global

topography model indicates the magnitude of the offset due to far zone mass. For example, in this area the mean of the difference is -2.9 Eötvös, and then the search domain for the gravity gradient offset due to far zone mass was empirically set to $-5 Eötvös \le \Delta \le 0 Eötvös$. The tuning parameters for the simulated annealing are listed below.

Table 4.4: The tuning parameters.

T_0^i	n^i	m^i	D	Q
1	$\log(1e7)$	$-\log(1e-4500)$	16506	16506

In this experiment, the SA iteration is terminated when the number of iterations reaches $1e6$. There are typically other criteria (e.g., terminate the iteration when the difference in cost function between transitions is smaller than a preset threshold for a certain number of times), but this is the only one that I used because it provides accurate control to the program running time.

4.3.3 Results of the Simulated Annealing

The program ran on the supercomputer Oakley at the Ohio Supercomputer Center and exited after $1e6$ iterations, as set in the termination criteria. The results are shown below. Figure 4.18 indicates that the cost decreases as the iteration number increases. It has dropped less than two orders of magnitude during the annealing process. The number of the iterations needed by the SA to converge is related to the number of unknown parameters in the state. The greater the number of unknown parameters, the more iterations are needed.

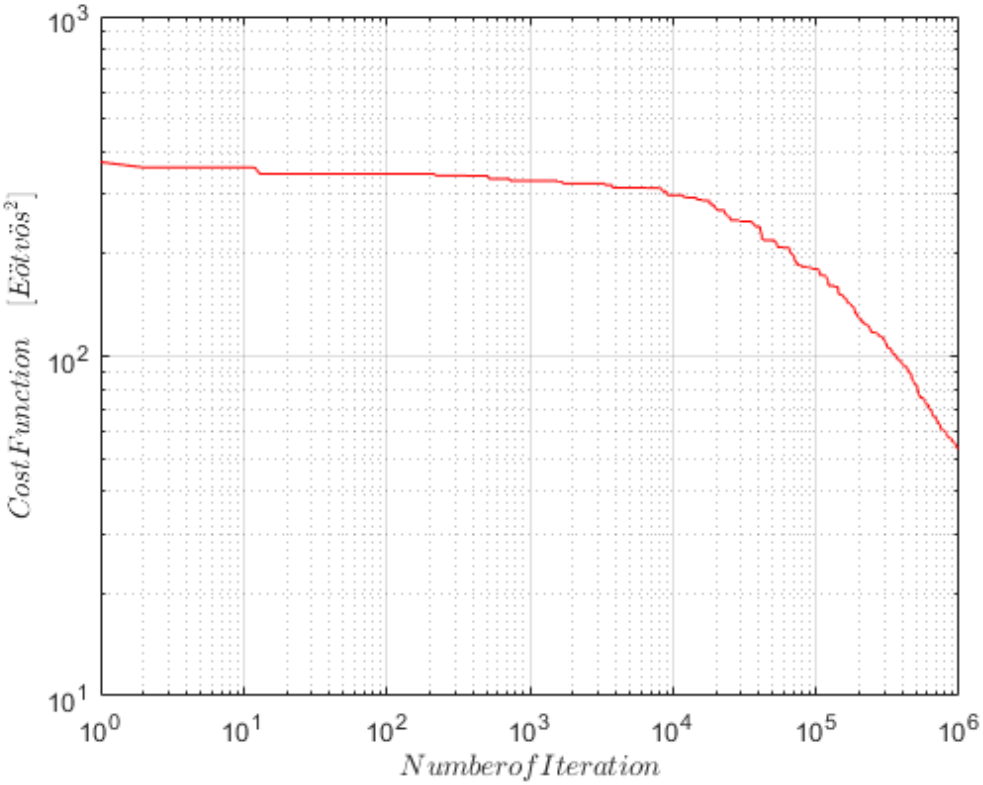

Figure 4.18: The cost function decreases during annealing.

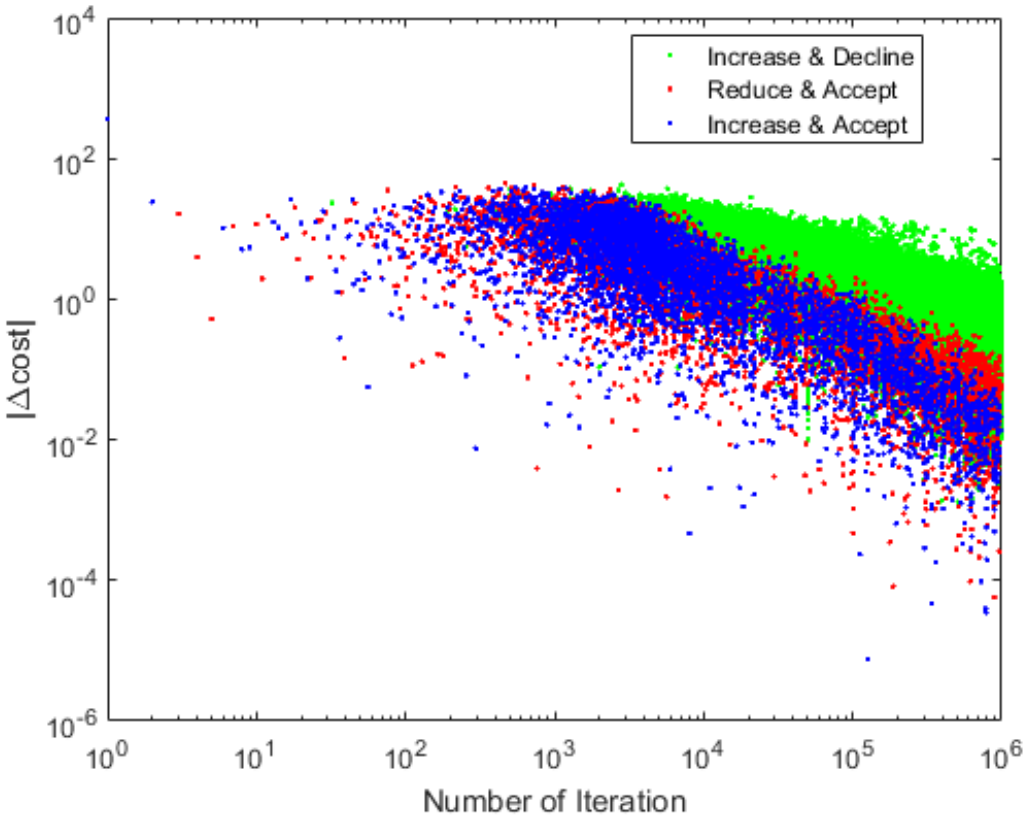

Figure 4.19: The change of cost function between transition. Red dots mean that the newly generated state reduces the cost function and the transition to the new state is accepted. Green dots mean that the new state increases the cost function and the transition to the new state is rejected by the Metropolis criterion. Blue dots mean that the newly generated state increases the cost function, but the transition is accepted.

As shown in formula (3.36), a new state is generated by adding a disturbance to the old state. The disturbance is a stochastic variable controlled by the temperature. Figure 4.19 indicates that, at the beginning when the temperature is high, the disturbance and the resulting $|\Delta\text{cost}|$ are large. Most of the new states are accepted even if they increase the cost function. As the iteration proceeds, the temperature decreases exponentially. This leads to a gradually diminishing disturbance and $|\Delta\text{cost}|$. That is, the probability distribution of the disturbance gradually concentrates on a smaller disturbance. As the temperature decreases, the probability of accepting the transitions which increase the cost function gradually becomes low. The Metropolis criterion ensures that the transition which increases the cost function can be accepted with probability,

thus the states have the ability to escape from a local minimum. At the end stage when the temperature is low, this probability becomes low as well, so that only the transitions reducing the cost function are accepted. In the meantime, the state and the $|\Delta \text{cost}|$ can only change with a tiny amplitude. The state then refines its precision and the cost function approaches the global minimum.

The seafloor depth (topography minus mean depth) as estimated through simulated annealing is shown in Figure 4.20, and its power spectral density (PSD) is shown in Figure 4.21. The other parameter in the state vector, the gravity gradient offset due to mass outside the near zone, is -3.1 Eötvös. The PSD of the topography as a function of radial frequency was computed through the following formula by azimuthally averaging the 2-D periodogram:

$$\Phi_{bb}\left(\bar{f}\right) = \left\langle \left(\mathcal{F}\left(b\right)\right)^{*} \mathcal{F}\left(b\right) \right\rangle \tag{4.8}$$

where Φ_{bb} is the power spectral density of the topography, $\bar{f}$ is the radial frequency, $\langle\ \rangle$ is the average operator, and the asterisk denotes the complex conjugate.

The PSD of the topography may be approximately represented by the following power law [*Jekeli*, 2013a], which is a straight line with negative slope in the log-log figure,

$$\Phi = C\bar{f}^{-\beta} \tag{4.9}$$

where C and β are constants. Therefore, in Figure 4.21 the power at frequencies higher than 7e-5 cy/m represents mainly errors in the estimation.

One may claim that the seafloor topography was recovered from the vertical gravity gradient, but the result contains high-frequency errors. The next step is to design a low-pass filter for the result and analyze the estimation accuracy.

The high-frequency error is generated due to the large dimensionality of the inversion and the comparatively small number of iterations used. Several simple numerical tests were conducted using errorless, simulated topography and VGG data sets, in which the number of unknown topography parameters was increased from 4 to 100 to see its effect on the estimation accuracy. The result shows that the estimation accuracy of SA decreases as the number of unknown parameters increases. The error is of high-frequency character. As the number of topography parameters increases, the cooling schedule (3.39) becomes prohibitively slow (see the red line in Figure 4.22) and thus the needed computation load increases exponentially fast. As a compromise (see the blue line in Figure 4.22), (3.40) was used instead. This leads to a smaller number of iterations, but the cooling schedule decreases faster. As discussed in subsection 3.3.1,

the cooling schedule (3.40) had been successfully applied to a number of complex problems with large dimension.

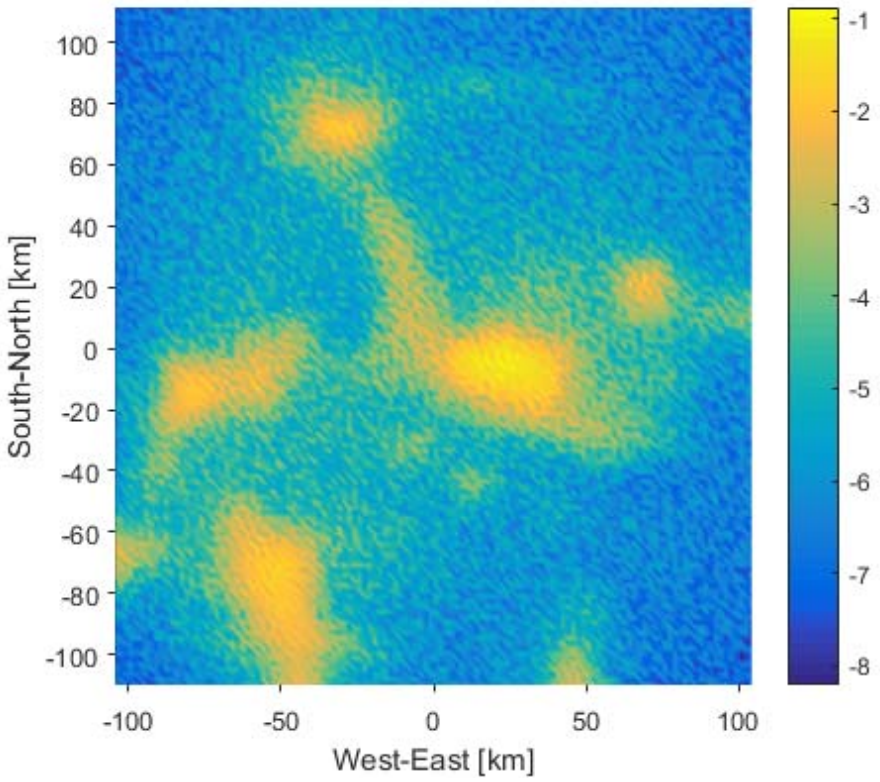

Figure 4.20: The seafloor depth estimated through simulated annealing. The units of the color bar are kilometer.

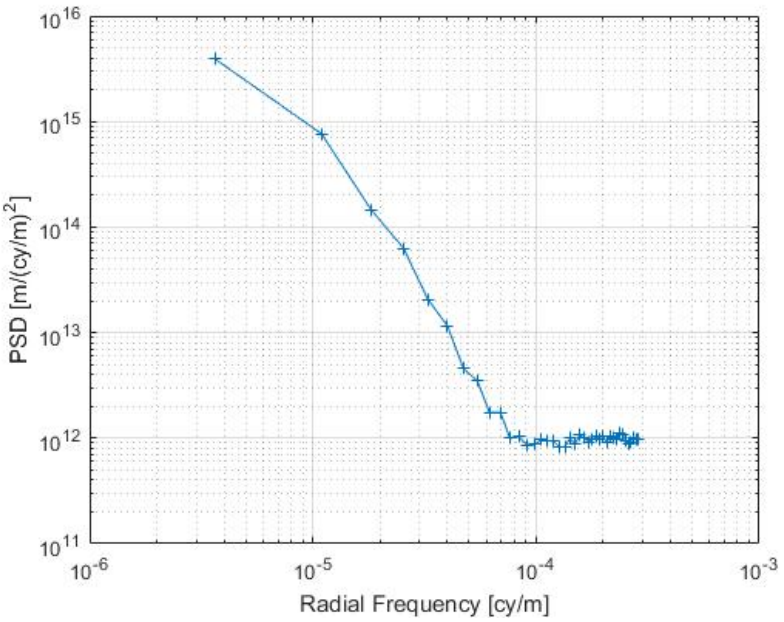

Figure 4.21: The Power spectral density of the topography estimation.

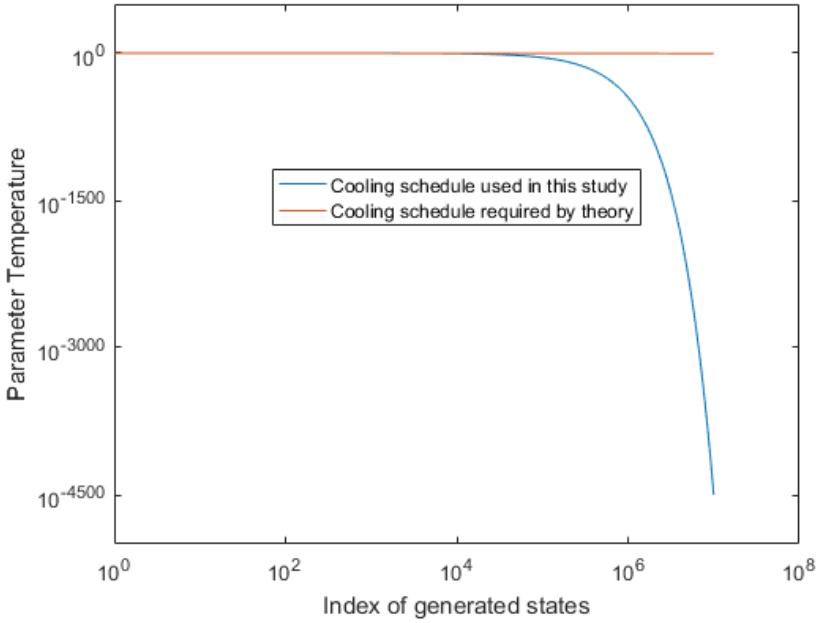

Figure 4.22: The cooling schedule (3.40) used in this study versus $T_k^i = e^{-k^{\frac{1}{16506}}}$, a particular cooling schedule (3.39) that statistically guarantees finding the global minimum.

The simulated annealing needs the temperature to be low at the ending stage of the iteration in order to converge. This is tuned by c^i through m^i and n^i. As a result, the theoretical cooling schedule does not approach 10^{-4500} until 10^{66279} iterations, if c^i is set to 1.

4.3.4 Low-pass Filtering the Estimated Seafloor Topography

Because Figure 4.21 shows that the power at frequencies higher than 7e-5 cy/m is mainly caused by error, the same filter as in Parker's method, the Gaussian low-pass filter (Figure 4.23) with cut-off frequency of 6.67e-5 cy/m (wavelength of 15 km)

$$W_l = e^{-2\times\left(2.8109\times10^3\,\pi\bar{f}\right)^2} \tag{4.10}$$

was applied to the seafloor topography estimation shown in Figure 4.20 to make the results of SA and Parker's method comparable. The filtered result is shown in Figure 4.24.

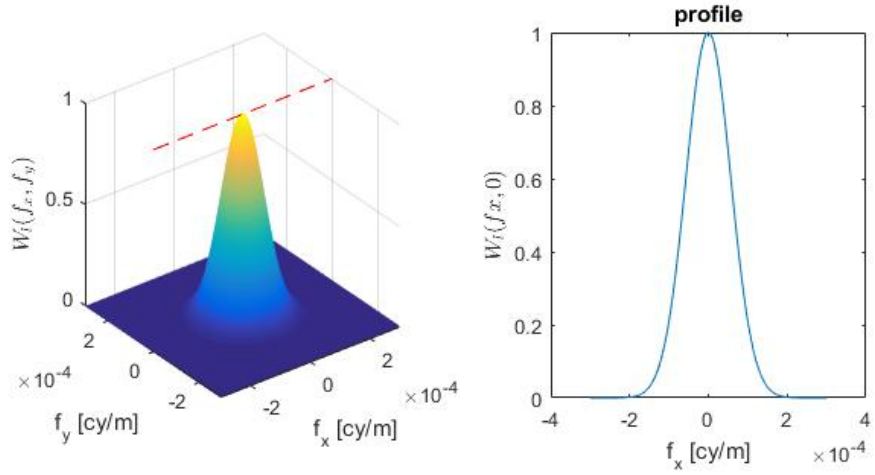

Figure 4.23: The frequency response of the Gaussian filter applied to the SA estimated topography (left panel). The right panel shows a profile (red dashed line in the left panel) for $f_y = 0$ cy/m.

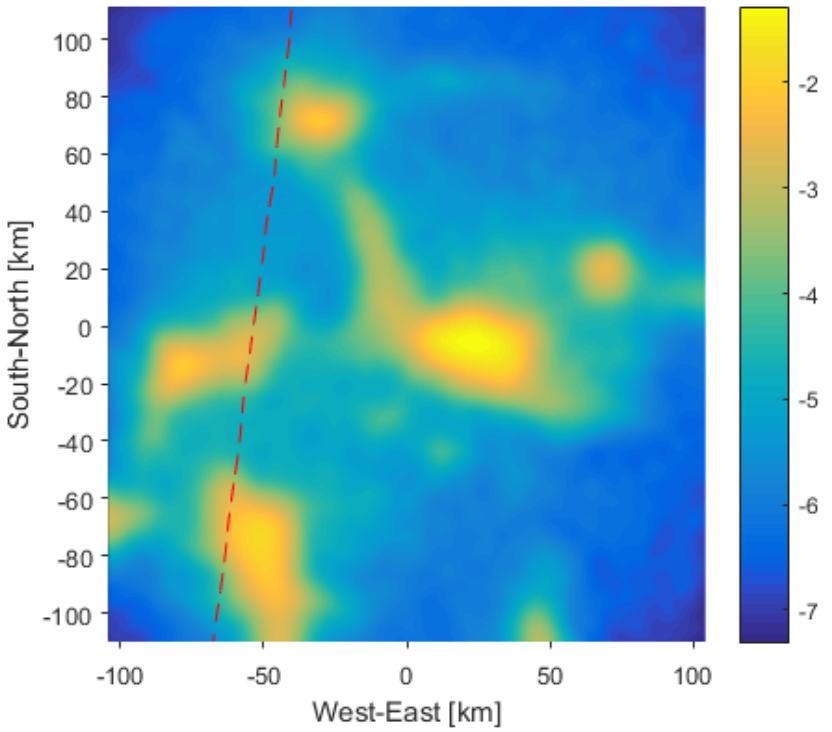

Figure 4.24: The filtered topography estimation. The units are km. The red dashed line is the ship track of the vessel *JOIDES Resolution*.

4.3.5 Evaluation

Figure 4.25 presents the seafloor depth estimated using simulated annealing and the bathymetric depth measured by the vessel *JOIDES Resolution* in 2009.

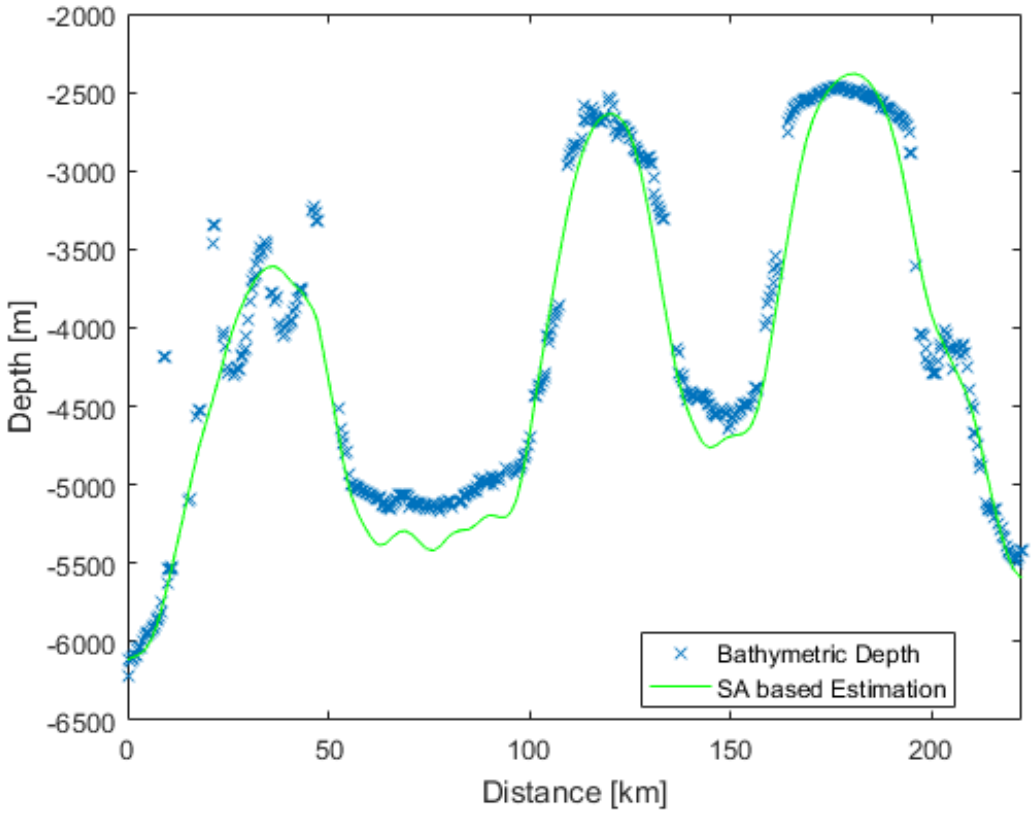

Figure 4.25: The blue crosses are bathymetric depths measured by the vessel *JOIDES Resolution*. The green solid line is the depth at corresponding locations estimated through simulated annealing.

Similar to the lower panel of Figure 4.2, the single-beam bathymetric depths from the NCEI were gridded on the same mesh as the topography model used in this section. At the mesh nodes constrained by ship sounding, the difference between the topography estimated by the SA method and the ship bathymetric depth was computed. The statistics of the differences are shown in Table 4.5.

Table 4.5: The statistics of the difference between topography estimation and the ship soundings at constrained mesh nodes. The units are meter.

Max Absolute	Mean	STD	RMS
1307.69	2.37	235.95	235.97

The histogram of these differences is shown in Figure 4.26. The skewness of these differences is 0.88. As mentioned in subsection 4.2.4, because the peak of the histogram is sharp, and the tails are longer than those of the normal distribution, the RMS cannot fully represent the distribution. So, the cumulative distribution of the absolute difference is also computed and presented in Figure 4.27. It shows that half of the absolute differences are smaller than 112 m. More than 75% of the differences are smaller than 200 m.

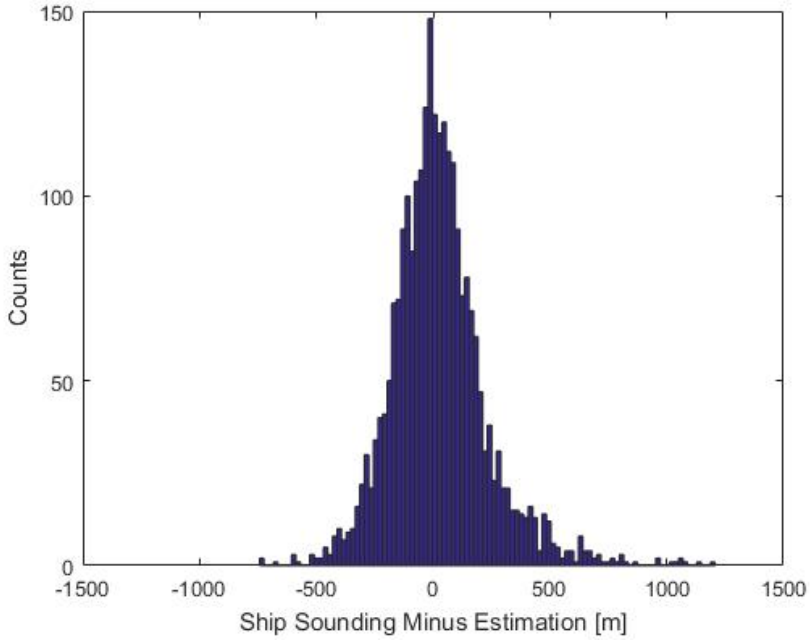

Figure 4.26: The histogram of the difference between ship soundings and estimation.

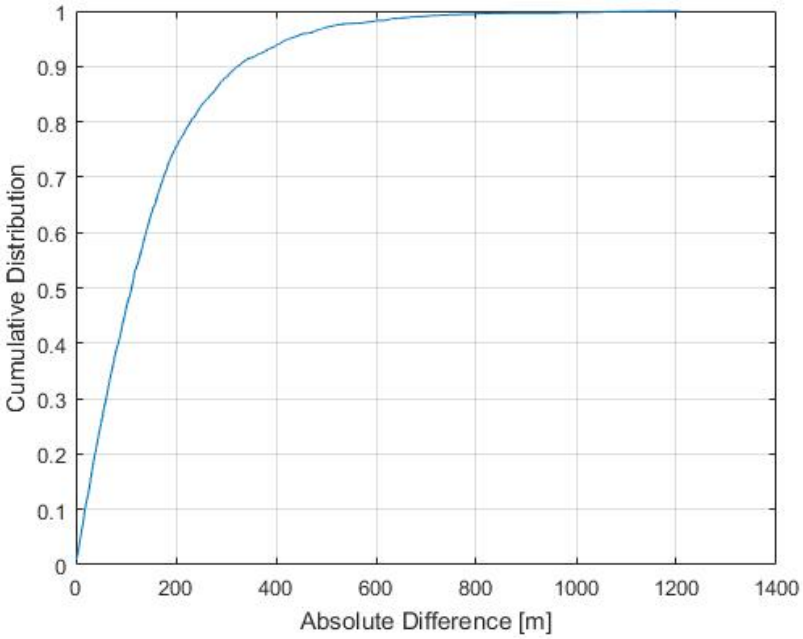

Figure 4.27: The cumulative distribution of the absolute difference between ship sounding and estimation.

4.3.6 Other Tests of the Simulated Annealing Algorithm

As shown in the bottom panel of Figure 2.3, the vertical gravity gradient is not sensitive to the long-wavelength topography due to the factor $-2\pi\bar{f}$ in the gradient admittance. Therefore, removing the long wavelengths from the VGG and the topography may improve the estimation accuracy.

This idea was tested in this subsection. The long-wavelength topography (>160 km) shown in Figure 4.5, rather than the mean depth, was used as the bottom boundary of the prisms that represent the seafloor, and the seafloor topography still served as the upper boundary of the prism. The forward-modeled VGG is thus attributed strictly to the shorter wavelengths of the seafloor topography and computed by

$$ {}^{i}\Gamma_{zz}^{comp}\left(b_j\right) = G\Delta\rho \arctan \frac{(x-\xi)(y-\eta)}{(z-\zeta)\sqrt{(x-\xi)^2+(y-\eta)^2+(z-\zeta)^2}}\Bigg|_{\xi=\mathrm{xw}_j}^{\mathrm{xe}_j}\Bigg|_{\eta=\mathrm{ys}_j}^{\mathrm{yn}_j}\Bigg|_{\zeta=lrt_j}^{b_j} \qquad (4.11) $$

where lrt_j is the Z-coordinate of the long-wavelength regional topography at j, and all other notations have the same meaning as in (2.51).

The high-pass filter $W_s = 1 - W_l$ was applied to the observed VGG shown in Figure 4.1 to calculate the short-wavelength (<160 km) VGG, where W_l is the low-pass filter defined by (4.2).

The difference between the forward computed and "observed" short-wavelength VGG was used in the computation of the cost function.

Besides removing long wavelengths, a series of tests was also conducted in this subsection to see the effects of using a smaller truncation distance, and using a smaller study area.

In test 0, the truncation distance was 49 km, and the study area spanned 2° (about 220 km) along latitude and longitude. Figure 4.16 shows that the corresponding maximum relative truncation error is about 50 Eötvös, which is not acceptable and suggests adopting a larger truncation distance. The test 0 served as a reference. The tests from No. 1 to No. 3 modified one condition at a time. Compared with test 0, test 1 increased the truncation distance to 350 km. In fact, test 1 is the numerical experiment shown in section 4.3. Then based on test 1, test 2 removed the long wavelengths from the observed vertical gravity gradient, and forward computed its counterpart, the calculated vertical gravity gradient, using masses between seafloor topography and long-wavelength topography. Finally, test 3 divided the study area into four 1°×1° regions, computed topography of one region at a time, and spliced the results together. All other settings were the same as for the test 2.

The statistics of the results are shown in Table 4.6, which indicates that increasing the truncation distance significantly improved the estimation accuracy of the simulated annealing. This modification reduces the maximum absolute value of the difference between the estimated seafloor depths and the ship sounding measurements, as well as the standard deviation (STD) and root mean squared (RMS) value of this difference. An exception is the mean value of the difference.

However, improvements obtained by removing the long wavelengths is not significant, since the VGG caused by long-wavelength topography is small.

Dividing the 2°×2° study area into 4 small regions and estimating one region at a time does not improve the estimation accuracy. This may be explained by the large truncation distance used in test 2 and 3. According to Figure 4.16, the maximum relative truncation error for $s_0 = 350\,\text{km}$, l=200 km (~ 2°) is 3 Eötvös. Reducing l to 100 km (~1°) decreases this value to 1.6 Eötvös. The improvement is not significant. However, the effect of errors in the padded-topography model that propagates into the unknown topography was enlarged when the area size is reduced.

This effect may be larger than the improvement on the relative truncation error, and thus decreases the estimation accuracy.

Table 4.6: The statistics of the differences between topography estimation by SA and the ship soundings at constrained mesh nodes. The units are meter.

	Settings			**Results**			
Test No.	Truncation distance (km)	Long wavelengths removed	Area size in one inversion	Max absolute (m)	Mean (m)	STD (m)	RMS (m)
0	49	×	2°×2°	1379.66	-4.68	308.80	308.89
1	350	×	2°×2°	1307.69	2.37	235.95	235.97
2	350	✓	2°×2°	1206.30	-11.31	224.74	225.02
3	350	✓	1°×1°	1356.97	-16.83	265.96	266.49

4.4 Comparison of the Estimation Results

4.4.1 Comparison with the SIO Topography Model

The global topography model [*Smith and Sandwell*, 1994; 1997], released by the Scripps Institution of Oceanography (SIO), has been incorporated into most publicly available global seafloor topography models, like Google Earth and the General Bathymetric Chart of the Oceans (GEBCO) [*Marks and Smith*, 2006; *Marks et al.*, 2010]. It was predicted from altimetry-derived gravity anomalies using Parker's formulation. In this section, it is used to compare with the estimation result in section 4.2, namely the seafloor topography estimated from altimetry-derived gravity gradients using Parker's formulation. Note that *Smith and Sandwell* modified their topography prediction to force the predicted topography at grid cells constrained by ship soundings to fit the bathymetry-implied heights. Therefore, their unadjusted prediction (see left panel of Figure 4.28), rather than the final released version of the global topography, should be used. The difference between their unadjusted topography prediction and the constraining ship soundings was calculated. The statistics of the difference are shown in Table 4.7.

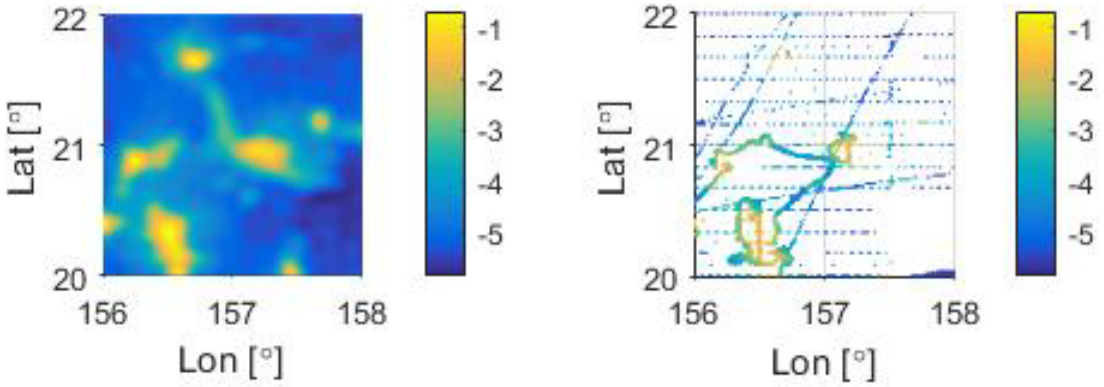

Figure 4.28: (left) The unadjusted total global seafloor depth prediction released by SIO. (right) The grid cells constrained by ship soundings. For cells with more than one bathymetric depth, the median value is retained. The units of the colorbar are kilometer.

Table 4.7: The statistics of the differences between *Smith and Sandwell*'s unadjusted prediction and the ship sounding at constrained grid cells. The units are meter.

Max Absolute	Mean	STD	RMS
1761.39	2.77	301.26	301.28

The seafloor depths in the left panel of Figure 4.28 were predicted from gravity anomalies derived from satellite altimetry, whereas the topography shown in Figure 4.10 in section 4.2 was estimated by Parker's formulation from the altimetry-derived gravity gradients. All other conditions for the two predictions such as gridding interval, filters, cut-off frequency were set to be as close as possible. Comparison between Tables 4.6 and 4.1 shows that the RMS of the differences with respect to the ship soundings for the gradient estimated topography by Parker's formulation is about 11% smaller than the gravity anomaly predicted topography. Note that although the superiority of gravity gradients over gravity anomalies is theoretically analyzed in subsection 2.1.5, the comparison in this subsection cannot serve as a corresponding numerical demonstration since the same essential data (altimetry) were used in both cases.

Hu et al. [2014b] tested their method in the same area. However, they interpolated the topography-to-gradient admittance at control points onto the whole topography grid, which makes their prediction method to some extent similar to direct interpolation of ship soundings. Besides, they compared the ship soundings with the polished SAS model (final released version, which itself should fit the ship soundings) rather than the unpolished one. As a result, the RMS of the difference is only 66.374 m. Therefore, their method is technically incorrect, and thus not compared with the topographies estimated in this chapter.

4.4.2 Comparison Between the Two Methods

In the preceding two sections, the seafloor topography was estimated from the same VGG data set using Parker's formulation and SA, respectively. Both methods assume that the density of the topography is uniform, and make use of a relationship between topography and gravity gradients, although one is in the frequency domain and the other in the space domain.

Parker's method assumes a linear relationship between topography and gravity gradients whereas the SA method removes this linear approximation. As a result, Parker's method cannot provide an accurate topography estimation at the short wavelengths. The reason can be found in Figure

3.4, which is computed from a synthesized topography that is very similar to our study area. At wavelengths longer than 15 km, the coherency between the topography and the vertical gravity gradient is larger than 0.8; so, Parker's method which assumes a linear relation between topography and gravity gradient may perform well. However, at wavelengths shorter than 5 km, the coherency is lower than 0.5. Therefore, at short wavelengths, no matter how accurate the vertical gravity gradient is, Parker's method is not able to infer the seafloor topography as well.

The estimations in both methods are performed in the same spectral band of wavelengths as the SIO global topography model, namely for wavelengths longer than 15 km. Although the Nyquist wavelength of the topography and VGG data sets in the two methods is about 3.5 km, the same Gaussian low-pass filter with cut-off wavelength of 15 km was applied to both topography estimations. Note that although a high-pass filter was used in Parker's method, it is just used to divide the spectral bands of the topography estimated from VGG and from the ship soundings. The final estimation only suppresses wavelengths shorter than 15 km. Tables 4.5, 4.1, and 4.3 are rewritten below for the convenience of comparison.

Table 4.8: The statistics of the differences between topography estimation and the ship soundings at constrained mesh nodes. The units are meter.

Topography Estimation	Max Absolute	Mean	STD	RMS
Unadjusted SIO model	1761.39	2.77	301.26	301.28
FFT	1378.32	72.81	258.21	268.28
SA	1307.69	2.37	235.95	235.97

The comparison between the last two rows in Table 4.8 shows that the RMS of prediction error for the simulated annealing is 12% smaller than for Parker's method. Since the estimations in both methods use the same VGG and perform in the same spectral band of wavelengths, this improvement is mainly attributed to the removal of the linear approximation in the modeled relationship between gravity gradient and topography.

The profile along the ship track of *JOIDES Resolution* is shown in Figure 4.29, which shows that, except a flat region (i.e. for a distance between 55 km and 95 km), in general the SA estimation is closer to the bathymetric depths than Parker's FFT-based estimation.

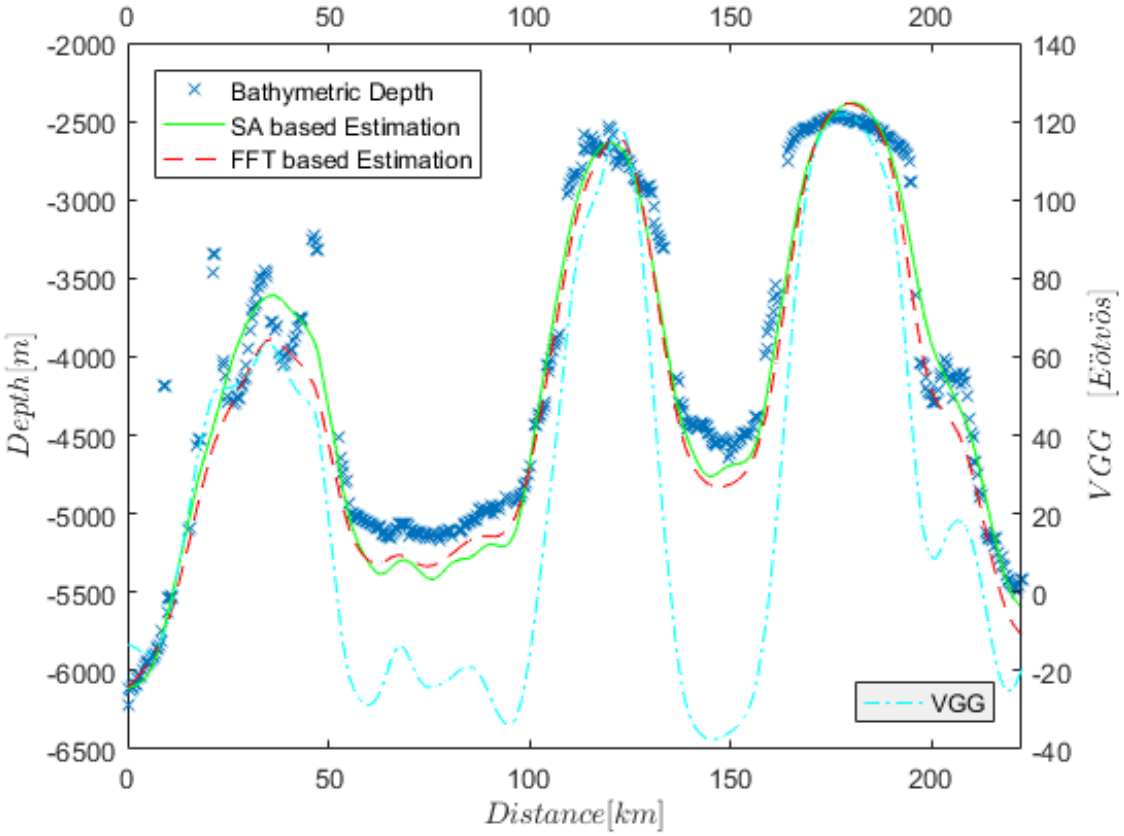

Figure 4.29: The blue crosses are bathymetric depths measured by the vessel *JOIDES Resolution*. The green solid line is the depth along the ship track estimated in section 4.3. The red dashed line is the depth estimated in section 4.2 based on Fourier transform. The cyan dot dashed line is from the vertical gravity gradients along the ship track.

Chapter 5: Sub-topography Density Anomaly

Although the satellite altimetry data cover the global ocean densely except in polar areas, the spatial resolution in gravity anomaly estimation from altimetry is limited in any case. The missing short wavelength component is one of the reasons why the Fourier-based method does not perform well in rough areas. Therefore, an alternative source of gravity data is considered. Airborne gravity gradiometry, whose line spacing is usually smaller than 0.5 kilometer, is a more direct measure of the Earth's gravity field at shorter wavelengths and inherently has the potential to improve not only the accuracy, but also the spatial resolution of the field for improved inference of seafloor topography. Besides, the altimetry-derived gravity gradients released by the SIO only contains vertical-vertical components, whereas the full-tensor airborne gravity gradiometry measures five independent gradient tensor components, which can be combined to further improve the accuracy of topography estimation.

Originally developed by Bell Aerospace (now part of Lockheed Martin), their gravity gradiometer instrument has been put into commercial operation since the late 1990s on three airborne platforms, the airborne gravity gradiometer (AGG) by BHP Billiton Falcon, full tensor gradiometer (Air-FTG), and FTGeX by ARKeX [*Dransfield*, 2007]. Measurements with this instrument enhance the natural resource exploration toolbox and have found an increasing number of applications in the past two decades [*Murphy et al.*, 2012]. Here it is tried to extend the application of airborne gravity gradiometry to seafloor topography estimation for the purpose of achieving higher spatial resolution and accuracy.

The airborne gravity gradient measurements are as yet scarcely available in ocean areas. Although there are two gravity gradient data sets available over the ocean, both were conducted for geologic purposes in areas with complex sub-topography geological structures, where the assumption of uniform density does not hold. Several ways to separate the effect of sub-topography density anomaly from gradient observations were investigated. The effort includes checking the characteristics of the power spectral density of the gradient observations and comparing them to the forward-computed gradients from ship bathymetry. But none of these analyses provided satisfying results. It is easy to understand, since sub-topography geologic structures are exactly what the contemporary commercially operated gradiometers are designed for. Therefore, no attempt can remove the sub-topography density anomaly effect from the gravity gradient observations, but instead we must accept the fact that at some places the sub-topography density anomaly is severe while at some other places the density of terrain is almost constant, where inferring topography from gravity is feasible. I remain optimistic about seafloor

topography estimation from airborne gravity gradients, but showcase a demonstration of the existence of places where sub-topography geologic structures are complex and are the main error source that impedes topography estimation from gravity gradients.

5.1 St. George's Bay Area

In December 2012, Bell Geospace Inc. (BGI) conducted a gravity gradiometry survey over St. George's Bay [*Selman*, 2013]. It is located off the southwestern shore of Newfoundland, Canada, and lies between longitudes -59.43° and -58.38°, and latitudes 47.92° and 48.59°, see Figure 5.1. The FTG full tensor gradiometer is installed on a Basler Turbo BT-67 aircraft, which was flown to gently drape the land topography in order to minimize the distance between measurement altitude and ground. The reported accuracy of the FTG is about 5 to 7 Eötvös [*Selman*, 2013]. The designed (nominal) flight altitude during the entire survey is 80 meters above the water. The flight lines are 400 meters apart, with data sampled along-track at a one second interval, which translates to 59.7 m spatial sampling interval using the 215 km/hour speed. As part of the data processing, BGI projected the gravity gradients onto the Universal Transverse Mercator (UTM) zone 21 N.

Also obtained were high horizontal resolution (10m × 10m) multibeam bathymetry data for this area from the Geological Survey of Canada (Atlantic) [*Shaw and Courtney*, 1997], see Figure 5.1. The reported accuracy of the multi-beam echo sounding is usually in the level of 10 cm [*Ernstsen et al.*, 2006]. Besides, the accuracy of the multibeam sounding is generally evaluated according to the International Hydrographic Organization Standards for Hydrographic Surveys [*International Hydrographic Organization*, 2008], which requires the uncertainty of the reduced depths to be smaller than $0.25 + 0.0075 \times b'$ meter. It is much smaller than the accuracy of the gravity estimated seafloor topography. Therefore, the bathymetric data I obtained are treated as errorless (true) values. The forward-modeled gravity gradients caused by the seafloor topography were computed according to the right rectangular prism method using formula (2.51), with the truncation distance for the near zone set to $s_0 = 30\,km$. According to formulas (2.66) and (2.57), the relative truncation error corresponding to 30 km truncation distance is 0.35 Eötvös, which is one order smaller than the accuracy of VGG observations. The topography in regions not covered by multibeam bathymetry comes from the SIO topography model shown in Figure 5.2, whose spatial resolution is about 1230 m.

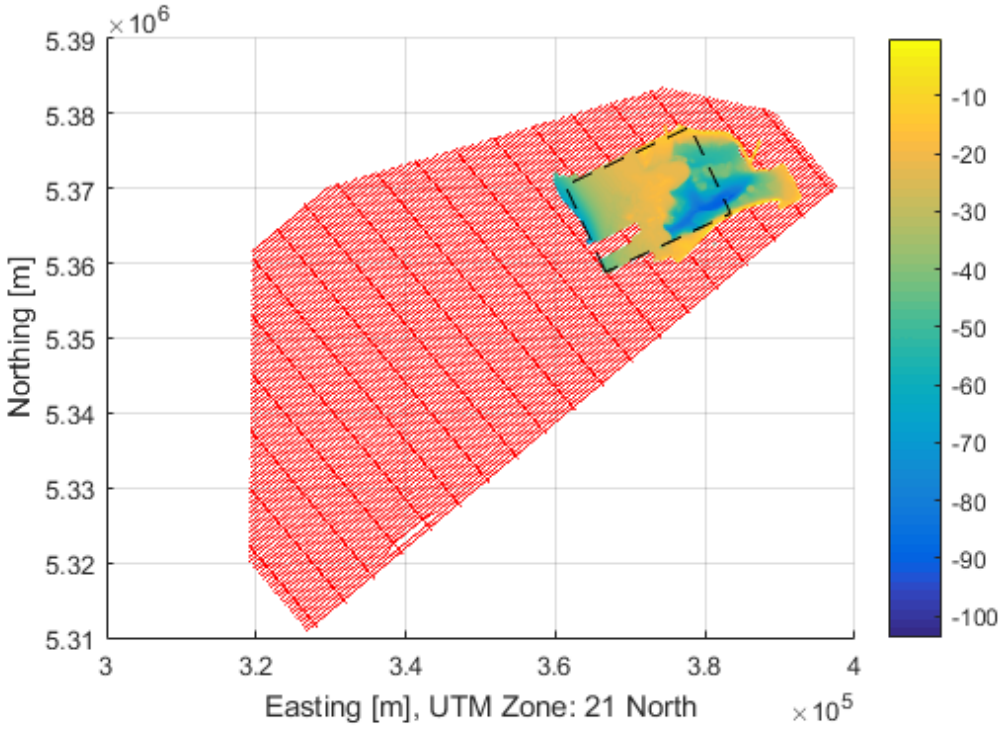

Figure 5.1: The collected data sets, where red dots represent the flight track of gravity gradiometry, and the colored region represents the multibeam bathymetry. The units of the color bar are meter. Only the gravity gradients in the area of the multibeam data (marked by the black dashed-line rectangle) were computed, since the resolution of multibeam bathymetry is much higher than the SIO topography model.

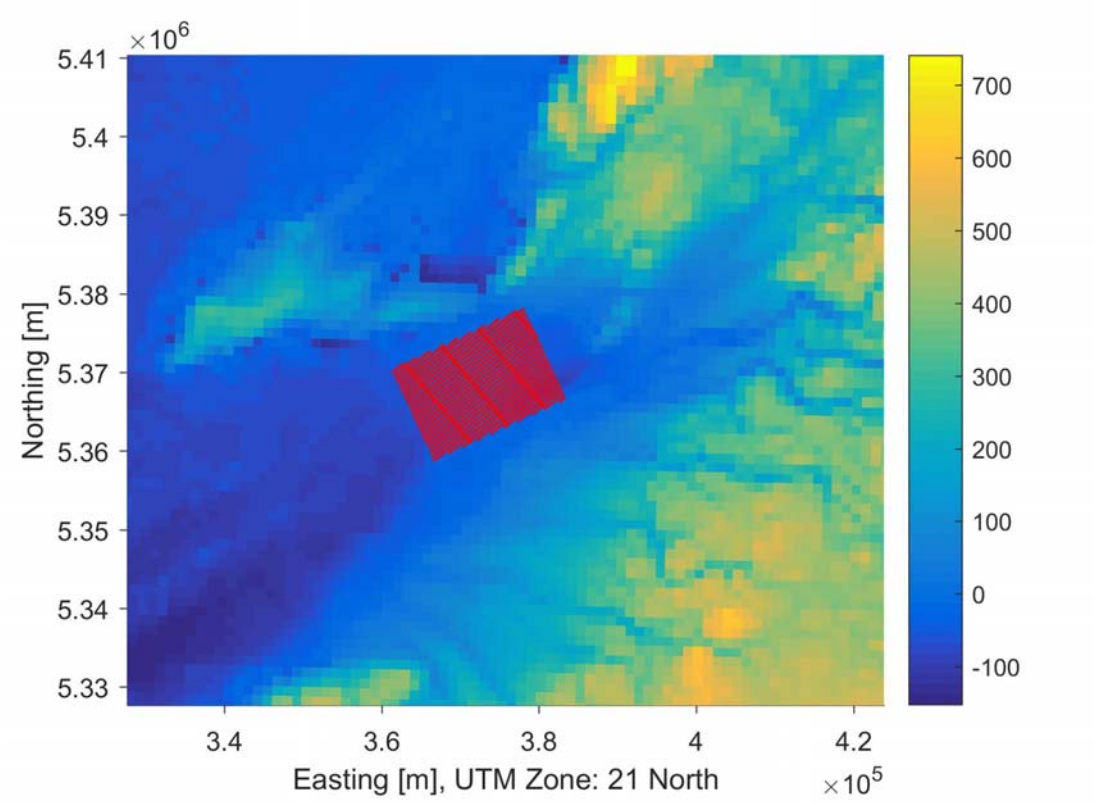

Figure 5.2: The SIO seafloor topography model, with the multibeam bathymetric depths incorporated, that is used in the forward computation. Scale bar units are meter. Red dots denote the location of measured gravity gradients within the rectangle marked in Figure 5.1.

The gravity gradients forward computed from topography are shown in Figure 5.3 (b). They are also called the terrain effects and were computed similarly by BGI. The directly measured gradients are shown in Figure 5.3 (a). Subtracting (b) from (a) gives Figure 5.3 (c). Because a DC offset was removed from the gravity gradient observations by BGI during data processing, the mean of the vertical gravity gradient shown in (a) is near zero although its total value near the Earth's surface is about 3080 Eötvös. From Figure 5.3 we may find that the measured gradients near the easting, x = 375 km, are mainly caused by the steep slope of the seafloor (see the multibeam bathymetry in Figure 5.1 marked by black dashed-line rectangle). In Figure 5.3 (c), apparently only high frequencies are left in this region. However, in the northwest region where the topography is smooth, the measured gradients (a) show abnormally high values, indicating a high-density anomaly beneath the topography. At the southeast corner, there is a trench where the observed gradient is significantly smaller than the terrain effect. One explanation is that the sediments in this trench are less dense than the surrounding seafloor rock.

In summary, over the St. George's Bay area, ocean bedrock is overlaid with thick sediments. The gravity gradient has a large signal but the topography is smooth (Figure 5.1). In addition, at the northwest and southeast corners of Figure 5.3, significant gradient anomaly occurs which might be due to large internal crustal variations. As a result, the terrain effect contributes less than 50% of the gravity gradient observations (the RMS of the terrain effect shown in Figure 5.3 (b) is about 30.5% of the RMS of the directly measured gradients shown in Figure 5.3 (a)). Topography estimation from gravity gradients in this area is feasible, yet very inaccurate since sub-topography density variation introduces large errors.

The following two sections present topography estimation from airborne gravity gradients within the rectangle marked in Figure 5.1 using both the SA and the Fourier methods. The two sections only focus on estimation results since the estimation algorithms are the same as described in chapter 4. For the convenience of computation, all the data sets are rotated -25.0357° about the Z-axis, and then translated by (-2600013, -4700165, 0). The X, Y axes of the new coordinates are called "rotated easting" and "rotated northing" respectively. Finally, they are resampled to a 200 m × 200 m grid (see Figure 5.5).

Figure 5.3: (a) Gravity gradient Γ_{zz} measured by BGI. (b) Γ_{zz} forward computed from topography. (c) is the difference between (a) and (b). Units are Eötvös. Note that the scales are different for (a) and (b).

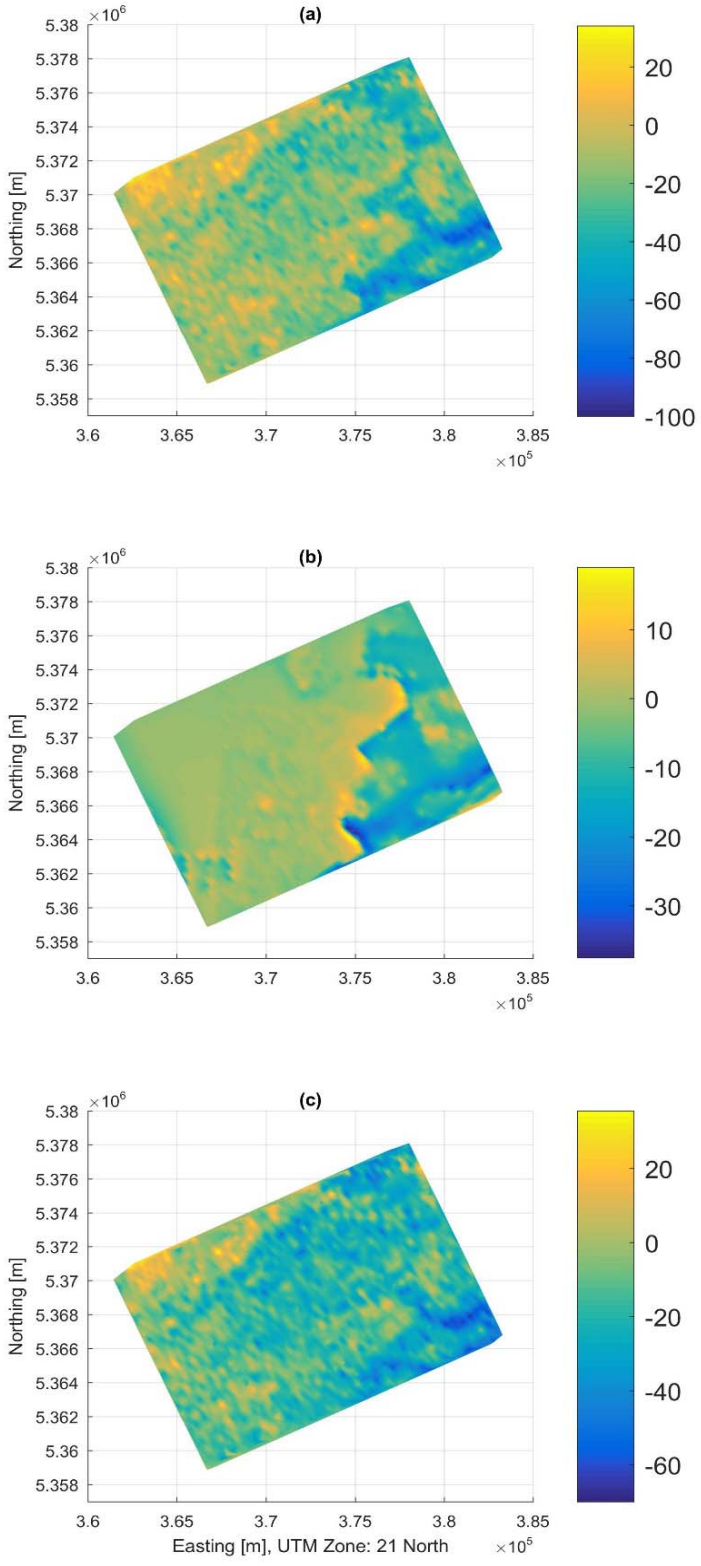
(a)
(b)
(c)
Northing [m]
Easting [m], UTM Zone: 21 North
×10^6
×10^5
5.38
5.378
5.376
5.374
5.372
5.37
5.368
5.366
5.364
5.362
5.36
5.358
3.6
3.65
3.7
3.75
3.8
3.85
20
0
-20
-40
-60
-80
-100
10
-10
-30

Figure 5.3.

5.2 Estimation Using Parker's Formulation

5.2.1 Analysis through Admittance Function

The theoretical uncompensated gravity gradient admittance was computed based on equation (2.49) with the density of the seafloor topography set to 2.2 g/cm^3 [*Selman*, 2013], see Figure 5.4. The distance between measured gravity gradients and the seafloor topography, d, was set to 118.56 m (mean depth of 38.56m plus the nominal flight altitude of 80m).

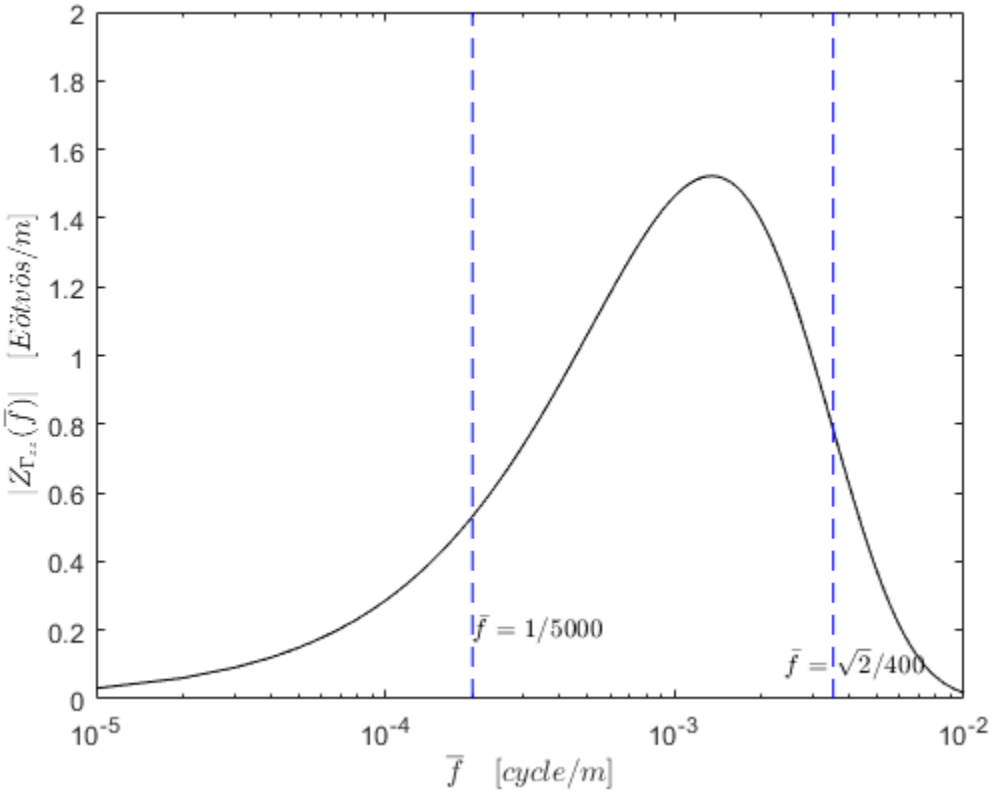

Figure 5.4: The theoretical gravity gradient admittance computed by formula (2.49).

The Nyquist wavelength of the VGG data (shown in Figure 5.5) is 0.4 km. Figure 5.4 shows that, at the corresponding radial Nyquist frequency, $\bar{f} = \sqrt{2}/400$ cycle/m, the admittance is large. So, unlike in section 4.2, there is no need to remove short wavelengths. At long wavelengths,

however, the admittance is small, which means that the gravity gradients are not sensitive to the seafloor topography at long wavelengths. As a result, the VGG data are only used to estimate the spectrum between 0.4 km to 5 km wavelengths of the local topography. Wavelengths longer than 5 km are obtained by low-pass filtering the ship soundings. The 5 km cut-off wavelength is empirically chosen based on the theoretical gravity gradient admittance shown in Figure 5.4.

5.2.2 Data Preparation

The vertical gravity gradients used in the estimation are shown in Figure 5.5.

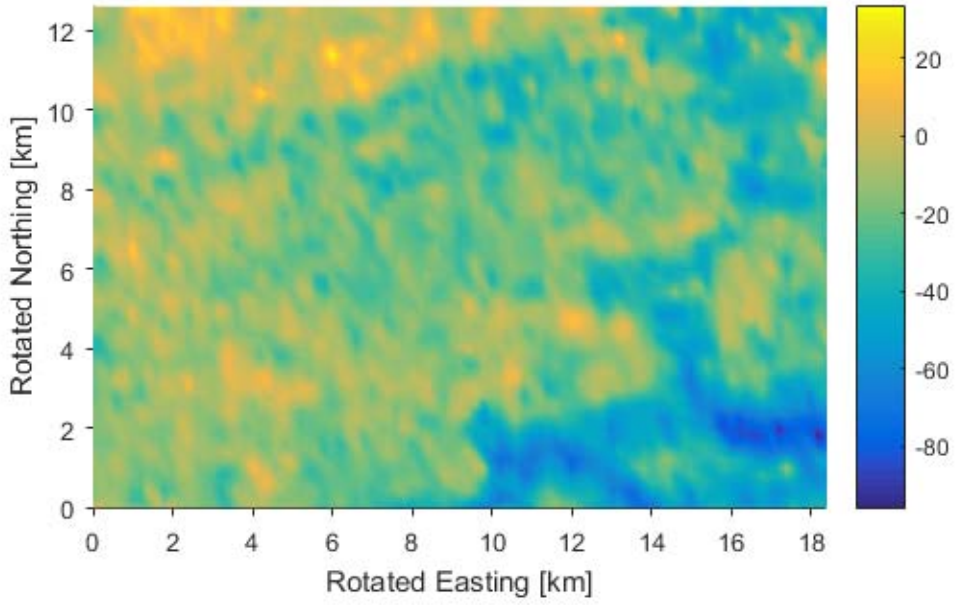

Figure 5.5: The 200 m × 200 m vertical gravity gradients of the study area in St. George's Bay. The units are Eötvös.

Parker's method needs ship soundings to compute the topography-to-gradient admittance scale and to obtain the long wavelength topography. The single-beam bathymetric depths that were downloaded from NCEI are very sparse in the study area. The multi-beam bathymetric depths are densely distributed, but are reserved for accuracy tests and not used in the estimation.

Consequently, the 10 m × 10 m multi-beam bathymetric depths were resampled to a 2.4 km × 2.4 km grid, and treated as simulated ship soundings.

A 200 m × 200 m topography grid was interpolated from the simulated ship soundings (the 2.4 km × 2.4 km grid) using the biharmonic spline interpolation method in preparation for the computation of the long-wavelength regional topography and the topography-to-gradient admittance scale; see Figure 5.6.

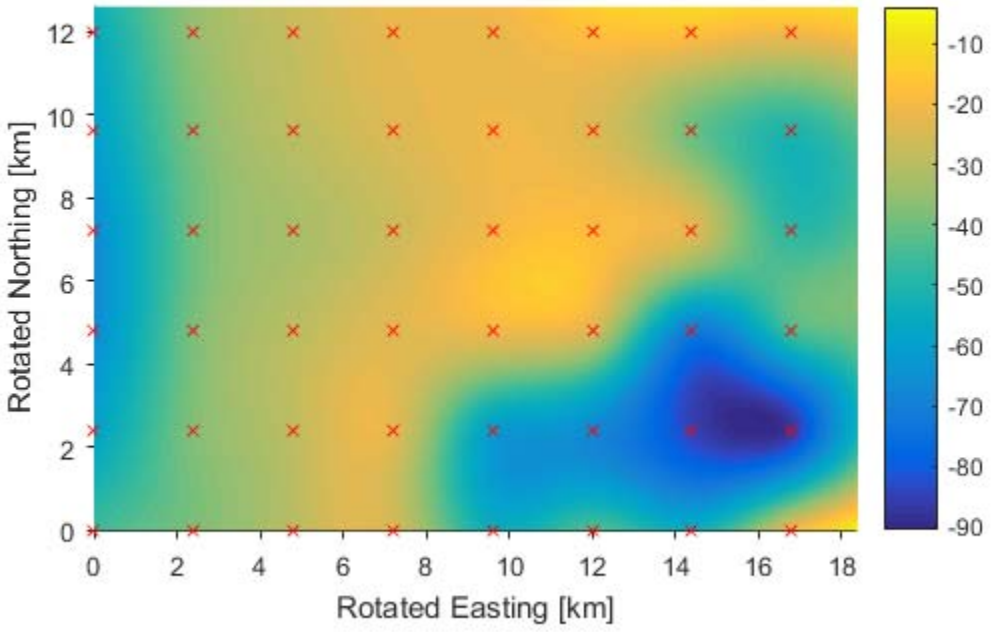

Figure 5.6: The 200 m by 200 m seafloor depth interpolated from simulated ship soundings. The simulated ship soundings are obtained by resampling the multi-beam bathymetric depths, and are marked by red crosses. The units of the color bar are meter.

5.2.3 Data Filtering

The Gaussian low-pass filter

$$W_l = e^{-2\times\left(936.9531\pi\overline{f}\right)^2} \tag{5.1}$$

was applied to the interpolated values shown in Figure 5.6 in order to obtain the long-wavelength seafloor topography Figure 5.7. $W_l = 0.5$ when $\overline{f} = 1/5000$ cycle/m.

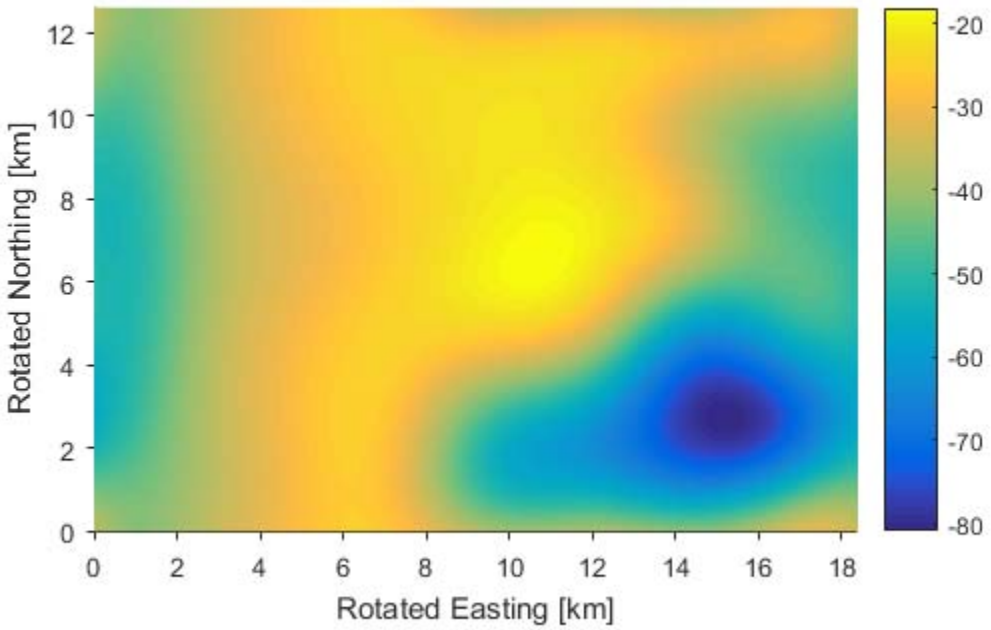

Figure 5.7: The long-wavelength depth obtained by low-pass filtering the simulated ship soundings. The units are meter.

To compute the topography-to-gradient admittance scale, the high-pass filter $W_h = 1 - W_l$ was applied to the interpolated depths in Figure 5.6 to obtain the 0.4-5 km wavelength local topography. The vertical gravity gradients in Figure 5.5 were multiplied by $\left(2\pi \bar{f}\right)^{-1} e^{2\pi \bar{f} d}$ in the frequency domain to obtain the equivalent gravity anomalies, and were then filtered using the same high-pass filter. Note that Parker's formulation requires all the gravity gradients to be measured on the same plane. The actual flight altitude over the study area ranges from 65.2 m to 244.5 m, with an average value of 86.8 m. In this analysis, this trajectory fluctuation is ignored. The scatter plot of local topography versus local equivalent gravity anomaly is shown in Figure 5.8. The topography-to-gradient admittance scale computed through formula (4.5) is $S = 1.1479e-4$.

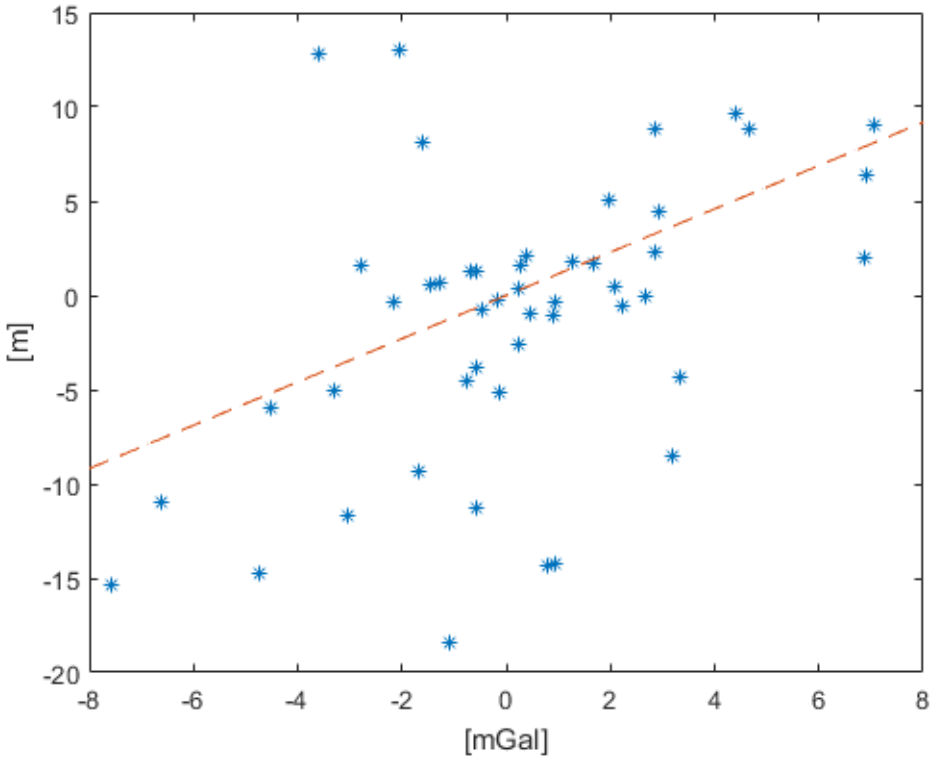

Figure 5.8: Local topography versus local equivalent gravity anomalies at places constrained by ship soundings, which are marked by red crosses in Figure 5.6.

Figure 5.8 shows that the local topography is only vaguely proportional to the local equivalent gravity anomalies. The correlation coefficient between them, computed according to (4.4), is only 0.4528. This is mainly due to the presumed large sub-surface density anomalies, as summarized in the last section.

5.2.4 Results

Since the linear model assumed in Parker's method does not seem to hold well in this case, results are expected to be correspondingly poor. Nevertheless, an estimation of seafloor topography is made according to formula (3.3). That is, the high-pass filtered equivalent gravity anomalies are multiplied by the topography-to-gradient admittance scale, and then supplemented by the long-wavelength topography (Figure 5.7). The results are shown in Figure 5.9 and Figure 5.10. The RMS of the difference between the total seafloor topography estimation and the multi-beam implied topography is ±7.1 m.

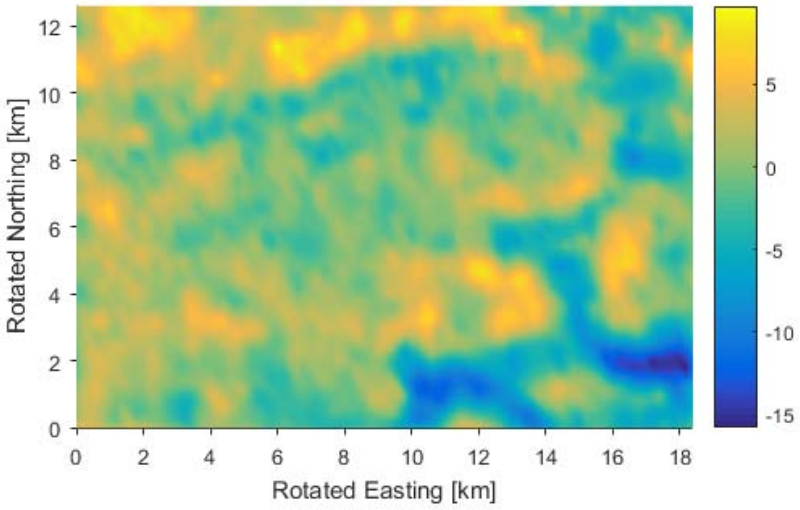

Figure 5.9: The short wavelength seafloor depths estimated from observed VGG according to formula (3.1). The units of the color bar are meter.

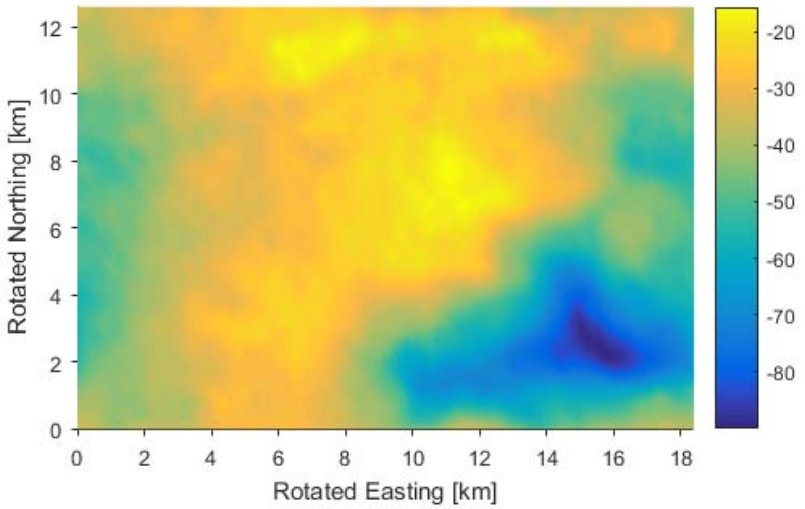

Figure 5.10: The total seafloor depths estimation. The units of the color bar are meter.

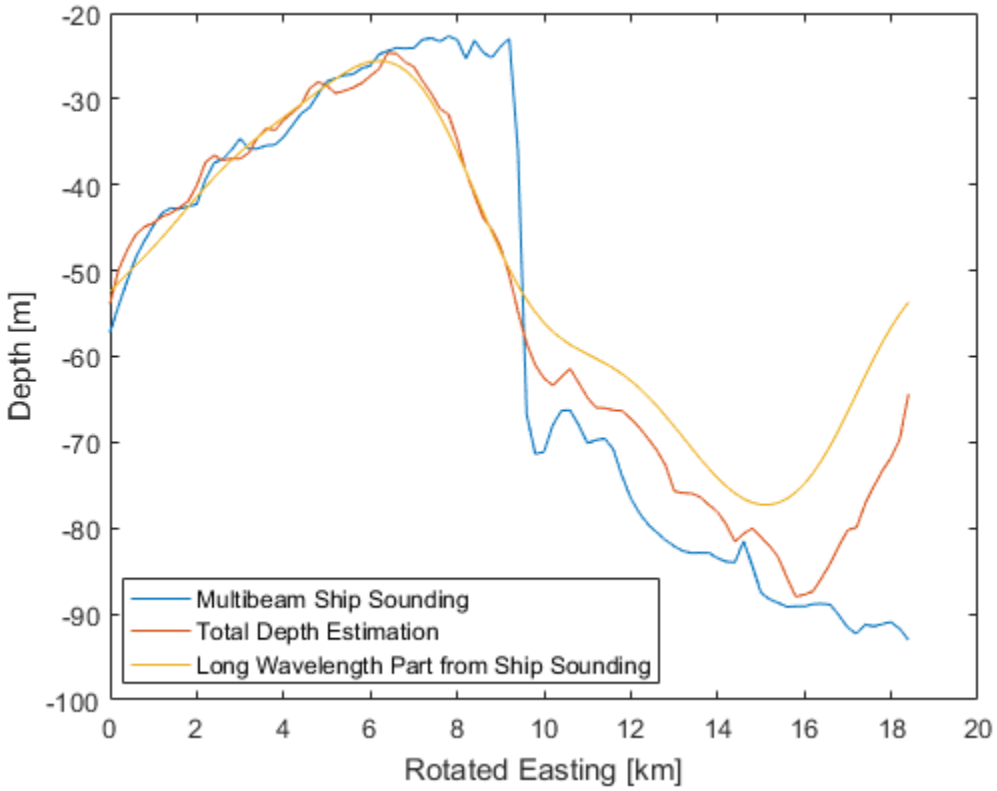

Figure 5.11: The profiles of the multibeam ship soundings, the depths estimated by using Parker's formulation, and the long-wavelength depths obtained by low-pass filtering the ship soundings, along the line where the rotated northing equals 2 km.

Figure 5.11 shows that, in general, the gradient-estimated topography improves the long-wavelength topography obtained from ship soundings. The estimations with respect to different long cut-off wavelength were computed. Table 5.1 shows that increasing the long cut-off wavelength in equation (5.1) to expand the wavelength band estimated from VGG decreases the estimation accuracy.

Table 5.1: Long cut-off wavelength versus the RMS of the difference between the total seafloor topography estimation and the multi-beam implied topography.

long cut-off wavelength [km]	RMS [m]
3	5.3
5	7.1
7	9.9
9	10.4

5.3 Estimation Using Simulated Annealing

5.3.1 Data Preparation and SA Configuration

The same VGG data as described in section 5.2, namely those seen in Figure 5.5, were used in the estimation by simulated annealing.

The X, Y coordinates of the 200 m × 200 m VGG grid were used to build the topography model by using adjacent right rectangular prisms. They serve as the X, Y coordinates of the prism center. Each face of the prism is parallel to one of the coordinate planes. The edge lengths of each prism along X and Y directions are both 200 m. The bottom boundary of the prism is the mean depth of the seafloor (38.56 m) over the study area, and the upper boundary is the topographic height. These topographic heights and one far zone topography effect parameter constitute the state vector to be estimated in the simulated annealing.

The truncation distance in the forward computation was set to 23 km. According to formula (2.66), the corresponding relative truncation error is 0.5 Eötvös, which means that the largest difference of the far zone topography effect between two points both in the study area is 0.5 Eötvös; this is one order of magnitude smaller than the accuracy of gradient observations. Thus, the topography model was extended by 23 km (115 grid nodes) from each of four sides to enable

the forward computation at the study area margin. The resolution of the extended topography is still 200 m by 200 m, and is interpolated from the 1′×1′ SIO global topography model version 18.1.

The upper and lower search limits of the seafloor topography were set to 20 m above and below the multi-beam bathymetric depths, respectively. The density of the seafloor topography was set to 2.2 g/cm^3. The search range for the far zone topography effect was set to [-20, 0] Eötvös. Other tuning parameters for the simulated annealing are listed in the Table 5.2.

Table 5.2: The tuning parameters.

T_0^i	n^i	m^i	D	Q
1	$\log(1e7)$	$-\log(1e-4500)$	5952	5952

5.3.2 Results

The SA program ran on the supercomputer Oakley at the Ohio Supercomputer Center, and exited after 1e7 iterations. The estimated seafloor topography is shown in Figures 5.12 and 5.13. The difference between the seafloor topography estimation and the multi-beam ship soundings was computed. The RMS of the difference is ±8.50 m.

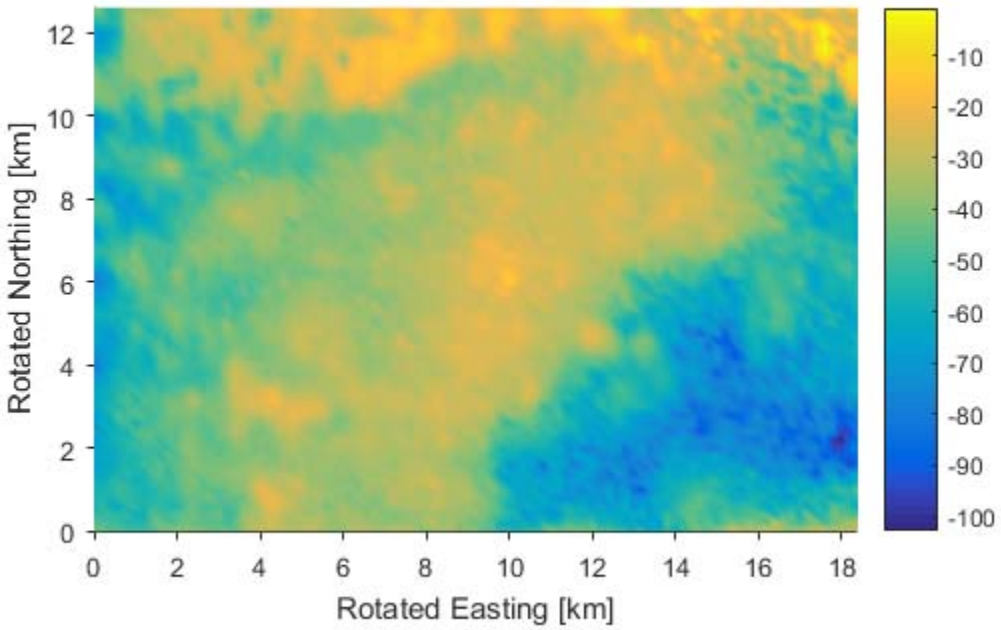

Figure 5.12: The seafloor depths estimated by using simulated annealing. The units of the color bar are meter.

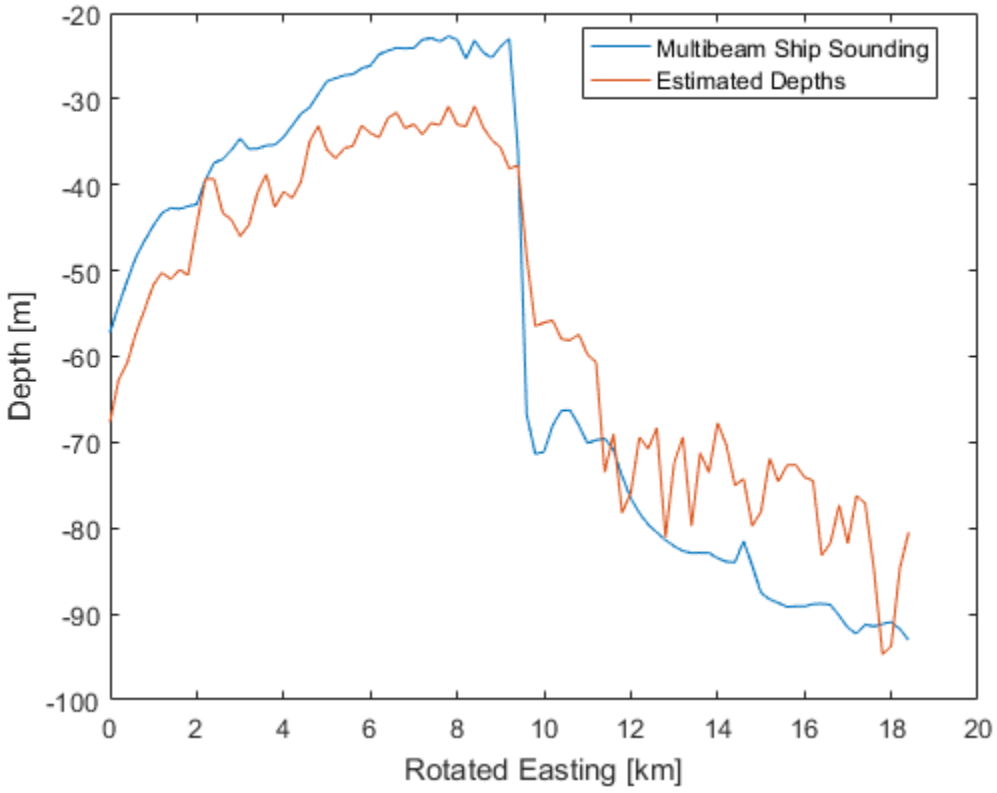

Figure 5.13: The profiles of the multibeam ship soundings and the SA estimated depths along the line where the rotated northing equals 2 km.

Although, in this experiment, the RMS of Parker's FFT-based method's topography estimation error is smaller than the RMS of that based on the SA method, one cannot conclude that Parker's method performs better. The Parker method seems to do well at long wavelengths due to reliance on truth data, while short wavelength features seem better approximated by SA, e.g., the sharp drop in topography at 9 km easting.

Chapter 6: Summary and Conclusions

Theoretical analysis showed that the gravity gradient is more sensitive to the short-wavelength topography than gravity anomaly. This research attempted to improve the current standard seafloor topography estimation methods by employing gravity gradients, removing the linear approximation in the modeled relationship between gravity and topography, and by incorporating the airborne gradiometry data whose spatial resolution is high.

The most widely used seafloor topography prediction method [*Smith and Sandwell*, 1994; 1997] was generalized to infer the topography from gravity gradients. Under the constant density assumption, the linear approximation of Parker's infinite series [*Parker*, 1973] and the regional isostatic compensation mechanism [*Watts*, 2001] were used to develop the gradient admittance that relates topography and gravity gradients in the spectral domain. The admittance function shows that the vertical gravity gradient is not sensitive to the long wavelength, due to using the derivative of gravity. The sensitivity is also limited at the very high frequencies due to downward continuation. Inversion at these spectral bands is therefore not stable and only an intermediate bandwidth of topography can be estimated from the gravity gradients. The long wavelengths must be computed from an existing model derived, e.g., from ship soundings.

The estimation based on Parker's method was tested in a 2°×2° area in the West Pacific Ocean using an estimation of the local admittance between topography and the gravity gradients. The gravity gradients are determined from satellite altimetry as a proxy for observed airborne gravity gradients that are as yet scarcely available in particular ocean areas where the density of the topography can be assumed uniform. Because they are not measured gradients, the prediction bandwidth is set to the same range as for the altimetry-derived gravity anomalies used for topography estimation by Smith and Sandwell.

Numerical analysis from this sample test showed that in rugged areas (topography ranges from -1000 m to -5000 m over a 200 km by 200 km rectangular area), the nonlinear terms of Parker's series are not negligible. This was supported by an algorithmic analysis of simulated topography using the radially symmetric coherency, which is a frequency-domain analogue of the correlation coefficient, and indicates how much of the observed gravity gradient is attributed to the linear part of the terrain effect. In the synthesized rugged area, the analysis shows that at short wavelengths, more than half of the implied vertical gravity gradient is from the nonlinear terrain effect if the density of the topography is assumed constant. This finding means that in rugged areas, the accuracy of the Fourier transform based method quickly decreases as the frequency

increases, no matter how accurate the gravity gradient measurement is and how high the resolution is. It strongly suggests that algorithms to remove the linear approximation should be developed in preparation for a more accurate and high resolution topography estimation capability.

To employ nonlinear terms in the estimation of seafloor topography from gravity gradients, a global optimization technique called simulated annealing (SA) was used, which can process nonlinear inverse problems. This method was also tested in the same 2°×2° area in the West Pacific Ocean using the same altimetry-derived gravity gradients. The seafloor topography parameters in a forward model were estimated through SA by minimizing the difference between the observed and forward-computed vertical gravity gradients. Two processing steps were found critical to achieve success. Padding (i.e., extending) the vicinity of the study area with a known topography model is needed to make the forward computation possible. Including sufficient extent of topography for the upward continuation in the forward model is necessary to ensure that the relative truncation error is below the level of observation noise, and thus enabling the modeling of the far zone effect as a constant.

The estimated topographies were compared with single beam bathymetric depths downloaded from NCEI. The RMS of the difference between them for the Fourier transform method is ±268 m. The RMS of the difference for the simulated annealing method is ±236 m, which is 12% smaller. It is also 22% smaller than that of the SIO's global topography model over the study area.

In principle, the simulated annealing is superior to the Fourier transform method by removing the linear approximation in the modeled relationship between topography and gravity gradient, which is extremely important in rugged areas. Although this also implies a tremendous increase in computational burden, the computing cost in the coming "big data" and "artificial intelligence" era is decreasing fast. It is worthwhile to trade computation costs for better accuracy and resolution in the estimation of seafloor topography. Another advantage of the simulated annealing technique is that it has no restrictions on data distribution, as required in Parker's infinite series model, thus enabling more flexibility in airborne gravity gradient trajectories.

The simulated annealing method developed in this research may be useful in updating the global seafloor topography. But this method, as well as the Fourier transform method, are limited to areas where sub-topography density can be assumed uniform. The existence of places where sub-surface geologic structures are complex and are the main source for gravity gradients impedes topography estimation from gravity gradients. This is demonstrated using airborne gravity gradients over St. George's Bay. Identifying this kind of area is an interesting topic for future research. Further investigations need to be performed to optimally combine different gravity gradient tensor elements or combine gravity gradient and gravity anomaly from independent sources. The purpose of the former is to increase the signal-to-noise ratio, and the objective of

the latter is to combine the superiorities of the gravity gradient and the gravity anomaly at different frequencies.

References

Abramowitz, M., and I. A. Stegun (1972), *Handbook of Mathematical Functions With Formulas, Graphs, and Mathematical Tables*.

Banks, R. J., R. L. Parker, and S. P. Huestis (1977), Isostatic compensation on a continental scale: local versus regional mechanisms, *Geophysical Journal of the Royal Astronomical Society*, *51*(2), 431-452, doi:10.1111/j.1365-246X.1977.tb06927.x.

Barnes, G., and J. Lumley (2011), Processing gravity gradient data, *Geophysics*, *76*(2), I33-I47, doi:10.1190/1.3548548.

Barthelmes, F. (2009), *Definition of functionals of the geopotential and their calculation from spherical harmonic models*, Helmholtz Centre Potsdam, GFZ GERMAN RESEARCH CENTRE FOR GEOSCIENCES, Potsdam, Germany, doi:10.2312/GFZ.b103-0902-26.

Bendat, J. S., and A. G. Piersol (1971), *Random Data Analysis and Measurement Procedures*, Wiley-Interscience, New York.

Bendat, J. S., and A. G. Piersol (2010), *Random Data: Analysis and Measurement Procedures*, Fourth Edition ed., Wiley, Hoboken, N.J.

Calmant, S. (1994), Seamount topography by least-squares inversion of altimetric geoid heights and shipborne profiles of bathymetry and/or gravity anomalies, *Geophys. J. Int.*, *119*(2), 428-452, doi:10.1111/j.1365-246X.1994.tb00133.x.

Calmant, S., M. Berge-Nguyen, and A. Cazenave (2002), Global seafloor topography from a least-squares inversion of altimetry-based high-resolution mean sea surface and shipboard soundings, *Geophys. J. Int.*, *151*(3), 795-808, doi:10.1046/j.1365-246X.2002.01802.x.

Carter, G. C., C. Knapp, and A. H. Nuttall (1973), Estimation of the magnitude-squared coherence function via overlapped fast Fourier transform processing, *Audio and Electroacoustics, IEEE Transactions on*, *21*(4), 337-344, doi:10.1109/TAU.1973.1162496.

Černý, V. (1985), Thermodynamical approach to the traveling salesman problem: An efficient simulation algorithm, *Journal of Optimization Theory and Applications*, *45*(1), 41-51, doi:10.1007/bf00940812.

Dixon, T. H., M. Naraghi, M. McNutt, and S. Smith (1983), Bathymetric prediction from Seasat altimeter data, *Journal of Geophysical Research: Oceans (1978–2012)*, *88*(C3), 1563-1571.

Dixon, T. H., and M. Parke (1983), Bathymetry estimates in the southern oceans from Seasat altimetry, *Nature*, *304*, 406-411.

Dransfield, M. (2007), Airborne gravity gradiometry in the search for mineral deposits, paper presented at Exploration 07, the Fifth Decennial International Conference on Mineral Exploration, Toronto, Canada.

Ernstsen, V. B., R. Noormets, D. Hebbeln, A. Bartholomä, and B. W. Flemming (2006), Precision of high-resolution multibeam echo sounding coupled with high-accuracy positioning in a shallow water coastal environment, *Geo-Marine Letters*, *26*(3), 141-149, doi:10.1007/s00367-006-0025-3.

Forsberg, R. (1985), Gravity field terrain effect computations by FFT, *Bulletin géodésique*, *59*(4), 342-360, doi:10.1007/bf02521068.

Forsberg, R., and S. Kenyon (1995), Downward continuation of airborne gravity data, *unpublished work*.

Garcia, E. S., D. T. Sandwell, and W. H. F. Smith (2014), Retracking CryoSat-2, Envisat and Jason-1 radar altimetry waveforms for improved gravity field recovery, *Geophys. J. Int.*, *196*(3), 1402-1422, doi:10.1093/gji/ggt469.

Griff, B. (1991), *Efficient generators in simulated annealing*, Center for Communications and Signal Processing, Department Electrical and Computer Engineering, North Carolina State University, Raleigh, NC, USA.

Hanssen, A. (1997), Multidimensional multitaper spectral estimation, *Signal Processing*, *58*(3), 327-332.

Harri, R., and K. Kimmo (1990), Image Deconvolution with Simulated Annealing Method, *Physica Scripta*, *1990*(T33), 126-130.

Hirt, C., and M. Kuhn (2012), Evaluation of high‐degree series expansions of the topographic potential to higher‐order powers, *Journal of Geophysical Research*, *117*(B12407), 1-12, doi:10.1029/2012JB009492.

Hofmann-Wellenhof, B., and H. Moritz (2005), *Physical Geodesy*, Second, corrected ed., SpringerWienNewYork, Austria.

Hsiao, Y.-S., J. W. Kim, K. B. Kim, B. Y. Lee, and C.-W. Hwang (2011), Bathymetry Estimation Using the Gravity-Geologic Method: An Investigation of Density Contrast Predicted by the Downward Continuation Method, *Terrestrial, Atmospheric and Oceanic Sciences*, *22*(3), 347-358.

Hu, M., J. Li, H. Li, C. Shen, and L. Xing (2014a), A program for bathymetry prediction from vertical gravity gradient anomalies and ship soundings, *Arabian Journal of Geosciences*, 1-7, doi:10.1007/s12517-014-1570-0.

Hu, M., J. Li, H. Li, and L. Xing (2014b), Bathymetry predicted from vertical gravity gradient anomalies and ship soundings, *Geodesy and Geodynamics*, *5*(1), 41-46.

Hwang, C. W., J. Y. Guo, X. L. Deng, H. Y. Hsu, and Y. T. Liu (2006), Coastal gravity anomalies from retracked Geosat/GM altimetry: Improvement, limitation and the role of airborne gravity data, *J. Geodesy*, *80*(4), 204-216, doi:10.1007/s00190-006-0052-x.

Ingber, L. (1989), Very Fast Simulated Re-annealing, *Mathematical and Computer Modelling*, *12*(8), 967-973.

Ingber, L. (1993), Simulated Annealing: Practice versus Theory, *Mathematical and Computer Modelling*, *18*(11), 29-57.

Ingber, L. (1996), Adaptive Simulated Annealing (ASA): Lessons Learned, *Control and Cybernetics*, *25*, 33-54.

Ingber, L., and B. Rosen (1992), Genetic Algorithms and Very Fast Simulated Reannealing - A Comparison, *Mathematical and Computer Modelling*, *16*(11), 87-100, doi:10.1016/0895-7177(92)90108-w.

International Hydrographic Organization (2008), *IHO Standards for Hydrographic Surveys*, International Hydrographic Bureau, Monaco.

Jekeli, C. (2010), Correlation Modeling of the Gravity Field in Classical Geodesy, in *Handbook of Geomathematics*, edited by W. Freeden, M. Z. Nashed and T. Sonar, pp. 833-863, Springer Berlin Heidelberg, doi:10.1007/978-3-642-01546-5_28.

Jekeli, C. (2013a), Extent and resolution requirements for the residual terrain effect in gravity gradiometry, *Geophys. J. Int.*, *195*(1), 211-221, doi:10.1093/gji/ggt246.

Jekeli, C. (2013b), *Fourier Geodesy, Class Notes for GS7875*, School of Earth Sciences, The Ohio State University, Columbus, Ohio, USA.

Jekeli, C. (2017), *Spectral Methods in Geodesy and Geophysics*, CRC Press.

Jena, B., P. J. Kurian, D. Swain, A. Tyagi, and R. Ravindra (2012), Prediction of bathymetry from satellite altimeter based gravity in the Arabian Sea: Mapping of two unnamed deep seamounts, *Int. J. Appl. Earth Obs. Geoinf.*, *16*, 1-4, doi:10.1016/j.jag.2011.11.008.

Kim, J. W., R. R. von Frese, B. Y. Lee, D. R. Roman, and S.-J. Doh (2010a), Altimetry-derived gravity predictions of bathymetry by the gravity-geologic method, *PAGEOPH*, *168*(5), 815-826.

Kim, K. B., Y. S. Hsiao, J. W. Kim, B. Y. Lee, Y. K. Kwon, and C. H. Kim (2010b), Bathymetry enhancement by altimetry-derived gravity anomalies in the East Sea (Sea of Japan), *Mar. Geophys. Res.*, *31*(4), 285-298, doi:10.1007/s11001-010-9110-0.

Kirkpatrick, S., C. D. Gelatt, and M. P. Vecchi (1983), Optimization by Simulated Annealing, *Science*, *220*(4598), 671-680, doi:10.1126/science.220.4598.671.

Laarhoven, P. J. M., and E. H. L. Aarts (1987), *Simulated Annealing: Theory and Applications*, 7-15 pp., Springer Netherlands, Dordrecht, doi:10.1007/978-94-015-7744-1_2.

Lewis, B. T., and L. M. Dorman (1970), Experimental isostasy: 2. An isostatic model for the USA derived from gravity and topographic data, *Journal of Geophysical Research*, *75*(17), 3367-3386.

Li, L., and G. Ma (2014), The inversion of seabed terrain of the South China Sea by simulated annealing based on gravity gradient data, *Progress in Geophysics*, *29*(2), 931-935, doi:10.6038/pg20140261.

Lindberg, C. R., and J. Park (1987), Multiple-taper spectral analysis of terrestrial free oscillations: part II, *Geophys. J. Int.*, *91*(3), 795-836, doi:10.1111/j.1365-246X.1987.tb01669.x.

Liu, J. S., A. J. Caley, A. J. Waddie, and M. R. Taghizadeh (2008), Comparison of simulated quenching algorithms for design of diffractive optical elements, *Applied Optics*, *47*(6), 807-816, doi:10.1364/ao.47.000807.

Marks, K. M. (1996), Resolution of the Scripps/NOAA marine gravity field from satellite altimetry, *Geophys. Res. Lett.*, *23*(16), 2069-2072, doi:10.1029/96gl02059.

Marks, K. M., and W. H. F. Smith (2006), An evaluation of publicly available global bathymetry grids, *Mar. Geophys. Res.*, *27*(1), 19-34, doi:10.1007/s11001-005-2095-4.

Marks, K. M., and W. H. F. Smith (2012), Radially symmetric coherence between satellite gravity and multibeam bathymetry grids, *Marine Geophysical Research*, *33*(3), 223-227.

Marks, K. M., W. H. F. Smith, and D. T. Sandwell (2010), Evolution of errors in the altimetric bathymetry model used by Google Earth and GEBCO, *Marine Geophysical Research*, *31*(3), 223-238, doi:10.1007/s11001-010-9102-0.

McKenzie, D. P., and C. Bowin (1976), The relationship between bathymetry and gravity in the Atlantic Ocean, *Journal of Geophysical Research*, *81*(11), 1903-1915, doi:10.1029/JB081i011p01903.

McNutt, M. (1979), Compensation of oceanic topography: An Application of the Response Function Technique to the Surveyor area, *Journal of Geophysical Research: Solid Earth*, *84*(B13), 7589-7598, doi:10.1029/JB084iB13p07589.

Metropolis, N., A. W. Rosenbluth, M. N. Rosenbluth, A. H. Teller, and E. Teller (1953), Equation of State Calculations by Fast Computing Machines, *The Journal of Chemical Physics*, *21*(6), 1087-1092, doi:10.1063/1.1699114.

Murphy, C., J. Dickinson, and A. Salem (2012), Depth estimating Full Tensor Gravity data with the Adaptive Tilt Angle method, *ASEG Extended Abstracts*, *2012*(1), 1-3.

Nettleton, L. (1939), Determination of density for reduction of gravimeter observations, *Geophysics*, *4*(3), 176-183.

Ouyang, M. D., Z. M. Sun, and Z. H. Zhai (2014), Predicting bathymetry in South China Sea using the gravity-geologic method, *Chinese J. Geophys.-Chinese Ed.*, *57*(9), 2756-2765, doi:10.6038/cjg20140903.

Park, J., C. R. Lindberg, and D. J. Thomson (1987a), Multiple-taper spectral analysis of terrestrial free oscillations: part I, *Geophys. J. Int.*, *91*(3), 755-794, doi:10.1111/j.1365-246X.1987.tb01668.x.

Park, J., C. R. Lindberg, and F. L. Vernon (1987b), Multitaper spectral analysis of high-frequency seismograms, *Journal of Geophysical Research: Solid Earth*, *92*(B12), 12675-12684, doi:10.1029/JB092iB12p12675.

Parker, R. L. (1973), The Rapid Calculation of Potential Anomalies, *Geophysical Journal of the Royal Astronomical Society*, *31*(4), 447-455, doi:10.1111/j.1365-246X.1973.tb06513.x.

Pavlis, N. K., S. A. Holmes, S. C. Kenyon, and J. K. Factor (2012), The development and evaluation of the Earth Gravitational Model 2008 (EGM2008), *Journal of Geophysical Research: Solid Earth (1978–2012)*, *117*(B4).

Ramillien, G., and I. C. Wright (2000), Predicted seafloor topography of the New Zealand region: A nonlinear least squares inversion of satellite altimetry data, *J. Geophys. Res.-Solid Earth*, *105*(B7), 16577-16590, doi:10.1029/2000jb900099.

Raney, R. K., W. H. F. Smith, D. T. Sandwell, J. R. Jensen, D. L. Porter, and E. Reynolds (2003), Abyss-Lite: improved bathymetry from a dedicated small satellite delay-Doppler radar altimeter, paper presented at the Geoscience and Remote Sensing Symposium, 2003. IGARSS '03. Proceedings. 2003 IEEE International, 21-25 July 2003.

Ribe, N. M. (1982), On the interpretation of frequency response functions for oceanic gravity and bathymetry, *Geophysical Journal of the Royal Astronomical Society*, *70*(2), 273-294, doi:10.1111/j.1365-246X.1982.tb04968.x.

Rousseeuw, P. J., and A. M. Leroy (2005), *Robust Regression and Outlier Detection*, John Wiley & Sons, Inc., Published Online, doi:10.1002/0471725382.

Roy, L., M. K. Sen, D. D. Blankenship, P. L. Stoffa, and T. G. Richter (2005), Inversion and uncertainty estimation of gravity data using simulated annealing: An application over Lake Vostok, East Antarctica, *Geophysics*, *70*(1), J1-J12, doi:10.1190/1.1852777.

Rummel, R., and R. H. N. Haagmans (1990), Gravity gradients from satellite altimetry, *Mar. Geod.*, *14*(1), 1-12, doi:10.1080/15210609009379641.

Sailor, R. V., and E. A. Okal (1983), Applications of SEASAT Altimeter Data in Seismotectonic Studies of the South-Central Pacific, *Journal of Geophysical Research-Oceans*, *88*(NC3), 1572-1580, doi:10.1029/JC088iC03p01572.

Sandwell, D. T. (1987), Biharmonic spline interpolation of GEOS-3 and SEASAT altimeter data, *Geophys. Res. Lett.*, *14*(2), 139-142, doi:10.1029/GL014i002p00139.

Sandwell, D. T., E. Garcia, K. Soofi, P. Wessel, M. Chandler, and W. H. F. Smith (2013), Toward 1-mGal accuracy in global marine gravity from CryoSat-2, Envisat, and Jason-1, *The Leading Edge*, *32*(8), 892-899, doi:10.1190/tle32080892.1.

Sandwell, D. T., and D. C. McAdoo (1990), High-Accuracy, High-Resolution Gravity Profiles From 2 Years of the Geosat Exact Repeat Mission, *Journal of Geophysical Research-Oceans*, *95*(C3), 3049-3060, doi:10.1029/JC095iC03p03049.

Sandwell, D. T., R. D. Müller, W. H. F. Smith, E. Garcia, and R. Francis (2014), New global marine gravity model from CryoSat-2 and Jason-1 reveals buried tectonic structure, *Science*, *346*(6205), 65-67, doi:10.1126/science.1258213.

Sandwell, D. T., and W. H. F. Smith (1992), Global marine gravity from ERS-1, Geosat and Seasat reveals new tectonic fabric, *Eos Transactions of the American Geophysical Union*, *73*(43), 133, doi:10.1029/91EO10347.

Sandwell, D. T., and W. H. F. Smith (1997), Marine gravity anomaly from Geosat and ERS 1 satellite altimetry, *Journal of Geophysical Research: Solid Earth*, *102*(B5), 10039-10054, doi:10.1029/96JB03223.

Sandwell, D. T., W. H. F. Smith, S. Gille, E. Kappel, S. Jayne, K. Soofi, B. Coakley, and L. Geli (2006), Bathymetry from space: Rationale and requirements for a new, high-resolution altimetric mission, *C. R. Geosci.*, *338*(14-15), 1049-1062, doi:10.1016/j.crte.2006.05.014.

Selman, D. (2013), *Final Report of Processing and Acquisition of Air-FTG® Data and Magnetics in Bay St. George, Newfoundland/Labrador for Natural Resources Canada*, Bell Geospace Inc., Houston, TX.

Shaw, J., and R. C. Courtney (1997), Multibeam bathymetry of glaciated terrain off southwest Newfoundland, *Marine Geology*, *143*(1–4), 125-135, doi:10.1016/S0025-3227(97)00093-5.

Shum, C. K., P. A. M. Abusali, C.-Y. Kuo, H. Lee, J. Ogle, R. K. Raney, J. C. Ries, W. H. F. Smith, D. Svehla, and C. Zhao (2009), Orbit Accuracy Requirement for ABYSS: The Space Station Radar Altimeter to Map Global Bathymetry, *Geoscience and Remote Sensing Letters, IEEE*, *6*(4), 653-657, doi:10.1109/LGRS.2009.2012877.

Simons, F. J., M. T. Zuber, and J. Korenaga (2000), Isostatic response of the Australian lithosphere: Estimation of effective elastic thickness and anisotropy using multitaper spectral analysis, *Journal of Geophysical Research: Solid Earth*, *105*(B8), 19163-19184, doi:10.1029/2000JB900157.

Slepian, D. (1978), Prolate spheroidal wave functions, fourier analysis, and uncertainty - V: the discrete case, *Bell System Technical Journal, The*, *57*(5), 1371-1430, doi:10.1002/j.1538-7305.1978.tb02104.x.

Smith, W. H. F. (1993), On the accuracy of digital bathymetric data, *Journal of Geophysical Research: Solid Earth (1978–2012)*, *98*(B6), 9591-9603.

Smith, W. H. F., and D. T. Sandwell (1994), Bathymetric prediction from dense satellite altimetry and sparse shipboard bathymetry, *Journal of Geophysical Research: Solid Earth (1978–2012)*, *99*(B11), 21803-21824.

Smith, W. H. F., and D. T. Sandwell (1997), Global sea floor topography from satellite altimetry and ship depth soundings, *Science*, *277*(5334), 1956-1962.

Smith, W. H. F., and D. T. Sandwell (2004), Conventional bathymetry, bathymetry from space, and geodetic altimetry, *OCEANOGRAPHY-WASHINGTON DC-OCEANOGRAPHY SOCIETY-*, *17*(1), 8-23.

Smith, W. H. F., D. T. Sandwell, and R. K. Raney (2005), Bathymetry from satellite altimetry: Present and future, paper presented at Proceedings of OCEANS 2005 MTS/IEEE, New York, 17-23 Sept. 2005.

Szu, H., and R. Hartley (1987), Fast simulated annealing, *Phys. Lett. A*, *122*(3), 157-162, doi:10.1016/0375-9601(87)90796-1.

Tapley, M. B. (1997), Evaluation of flat-earth approximation results for geopotential missions, *J. Guid. Control Dyn.*, *20*(2), 246-252, doi:10.2514/2.4059.

Thomson, D. J. (1982), Spectrum estimation and harmonic analysis, *Proceedings of the IEEE*, *70*(9), 1055-1096, doi:10.1109/PROC.1982.12433.

Uzun, S. (2013), Estimating Parameters of Subsurface Structures from Airborne Gravity Gradiometry Data Using a Monte-Carlo Optimization Method, Ph.D. thesis, School of Earth Sciences, The Ohio State University, Columbus, Ohio, USA.

Wang, Y. M. (2000), Predicting Bathymetry from the Earth's Gravity Gradient Anomalies, *Mar. Geod.*, *23*(4), 251-258, doi:10.1080/01490410050210508.

Watts, A. B. (1978), An analysis of isostasy in the world's oceans 1. Hawaiian-Emperor Seamount Chain, *Journal of Geophysical Research: Solid Earth*, *83*(B12), 5989-6004, doi:10.1029/JB083iB12p05989.

Watts, A. B. (2001), *Isostasy and Flexure of the Lithosphere*, Cambridge University Press.

Weatherall, P., K. M. Marks, M. Jakobsson, T. Schmitt, S. Tani, J. E. Arndt, M. Rovere, D. Chayes, V. Ferrini, and R. Wigley (2015), A new digital bathymetric model of the world's oceans, *Earth and Space Science*, *2*(8), 331-345, doi:10.1002/2015EA000107.

Welch, P. D. (1967), The use of fast Fourier transform for the estimation of power spectra: A method based on time averaging over short, modified periodograms, *Audio and Electroacoustics, IEEE Transactions on*, *15*(2), 70-73, doi:10.1109/TAU.1967.1161901.

White, J. V., R. V. Sailor, A. R. Lazarewicz, and A. R. Leschack (1983), Detection of Seamount Signatures in SEASAT Altimeter Data Using Matched Filters, *Journal of Geophysical Research-Oceans*, *88*(NC3), 1541-1551, doi:10.1029/JC088iC03p01541.

Wiener, N. (1949), *Extrapolation, Interpolation, and Smoothing of Stationary Time Series*, MIT Press Cambridge, MA.

Wingham, D. J., C. R. Francis, S. Baker, C. Bouzinac, D. Brockley, R. Cullen, P. de Chateau-Thierry, S.W. Laxon, U. Mallow, C. Mavrocordatos, L. Phalippou, G. Ratier, L. Rey, F. Rostan, P. Viau, D. W. Wallis (2006), CryoSat: A mission to determine the fluctuations in Earth's land and marine ice fields, *Adv. Space Res.*, *37*(4), 841-871, doi:dx.doi.org/10.1016/j.asr.2005.07.027.

Zhu, L. (2007), Gradient Modeling with Gravity and DEM, Ph.D. thesis, School of Earth Sciences, The Ohio State University, Columbus, Ohio, USA.

Appendix A: Thomson's Multiple-Slepian-Taper method

Thomson [1982] windows one realization of random process by several orthogonal tapers $u_j(x_l)$ and uses these windowed data to calculate uncorrelated periodogram $\hat{\Theta}_{\Gamma b}^{j}(f_k)$ according to (3.20). The weighted average of $\hat{\Theta}_{\Gamma b}^{j}(f_k)$ reduces the estimation variance and gives the final estimation of the PSD (equation [9] in [*Park et al.*, 1987b]).

$$\hat{\Theta}_{\Gamma b}(f_k) = \frac{1}{M}\sum_{j=1}^{M} \lambda_j \hat{\Theta}_{\Gamma b}^{j}(f_k) \tag{A.1}$$

where λ_j are weights, M is the number of tapers used, and $\hat{\Theta}_{\Gamma b}^{j}(f_k)$ is given by

$$\hat{\Theta}_{\Gamma b}^{j}(f_k) = \frac{1}{T}\left(\mathcal{F}\left(u_j \Gamma_T(x_l)\right)\right)^{*} \mathcal{F}\left(u_j b_T(x_l)\right) \tag{A.2}$$

That is, if the periodograms are uncorrelated and their variances are same, after averaging the variance of the final PSD estimation is reduced by $\frac{1}{M}$.

When we use only a finite extent of a signal to determine the spectrum of the entire signal, the spectrum of the signal at a particular frequency leaks into neighboring parts of the spectrum. Usually a window is adopted to reduce the spectral leakage. According to different minimization criteria we could find different windows. *Slepian* [1978] builds an ideal taper set from discrete prolate spheroidal sequences (dpss) using the energy concentration criterion,

$$\frac{\int_{-W}^{W}\left(\mathcal{F}\left(u_j\right)\right)^{*}\mathcal{F}\left(u_j\right)df}{\int_{-f_N}^{f_N}\left(\mathcal{F}\left(u_j\right)\right)^{*}\mathcal{F}\left(u_j\right)df} = \max \tag{A.3}$$

where $f_N = \frac{1}{2\Delta x}$ is the Nyquist frequency, and $W < f_N$ is the bandwidth we designate.

Criterion (A.3) means that this taper concentrates most of its energy in the frequency interval $[-W, W]$. W measures the resolution of the estimates, and is usually chosen as a small integer multiple of the fundamental frequency $\frac{1}{N\Delta x}$ [*Simons et al.*, 2000]. The tapers built by this criterion are solutions to an eigenvector problem (A.4) [*Lindberg and Park*, 1987; *Park et al.*, 1987a].

$$\mathbf{C}\mathbf{u}_j = \lambda_j \mathbf{u}_j \tag{A.4}$$

The elements of $\mathbf{C}$ are:

$$C_{ij} = \begin{cases} \dfrac{\sin\left(2\pi W \Delta x (i-j)\right)}{\pi (i-j)} & i \neq j \\ 2W\Delta x & i = j \end{cases} \tag{A.5}$$

where $i, j = 0, 1, \cdots, N$. As a result, they are orthogonal and the resulting periodogram $\hat{\Theta}^j_{\Gamma b}(f_k)$ of the windowed data are uncorrelated. The corresponding eigenvalues are the frequency domain energy concentration ratios in (A.3), and serve as the weights in formula (A.1). The larger the eigenvalue, the less energy in the side lobe of the taper spectrum, see Figure A 3.

For a chosen W, there are $2NW\Delta x$ useful tapers. Usually only the first $M = 2NW\Delta x - 1$ tapers are used to build the uncorrelated periodogram. The corresponding eigenvalues of these M tappers approximate one. When the order of the taper increases beyond $2NW\Delta x$, the corresponding eigenvalues decrease sharply to zero (see Figure A 2). Although larger W builds more useful tapers and thus makes the variance of the final PSD estimation smaller, the resolution decays, see Figure A 4. So the selection of W is a trade-off between estimate variance and resolution.

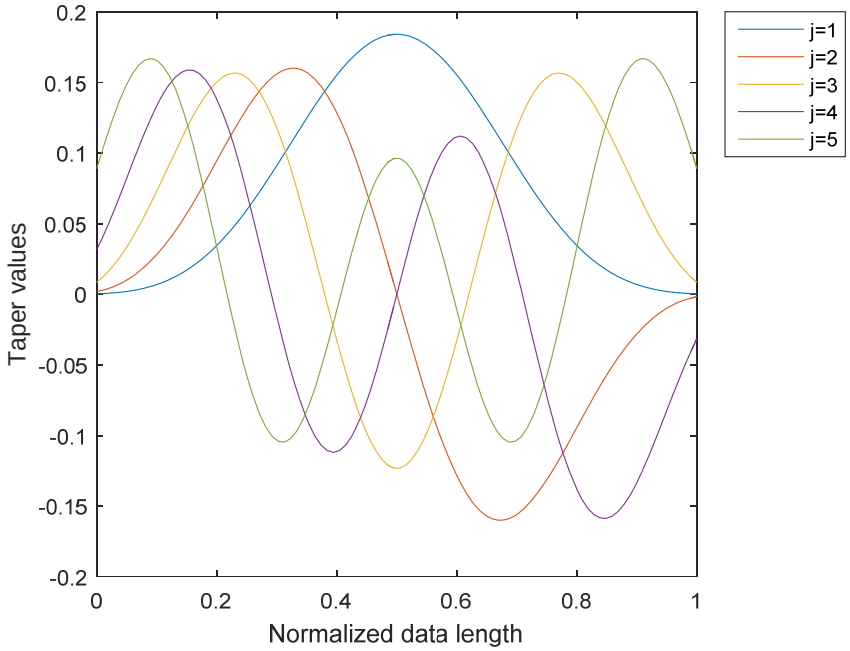

Figure A 1: Windowing tapers $u_j(x)$ for data length $N=100$, $NW\Delta x=3$, $j=1,2,\cdots,2NW\Delta x-1$.

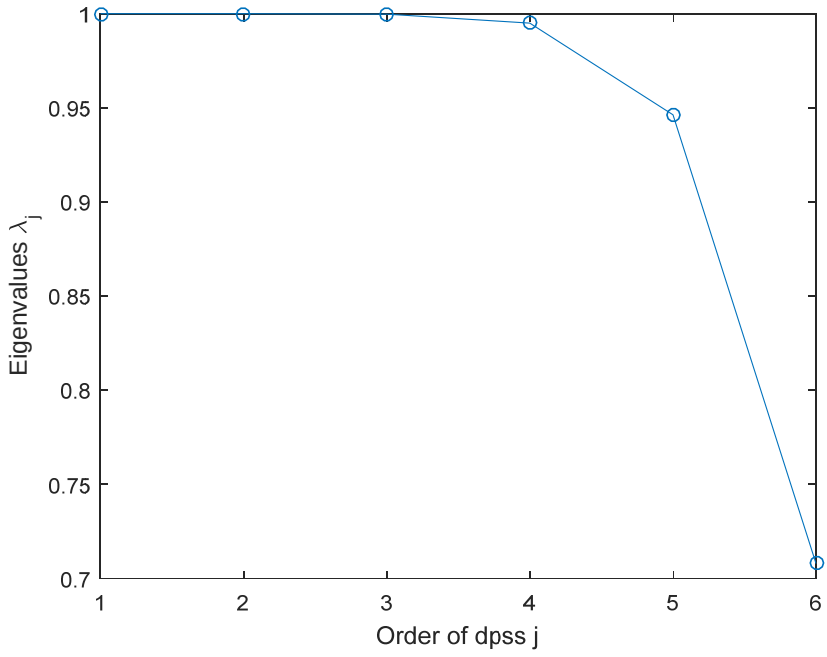

Figure A 2: Eigenvalues λ_j versus corresponding order of dpss tapers.

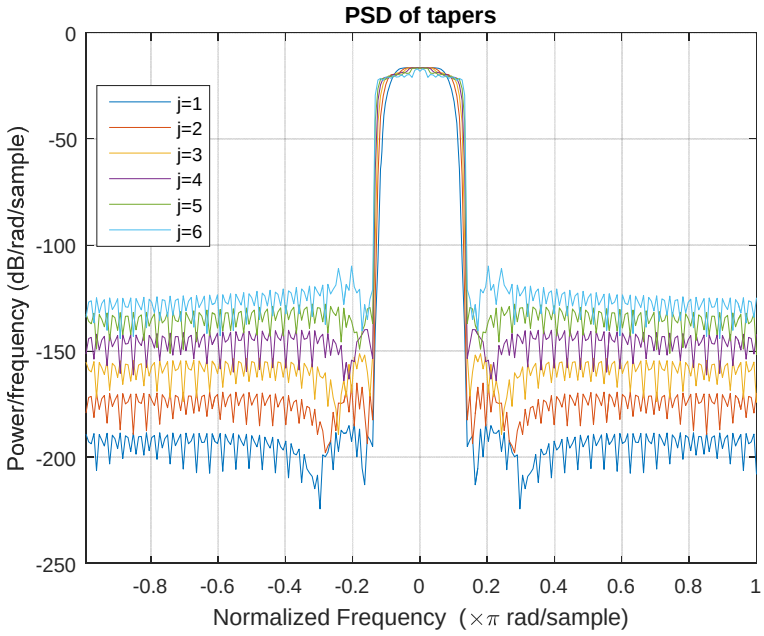

Figure A 3: The power spectral density of each taper.

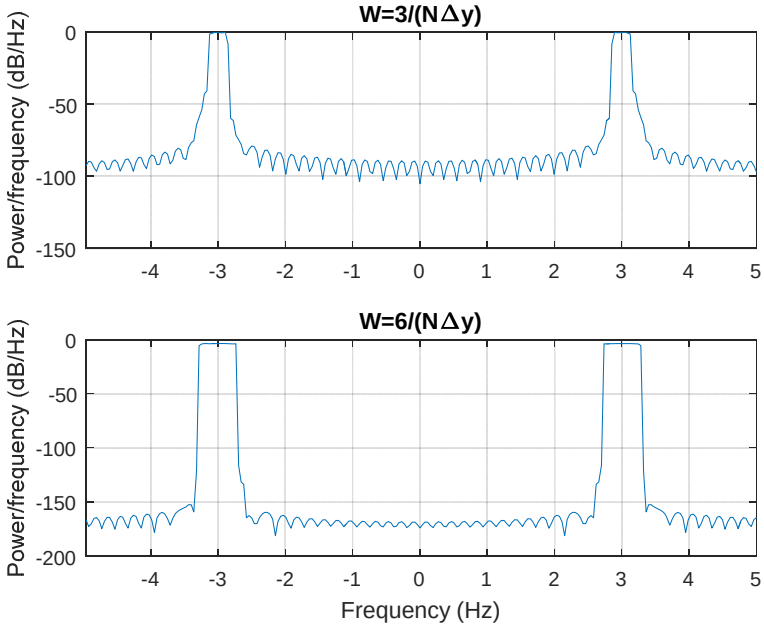

Figure A 4: The Thomson multitaper power spectral densities of data sampled from $y=\cos(6\pi x)$ between -10 and 9.9 with interval 0.1. The upper PSD is calculated with $NW\Delta x=3$ while the lower PSD calculated with $NW\Delta x=6$. Both calculations pick up the correct frequency 3, but with larger W value, the resolution decays.

Generalizing to two dimensional PSD estimation is straight forward and has been discussed in [*Hanssen*, 1997]. Let us denote the data as a $N_1 \times N_2$ matrix. Choosing two parameters W_1, W_2 one could build two one dimensional taper sets $\mathbf{u}_i^1$ and $\mathbf{u}_j^2$. The two-dimensional tapper is simply the outer product of these two 1-D tapers.

$$\mathbf{u}_{i,j} = \mathbf{u}_i^1 \left(\mathbf{u}_j^2\right)^T \tag{A.6}$$

The corresponding weight $\lambda_{i,j}$ is the product of the eigenvalues of the two 1-D tapers.

$$\lambda_{i,j} = \lambda_i \cdot \lambda_j \tag{A.7}$$

By doing so, a total of $\left(2N_1W_1\Delta x_1 - 1\right)\left(2N_2W_2\Delta x_2 - 1\right)$ tapers are built. Windowing the data with these tapers and average the direct PSD gives the final PSD estimation. The units of the two-dimensional cross-PSD is $Eötvös \cdot m / \left(cycle / m\right)^2$.

Appendix B: The Spherical Harmonics of the Gravity Anomaly

Equation (B.1) is the formula to compute the gravitational potential using the EGM2008 model.

$$V\left(r,\theta,\lambda\right)=\frac{GM}{r}\left[1+\sum_{n=2}^{N\max}\left(\frac{a}{r}\right)^{n}\sum_{m=0}^{n}\left(\overline{C}_{n,m}\cos m\lambda+\overline{S}_{n,m}\sin m\lambda\right)\overline{P}_{n,m}\left(\cos\theta\right)\right] \quad \text{(B.1)}$$

where GM is the geocentric gravitational constant, a is a scaling factor, $\overline{C}_{n,m}$ and $\overline{S}_{n,m}$ are the spherical harmonic coefficients given in the EGM2008 model.

The normal gravitational potential in spherical harmonics is [*Hofmann-Wellenhof and Moritz*, 2005]:

$$V'=\frac{GM}{r}\left[1+\sum_{k=1}^{\infty}\overline{C}_{2k,0}^{V'}\left(\frac{a_l}{r}\right)^{2k}\overline{P}_{2k,0}\left(\cos\theta\right)\right] \quad \text{(B.2)}$$

where

$$\overline{C}_{2k,0}^{V'}=\left(-1\right)^{k}\frac{3e^{2k}}{\left(2k+1\right)\left(2k+3\right)\sqrt{4k+1}}\left(1-k+5k\frac{J_2}{e^2}\right) \quad \text{(B.3)}$$

where e is the first eccentricity of the ellipsoid, a_l is the semi-major axis of the ellipsoid, and J_2 is the dynamical form factor of the earth.

The gravity potential is the sum of the gravitational potential and centrifugal potential. If the rotation speeds of the reference ellipsoid and actual Earth are the same, the actual and normal centrifugal potential would cancel out and the disturbing potential T can be written as

$$T\left(r,\theta,\lambda\right)=V\left(r,\theta,\lambda\right)-V'\left(r,\theta,\lambda\right) \quad \text{(B.4)}$$

In spherical approximation, the fundamental equation of physical geodesy becomes:

$$\Delta g\approx-\frac{\partial T}{\partial r}-\frac{2}{r}T \quad \text{(B.5)}$$

The spherical harmonics of the gravity anomaly, $\bar{C}_{n,m}^{\Delta g}$ and $\bar{S}_{n,m}^{\Delta g}$, can be easily obtained by substituting (B.1), (B.2) and (B.4) into (B.5).

$$\begin{aligned}\Delta g\left(r,\theta,\lambda\right) &= \frac{GM}{r^2}\left[-1+\left(n-1\right)\sum_{n=2}^{N\max}\left(\frac{a}{r}\right)^n\sum_{m=0}^{n}\left(\bar{C}_{n,m}^{T}\cos m\lambda+\bar{S}_{n,m}^{T}\sin m\lambda\right)\bar{P}_{n,m}\left(\cos\theta\right)\right] \\ &= \frac{GM}{r}\left[1+\sum_{n=2}^{N\max}\left(\frac{a}{r}\right)^n\sum_{m=0}^{n}\left(\bar{C}_{n,m}^{\Delta g}\cos m\lambda+\bar{S}_{n,m}^{\Delta g}\sin m\lambda\right)\bar{P}_{n,m}\left(\cos\theta\right)\right]\end{aligned} \tag{B.6}$$

where $\bar{C}_{n,m}^{T}=\bar{C}_{n,m}-\bar{C}_{n,m}^{V'}$, and $\bar{S}_{n,m}^{T}=\bar{S}_{n,m}-0$. Note that if $m\neq 0$ or n is odd, $\bar{C}_{n,m}^{V'}$ equals zero.

By comparing the two equations in (B.6), we have:

$$\bar{C}_{n,m}^{\Delta g}=\frac{n-1}{r}\left(\bar{C}_{n,m}-\bar{C}_{n,m}^{V'}\right) \tag{B.7}$$

$$\bar{S}_{n,m}^{\Delta g}=\frac{n-1}{r}\bar{S}_{n,m} \tag{B.8}$$

Equation (B.6)-(B.8) are based on the assumption that the spherical harmonic coefficients of the EGM2008 model and normal potential model are given with respect to the same GM and a. If the normal potential coefficients $\hat{\bar{C}}_{n,m}^{V'}$ are given with differently defined $GM^{V'}$ and a_l, the following correction should be applied:

$$\bar{C}_{n,m}^{V'}=\hat{\bar{C}}_{n,m}^{V'}\times\frac{GM^{V'}}{GM}\left(\frac{a_l}{a}\right)^n \tag{B.9}$$

Appendix C: Pseudo-Code for the Adaptive Simulated Annealing

Randomly choose $\mathbf{b}_0$, and compute $E(\mathbf{b}_0)$

Let $\mathbf{b}_{optimal} = \mathbf{b}_0$, $k = 1$

Set T_0

While (number of iteration is smaller than the preset limit)
Do

Calculate new temperature T_k

Generate new state $\mathbf{b}_k$ and compute $E(\mathbf{b}_k)$

If $E(\mathbf{b}_k) \le E(\mathbf{b}_{k-1})$

update state to $\mathbf{b}_k$

If $E(\mathbf{b}_k) < E(\mathbf{b}_{optimal})$ then let $\mathbf{b}_{optimal} = \mathbf{b}_k$

Else

If $\exp(-\Delta E / T_k) \ge$ random [0,1]

update state to $\mathbf{b}_k$

Else

keep $\mathbf{b}_{k-1}$

End If

End If

k to $k+1$

Check the termination criteria

If they are satisfied, then break the While loop

End Do
